Near-field millimeter-wave radio-frequency exposure analysis

Seyedfaraz Jafari

INSTITUT POLYTECHNIQUE DE PARIS

NNT : 2023IPPAT034

Thèse de doctorat

Amirkabir University of Technology
(Tehran Polytechnic)

TELECOM Paris

IP PARIS

Near-field millimeter-wave radio-frequency exposure analysis

Thèse de doctorat de l'Institut Polytechnique de Paris
préparée à Télécom Paris
en cotutelle avec Amirkabir University of Technology

École doctorale n°626 de l'Institut Polytechnique de Paris (ED IP Paris)
Spécialité de doctorat : Réseaux, informations et communications

Thèse présentée et soutenue à Palaiseau, le 22 Novembre 2023, par

JAFARI SEYEDFARAZ

Composition du Jury :

Hélène Roussel Sorbonne Université	Présidente et Examinatrice
Jean Marc Laheurte Université Gustave Eiffel	Rapporteur
Keyvan Forooraghi Tarbiat Modares University	Rapporteur
Christian Person IMT Atlantique	Examinateur
Joe Wiart Ecole Télécom Paris	Directeur de thèse
Alain Sibille Ecole Télécom Paris	Co-directeur de thèse
Reza Sarraf Shirazi Amirkabir University of Technology	Directeur de thèse
Gholamreza Moradi Amirkabir University of Technology	Co-directeur de thèse

Acknowledgements

This work would not have reached its culmination without the unwavering dedication and invaluable guidance of the individuals, to whom I owe a profound debt of gratitude. Their expertise, insights, and encouragement have not only shaped the trajectory of this research but have also enriched my understanding and perspective in profound ways.

My warmest thanks go to everyone who accepted to review this work and thoroughly examined each and every page, particularly my supervisors and the jury members.

I would like to express my gratitude to my supervisor, Prof. Joe Wiart, for his unwavering trust, inspiration, and continuous motivation. He has been an exceptional mentor, and this study would not have reached completion without his invaluable guidance, intellectual and moral support, and encouragement. I would also like to extend my sincere appreciation to my other supervisors, Prof. Alain Sibille, and my co-supervisors, Prof. Reza Sarraf-Shirazi and Prof. Gholamreza Moradi, from the joint institution, Amirkabir University of Technology. Their unwavering support throughout my Ph.D. research has been instrumental.

I extend my gratitude to my colleagues, namely Amirreza, Bader, Maarouf, and others at the chair C2M, for engaging in stimulating discussions and sharing enjoyable moments together. Working closely with all of you has been a tremendous opportunity that I truly appreciate.

Finally, I would like to express my deepest gratitude to my caring and supportive wife. Your unwavering support and encouragement during challenging times are immensely appreciated and will never be forgotten. Additionally, I would like to thank my family for standing by me and providing the strength and encouragement needed to pursue this work. Your presence and support have been invaluable throughout this journey.

Abstract

Fifth-generation wireless (5G) represents the latest advancement in cellular technology, designed to significantly enhance the speed and responsiveness of wireless networks. It aims to address the future demands for increased traffic volume, higher data rates, and the integration of new devices and services. One important consideration is the potential expansion of the communication spectrum into higher frequency bands, surpassing the current range typically used for mobile and wireless communication systems (typically below 6 GHz). A crucial aspect of wireless technologies lies in their direct impact on the human body, necessitating careful examination of their effects. To prevent potential harm caused by radiofrequency-electromagnetic field (RF-EMF) exposure, safety guidelines have been established. At frequencies above 6 GHz, the specific absorption rate (SAR) is replaced by power density (PD) as the exposure criterion, comprising absorbed power density (APD) and incident power density (IPD).

IPD refers to the power density of radiation emitted by an antenna in free space, which can be measured at various distances from the antenna, whether near or far. However, in scenarios involving near-field exposure where the antenna is in close proximity to the human body, IPD may no longer be a suitable option. This is because the interaction between the human body and the antenna, including coupling and multiple reflections, can lead to changes in the antenna's current and result in mismatches, alterations in radiation patterns, and increased exposure levels. These antenna-body interactions cannot be adequately assessed using IPD. Instead, APD takes into account the coupling between the antenna and the human body, allowing for a more accurate evaluation of the actual exposure level.

The objective of this thesis is to determine the APD by considering the effects of coupling between the antenna and the human body when they are in close proximity to each other at 5G mm-wave frequencies. To achieve this goal, two ideas have been proposed. The first idea focuses on measuring the E-field within a liquid model of human tissue. This method has traditionally been employed to evaluate SAR at frequencies below 6 GHz. In this thesis, a significant portion is dedicated to expanding this conventional method for higher frequencies and conducting the necessary investigations to practically implement this idea. On the other hand, the second idea concentrates on measuring the E-field surrounding the antenna outside of the phantom, using a non-invasive approach, as a means to assess the APD.

In the first idea, a patch antenna with 2×2 arrays operating at 10, 24, and 60 GHz is considered, with a radiated power of 200 milliwatts (the maximum power allowed in previous generations and the fifth generation of telecommunications). The goal is to obtain the APD. The process begins by sampling the E-field on a plane inside a model of human skin tissue at a specific distance from the skin surface. Subsequently, the E-field

beneath the air-phantom interface is evaluated by back-propagating the E-field using the plane wave expansion method (PWS). The investigation includes varying the antenna-phantom separation distances and the distances between the sampling plane and the air-phantom interface. Due to the shallow penetration depth of electromagnetic waves at mm-wave frequencies, the human body is modeled as a homogeneous half-space with skin tissue properties. The reconstruction errors at 10, 24, and 60 GHz were found to be no larger than 9.4%, 7.35%, and 7.8%, respectively, when evaluating the maximum spatially averaged power density for distances greater than 1 mm between the antenna and the phantom. Furthermore, the study explores the E-field measurement requirements inside the human skin model, including amplitude detection error and phase uncertainty. The proposed approach offers an accurate method with high computational efficiency and minimal measurement time compared to evaluating power density in free space using the PWS method. This study provides valuable insights for assessing APD in next-generation wireless telecommunications and establishes electromagnetic field compliance testing methods for products operating within these frequency bands.

The second idea focuses on evaluating the APD by utilizing E-field information, including the coupling between the antenna and the phantom, from outside the phantom. To accomplish this, the dyadic Green's function (DGF) is employed, presenting a non-invasive approach for assessing the APD. A practical method is devised to thoroughly analyze the APD regarding the coupling between the human skin model and the device under test (DUT). In the proposed method, the entire space is divided into two half-spaces. The upper half-space ($z > 0$) is filled with air, where the antenna is positioned, while the lower half-space is filled with an equivalent human skin liquid/solid model. The process begins by collecting the necessary data by sampling the electric fields on the surface of the hemisphere surrounding the antenna in the upper half-space. The electric field integral equation (EFIE) is then solved inversely using the method of moments (MoM) to reconstruct the equivalent source currents. Subsequently, the APD is evaluated beneath the interface of the air and the skin model phantom using spatial DGFs. Reconstruction errors are assessed for two types of antenna array placements: at the edge and corner of the mobile phone, at frequencies of 15, 30, and 60 GHz. The reconstructed APD demonstrates good agreement with the reference, particularly at higher frequencies. For instance, at 60 GHz, the maximum error in spatially averaged APD did not exceed 8.75% and 11.1% for the edge and corner antenna types, respectively. Additionally, measurement requirements, including sampling angular resolution, E-field measurement uncertainty (amplitude and phase error), and required phantom size, are investigated. It is shown that the proposed technique paves the way for a new methodology to assess APD, including the antenna-human body coupling, for exposure to handheld devices operating above 6 GHz.

Résumé

La technologie sans fil de cinquième génération (5G) représente la dernière avancée dans le domaine de la technologie cellulaire, conçue pour améliorer considérablement la vitesse et la réactivité des réseaux sans fil. Elle vise à répondre aux besoins futurs en matière de volume croissant du trafic, de débits de données plus élevés et d'intégration de nouveaux appareils et services. Une considération importante concerne l'expansion potentielle du spectre de communication vers des bandes de fréquences plus élevées, dépassant la plage actuellement utilisée pour les systèmes de communication mobile et sans fil (généralement en dessous de 6 GHz). Un aspect crucial des technologies sans fil réside dans leur impact direct sur le corps humain, ce qui nécessite une étude approfondie de leurs effets. Des lignes directrices de sécurité ont été établies pour prévenir les éventuels dangers liés à l'exposition aux champs électromagnétiques de radiofréquence (RF-EMF). Aux fréquences supérieures à 6 GHz, le taux d'absorption spécifique (SAR) est remplacé par la densité de puissance (PD) en tant que critère d'exposition, comprenant la densité de puissance absorbée (APD) et la densité de puissance incidente (IPD).

L'IPD fait référence à la densité de puissance du rayonnement émis par une antenne dans l'espace libre, qui peut être mesurée à différentes distances de l'antenne, qu'elle soit proche ou lointaine. Cependant, dans les scénarios d'exposition en champ proche où l'antenne est en proximité immédiate du corps humain, l'IPD peut ne plus être une option appropriée. En effet, les interactions entre le corps humain et l'antenne, comprenant le couplage et les réflexions multiples, peuvent entraîner des variations du courant de l'antenne, des incompatibilités, des altérations des diagrammes de rayonnement et une augmentation des niveaux d'exposition. Ces interactions entre l'antenne et le corps humain ne peuvent pas être adéquatement évaluées à l'aide de l'IPD. À la place, l'APD tient compte du couplage entre l'antenne et le corps humain, permettant ainsi une évaluation plus précise du niveau d'exposition réel.

L'objectif de cette thèse est de déterminer l'APD en tenant compte des effets de couplage entre l'antenne et le corps humain lorsqu'ils sont en proximité l'un de l'autre aux fréquences millimétriques 5G. Pour atteindre cet objectif, deux idées ont été proposées. La première idée se concentre sur la mesure du champ E à l'intérieur d'un modèle liquide de tissu humain. Cette méthode est traditionnellement utilisée pour évaluer le DAS à des fréquences inférieures à 6 GHz. Dans cette thèse, une part importante est consacrée à l'extension de cette méthode conventionnelle pour des fréquences plus élevées et à la réalisation des enquêtes nécessaires pour mettre en uvre cette idée de manière pratique. En revanche, la deuxième idée se concentre sur la mesure du champ E entourant l'antenne à l'extérieur du fantôme, en utilisant une approche non invasive, afin d'évaluer l'APD.

Dans la première idée, une antenne patch avec des matrices 2×2 fonctionnant à 10, 24 et 60 GHz est considérée, avec une puissance rayonnée de 200 milliwatts (la puis-

sance maximale autorisée dans les générations précédentes et la cinquième génération des télécommunications). L'objectif est d'obtenir l'APD. Le processus commence par l'échantillonnage du champ E sur un plan à l'intérieur d'un modèle de tissu cutané humain à une distance spécifique de la surface de la peau. Ensuite, le champ E sous l'interface air-fantôme est évalué en rétropropageant le champ E à l'aide de la méthode d'expansion d'onde plane (PWS). L'étude comprend des variations des distances de séparation antenne-fantôme et des distances entre le plan d'échantillonnage et l'interface air-fantôme. En raison de la faible profondeur de pénétration des ondes électromagnétiques aux fréquences millimétriques, le corps humain est modélisé comme un demi-espace homogène avec des propriétés de tissu cutané. Les erreurs de reconstruction à 10, 24 et 60 GHz se sont révélées inférieures à 9,4%, 7,35% et 7,8% respectivement, lors de l'évaluation de la densité de puissance maximale spatialement moyenne pour des distances supérieures à 1 mm entre l'antenne et le fantôme. De plus, l'étude explore les exigences de mesure du champ E à l'intérieur du modèle de peau humaine, notamment l'erreur de détection d'amplitude et l'incertitude de phase. L'approche proposée offre une méthode précise avec une efficacité de calcul élevée et un temps de mesure minimal par rapport à l'évaluation de la densité de puissance en espace libre à l'aide de la méthode PWS. Cette étude fournit des informations précieuses pour évaluer l'APD dans les télécommunications sans fil de nouvelle génération et établit des méthodes de test de conformité aux champs électromagnétiques pour les produits fonctionnant dans ces bandes de fréquences.

La deuxième idée se concentre sur l'évaluation de l'APD en utilisant des informations sur le champ E, y compris le couplage entre l'antenne et le fantôme, depuis l'extérieur du fantôme. Pour ce faire, la fonction dyadique de Green (DGF) est utilisée, présentant une approche non invasive pour évaluer l'APD. Une méthode pratique est conçue pour analyser en détail l'APD concernant le couplage entre le modèle de peau humaine et le dispositif testé (DUT). Dans la méthode proposée, l'espace entier est divisé en deux demi-espaces. Le demi-espace supérieur ($z > 0$) est rempli d'air, où se trouve l'antenne, tandis que le demi-espace inférieur est rempli d'un modèle équivalent de liquide/solide de peau humaine. Le processus commence par la collecte des données nécessaires en échantillonnant les champs électriques sur la surface de l'hémisphère entourant l'antenne dans le demi-espace supérieur. L'équation intégrale du champ électrique (EFIE) est ensuite résolue de manière inverse à l'aide de la méthode des moments (MoM) pour reconstruire les courants sources équivalents. Ensuite, l'APD est évaluée sous l'interface de l'air et du modèle fantôme de peau à l'aide des DGF spatiaux. Les erreurs de reconstruction sont évaluées pour deux types de placement d'antennes : sur le bord et dans le coin du téléphone portable, aux fréquences de 15, 30 et 60 GHz. L'APD reconstruit montre une bonne concordance avec la référence, notamment à des fréquences plus élevées. Par exemple, à 60 GHz, l'erreur maximale dans l'APD moyenne spatialement n'a pas dépassé 8,75% et 11,1% respectivement pour les types d'antennes sur le bord et dans le coin. De plus, les exigences de mesure, y compris la résolution angulaire d'échantillonnage, l'incertitude de mesure du champ E (erreur d'amplitude et de phase) et la taille du fantôme requise, sont étudiées. Il est démontré que la technique proposée ouvre la voie à une nouvelle méthodologie pour évaluer l'APD, y compris le couplage antenne-corps humain, pour l'exposition à des appareils portables fonctionnant au-dessus de 6 GHz.

Contents

List of Figures

List of Tables

List of Abbreviations

5G	Fifth-generation
PD	Power Density
IPD	Incident Power Density
IPD_{eq}	Equivalent Incident Power Density
APD	Absorbed Power Density
TPD	Transmitted Power Density
SAR	Specific Sbsorbtion Rate
TA	Thermal Analysis
EQC	Equivalent Current method
SRM	Source Reconstruction Method
PWS	Plane Wave Spectrum method
MoM	Method of Moments
DGF	Dyadic Green's Function
SWE	Spherical Wave Expansion method
NFM	Null Field Method
MAS	Method of Auxiliary Sources
FDTD	Finite-Difference Time-Domain method
FIT	Finite Integration Technique
FEM	Finite Element Method
TLM	Transmission Line Method
GB-IBEM	Galerkin-Bubnov Indirect Boundary Element method
RF	Radio Frequency
EMF	Electromagnetic Field
DUT	Device Under Test
AUT	Antenna Under Test
ICNIRP	International Commission on Non-Ionizing Radiation Protection
IEEE	Institute of Electrical and Electronics Engineers

Chapter 1

Introduction

With the deployment of fifth-generation (5G) mobile networks, mobile broadband speeds are significantly faster, and extensive mobile data usage is guaranteed. This is made possible by utilizing additional higher frequency bands. 5G aims to serve as the intersection of various communication domains, including virtual reality, autonomous vehicles, the industrial Internet, and smart cities. Additionally, 5G is considered the fundamental technology for the Internet of Things (IoT), enabling machine-to-machine (M2M) communication. 5G networks operate across multiple frequency bands, with lower frequencies initially allocated for the first phase of 5G deployment. Many of these frequencies have been used in previous generations of mobile communications. Furthermore, much higher radio frequencies are planned to be utilized in later stages of technological development. These new frequency bands are significantly higher than the UHF range, with wavelengths ranging from centimeters (6 to 30 GHz) to millimeters (30 to 300 GHz).

5G networks and associated IoT networks significantly increase the number of wireless devices compared to the current situation, necessitating high infrastructure density. Consequently, a much larger volume of mobile data is generated in each area. As a result, higher network densities are required due to the shorter range of higher frequencies. The introduction of wireless communication devices operating in the high-frequency portions of the electromagnetic spectrum has attracted a significant amount of research focused on health concerns [1].

Serious concerns have recently been raised regarding the adverse effects of exposure to electromagnetic fields (EMF) on the human body [2]. Promising 5G communication networks offer advantages such as high data rates, low latency, and increased capacity. However, these advancements may raise concerns regarding the potential increase in EMF energy exposure for human users. While it may be perceived that the higher data rates of 5G necessitate increased signal power at the receiver, it is important to note that this is not the case. In fact, the design principles of 5G emphasize achieving optimal data rates with efficient power usage. The advancements in 5G, such as the use of advanced modulation schemes, beamforming, and Massive MIMO, contribute to higher data rates without requiring a proportional increase in signal power [3]. Therefore, Public concerns may be related to the increasing number of cell towers, antennas, and the use of higher frequencies. At frequencies above 6 GHz, which are likely to be used in future 5G mobile telecommunications systems, two changes are expected to further amplify these concerns. Firstly, more transmitters on base stations and mobile devices will be operational. Secondly, narrow beams will be utilized as a solution for greater attenuation in high-frequency

bands [4].

Before delving into the required standards and instructions for human body exposure, it is necessary to understand the energy and power transmitted by electromagnetic waves and their relationships. In wireless communication systems, electromagnetic fields are utilized to transmit information over both long and short distances. Energy is essential for facilitating this transfer through electromagnetic waves. As shown in Figure 1.1, the electromagnetic energy within a defined region V, enclosed by the surface S and characterized by electric and magnetic properties ε, σ, and μ, can be mathematically expressed as follows [5]

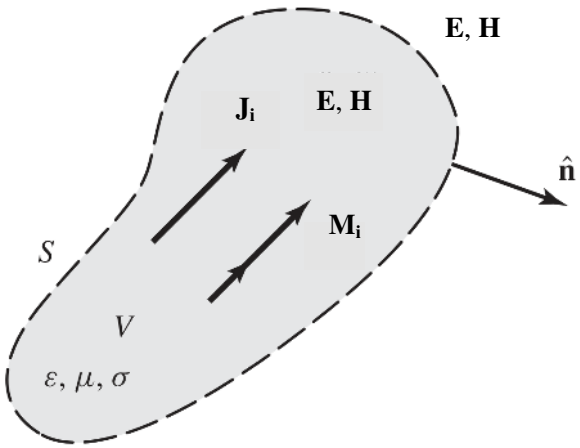

Figure 1.1: E- and H-fields due to $\mathbf{M_i}$ and $\mathbf{J_i}$ inside of the S [5].

$$\begin{aligned} \nabla \times \mathbf{E} &= -\mathbf{M_i} - j\omega\mu\mathbf{H} = -\mathbf{M_i} - \mathbf{M_d} \\ \nabla \times \mathbf{H} &= \mathbf{J_i} + \sigma\mathbf{E} + j\omega\varepsilon\mathbf{E} = \mathbf{J_i} + \mathbf{J_c} + \mathbf{J_d} \end{aligned} \tag{1.1}$$

where $\mathbf{E}$ and $\mathbf{H}$ represent the phasors of the electric field (V/m) and the magnetic field (A/m) respectively, $\mathbf{J_i}$, $\mathbf{J_c}$, and $\mathbf{J_d}$ denote the source, conduction, and induction electric current density ($\mathrm{A/m^2}$), and $\mathbf{M_i}$ and $\mathbf{M_d}$ represent the source and induction magnetic current density ($\mathrm{V/m^2}$) respectively

By performing inner multiplication of the first equation with the conjugate of the second equation in (1.1), and subsequently considering their difference, applying vector equality, dividing both sides of the equality by 2, integrating over the volume V, and applying the divergence theorem to convert the volume integral to a surface integral, we obtain the equation of (energy) stability.

$$\begin{aligned} -\frac{1}{2}\iiint_V (\mathbf{H}^* \cdot \mathbf{M_i} + \mathbf{E} \cdot \mathbf{J_i^*}) dv = \oiint_S (\frac{1}{2}\mathbf{E} \times \mathbf{H}^*) \cdot ds + \frac{1}{2}\iiint_V \sigma|\mathbf{E}|^2 dv \\ + j2\omega \iiint_V (\frac{1}{4}\mu|\mathbf{H}|^2 - \frac{1}{4}\varepsilon|\mathbf{E}|^2) dv) \end{aligned} \tag{1.2}$$

Thus, considering the average Poynting vector (average power density) in a time interval

$$\mathcal{P}_{av} = \mathbf{S} = \frac{1}{2}\,\mathrm{Re}[\mathbf{E} \times \mathbf{H}^*] \tag{1.3}$$

where $\boldsymbol{\mathcal{P}} = \boldsymbol{\mathcal{E}} \times \boldsymbol{\mathcal{H}}$ is the Poynting vector in the time domain, whose unit is W/m^2. Thus, the (1.2) can be written as follows

$$P_s = P_e + P_d + j2\omega(\overline{W}_m - \overline{W}_e) \tag{1.4}$$

where

$$P_s = -\frac{1}{2}\iiint_V (\mathbf{H}^* \cdot \mathbf{M_i} + \mathbf{E} \cdot \mathbf{J_i^*})dv, \tag{1.5}$$

$$P_e = \oiint_S (\frac{1}{2}\mathbf{E} \times \mathbf{H}^*) \cdot ds, \tag{1.6}$$

$$P_d = \frac{1}{2}\iiint_V \sigma|\mathbf{E}|^2 dv, \tag{1.7}$$

$$\overline{W}_m = \iiint_V \frac{1}{4}\mu|\mathbf{H}|^2 dv, \tag{1.8}$$

$$\overline{W}_e = \iiint_V \frac{1}{4}\varepsilon|\mathbf{E}|^2 dv \tag{1.9}$$

where P_s is the complex power of sources (W), P_e is the total complex power exits from the volume V enclosed by the surface S (W), P_d is the dissipated real power (W), $\overline{W}_m$ is the time-average magnetic energy (J) and $\overline{W}_e$ is the time-average electric energy (J). This equation is called the law of conservation of energy.

Therefore, by considering the concept of energy in electromagnetism and taking into account the conditions under which these waves exist in different media, it is possible to accurately investigate the absorbed energy and the incident or absorbed power density in the human body. In the following section, we will review the standards and guidelines for analyzing radiation effects on the human body.

1.1 Guidelines

The frequency band around 28 GHz is considered the most promising for 5G mobile communication systems and has thus garnered significant attention. Concerns regarding the adverse health effects of electromagnetic field exposure exist. International safety guidelines and standards aimed at protecting humans from radio-frequency electromagnetic fields have been published by the International Commission on Non-Ionizing Radiation Protection (ICNIRP) [6] and the IEEE International Commission on Electromagnetic Safety [7].

For the frequencies currently utilized in the second, third, and fourth generations of telecommunication, the specific absorption rate (SAR) in watts per kilogram is used as a measure of radiation exposure to the human body. This criterion is designed to mitigate risks associated with localized temperature increase in tissues [8]. At higher frequencies, energy absorption in human tissue is more superficial. Consequently, the radiation criterion transitions from SAR to power density (PD) in terms of watts per square meter. The criteria switching frequency, as indicated in the latest published standards and guidelines [6, 7], is set at 6 GHz.

Since the official proposal of human exposure standards in 2002, numerous reforms have been implemented. The most recent revision was published by IEEE in October

2019 [7], improving upon the guidelines and standards from 2005 [9] and 2002 [10]. Subsequently, the International Commission on Non-Ionizing Radiation Protection (ICNIRP) released revised guidelines in April 2020 to limit exposure to electromagnetic fields in the frequency range of 100 kHz to 300 GHz [6]. These updates include revisions to the RF-EMF section of the 1998 ICNIRP guidelines [11] and the 100 kHz to 10 MHz portion of the ICNIRP low-frequency guidelines [12]. Although the limitations specified in the new guidelines are largely consistent with previous versions, both the IEEE and ICNIRP have introduced some changes to the RF-EMF exposure ranges above 6 GHz.

1.1.1 Exposure limits below 6 GHz

At frequencies below 6 GHz, electromagnetic waves penetrate deeply into human tissues. For this reason, the standard of specific absorption rate has been defined at these frequencies.

1.1.1.1 Specific absorption rate

Specific absorption rate is the rate of absorbed electromagnetic power (W) by the tissue to the mass of the tissue (kg).

$$SAR = \frac{Absorbed\ Power\ in\ V}{Volume\ Mass\ of\ V} \tag{1.10}$$

The SAR measurement is often performed by averaging the absorbed energy over the entire body or specific organs. The IEEE and ICNIRP standards were developed to regulate human exposure by utilizing whole-body SAR, which represents the average SAR over the entire body. Additionally, these standards consider the maximum SAR averaged over 1 or 10 grams of tissue mass. In these cases, the objective is to estimate the maximum SAR within a continuous volume of tissue weighing 1 or 10 grams. The shape of the volume varies depending on the standard: IEEE recommends a cubic shape, while ICNIRP favors continuous tissues. The absorbed electromagnetic energy in the tissue volume (V) can be estimated either through the electric field method or by measuring the temperature rise. The former method is influenced by tissue conductivity, while the latter requires information about heat capacity [1].

The method of evaluating SAR based on temperature is less commonly utilized compared to the approach based on the electric field. In addition to the challenges related to measurement accuracy and sensitivity, there is another issue when measuring SAR through temperature, which is the requirement for achieving a steady state before each measurement. This requirement poses a challenge to the measurement process itself. For instance, if a large number of measurement points are involved, this limitation can result in a prolonged measurement time, which conflicts with other constraints such as the battery life of mobile phones. Therefore, the evaluation of exposure from mobile phones is typically carried out through electric field assessment [13].

[1] Heat capacity is a physical quantity for a substance, and it is the amount of heat that, if given to a certain amount of that substance, will raise its temperature by one unit. The SI unit for heat capacity is J/K.

Measuring the electric field using small antennas or optical probes is the most common method used for the experimental evaluation of SAR. The (1.11) gives the relation between SAR and electric field.

$$SAR = \frac{\iiint_V \sigma |\mathbf{E}|^2 dv}{2 \iiint_V \rho dv}, \tag{1.11}$$

where σ, ρ and $\mathbf{E}$ respectively are the conductivity of the body tissue (S/m), the mass density of the tissue (kg/m^3), and the maximum amplitude of electric field in the tissue (V/m). The $\frac{1}{2}$ coefficient can be included or omitted, depending on whether RMS (root mean square) or maximum electric field strength value is utilized.

1.1.2 Exposure limits above 6 GHz

As the frequency increases, the ability of electromagnetic waves to penetrate the body becomes limited and superficial. Above 6 GHz, local exposure is defined in terms of absorbed power density by ICNIRP basic restrictions [6] and epithelial power density by IEEE dosimetric reference limits (DRLs) [7]. Since assessing basic restrictions/DRLs can be challenging, the IEEE and ICNIRP provide additional limits, such as *reference levels or exposure reference limits* (ERLs), which utilize more practical quantities for evaluation purposes. Above 6 GHz, reference levels/ERLs and the RF exposure limits specified by the Federal Communications Commission (FCC) are defined in terms of incident power density.

1.1.2.1 Incident power density

According to IEEE and ICNIRP Guidelines, the spatial-average incident power density can be express as

$$S_{inc} = \frac{1}{A} \int_A \mathrm{Re}[\mathbf{E} \times \mathbf{H}^*] \cdot \hat{n} ds \tag{1.12}$$

where Re represents the real part, E and H denote the RMS complex electric field and the RMS complex magnetic field, respectively. The superscript * denotes the complex conjugation, and $\hat{n}$ represents the unit vector normal to the averaging area.

The ICNIRP 2020 guidelines impose a limitation on the incident power density for the general public, given by $55 f_G^{-0.177}$ W/m^2 (f_G represents the frequency in GHz) for the frequency range of 6-300 GHz. The incident power density, averaged over a square area of 4 cm^2 on the body surface, should not exceed the specified limit values. Additionally, for frequencies above 30 GHz, the incident power density averaged over a square area of 1 cm^2 should not exceed twice the restriction imposed for the 4 cm^2 area, namely $110 f_G^{-0.177}$ W/m^2.

The IEEE Std C95.1-2019 also adopts the same spatial-averaging restrictions of 4 cm^2 as defined in the ICNIRP 2020 guidelines. Above 30 GHz, if the area of the –3 dB contour relative to the peak spatial incident power density is less than 1 cm^2, the incident power density averaged over 1 cm^2 should not exceed twice the limits specified for the 4 cm^2 area.

In the FCC regulations [14], the Maximum Permissible Exposure (MPE) limits for incident power density are set at 10 W/m^2 for the general population. Although the

current FCC compliance assessment procedures applicable to mmWave handsets consider this value to be averaged over 4 cm^2 [15, 16], the FCC rules have not yet specified a maximum spatial power density limit for local exposure above 6 GHz. As a result, the FCC recently proposed a general local power density limit of 40 W/m^2, averaged over 1 cm^2 above 6 GHz [17]. Table 1.1 provides a summary of the ICNIRP and IEEE incident power density limitations, including recent updates, as well as the limitations currently in use and those proposed by the FCC.

Table 1.1: Inicident Power Density Limits ($f > 6$ GHz) [18]

	f_G (GHz)	Averaging area (cm^2)	S_{inc} (W/m^2)
ICNIRP [6]	6–300	4	$55 f_G^{-0.177}$
	30–300*	1	$110 f_G^{-0.177}$
IEEE C95.1 - 2019 [7]	6–300	4	$55 f_G^{-0.177}$
	30–300*	1	$110 f_G^{-0.177}$
FCC (current) [14–16]	6–100	4	10
FCC (proposed) [17]	6-3000	1	40

* According to IEEE C95.1 - 2019, 1 cm^2 averaging is required only when the area of the –3 dB contours relative to the peak spatial incident power density is less than 1 cm^2.

1.1.2.2 Absorbed/Epithelial power density

From a perspective of health risks, our primary concern lies in the amount of electromagnetic field (EMF) energy absorbed by biological tissues, as it is a significant factor in inducing heating effects. This is commonly expressed as a dosimetric quantity. Below 6 GHz, where EMFs can deeply penetrate tissues, it is advantageous to define this in terms of the "specific energy absorption rate" (SAR), which represents the power absorbed per unit mass (W/kg). Conversely, above 6 GHz, where EMFs are absorbed more superficially, it is more appropriate to define exposure in terms of the density of absorbed power over an area (W/m^2), which can be referred to as the "absorbed power density."

The absorbed power density is determined by calculating the spatially-averaged Poynting vector projected perpendicular to the averaging area on the body surface (S_{ab}). The power flow through the epithelium per unit area directly beneath the body surface is defined as the epithelial power density. Although expressed using different terms, absorbed power density and epithelial power density represent the same quantity.

Above 6 GHz, the absorption of radio-frequency power or energy mainly occurs within the very superficial regions of the body. For instance, at 6 GHz and 300 GHz, the penetration depths (defined as the distance from the surface where 86% of the radio-frequency power is absorbed) are approximately 8.1 mm and 0.23 mm, respectively (refer to Table 1.2). The absorbed power density (W/m^2) is defined at the body surface as

follows

$$S_A = \iint_A dxdy \int_0^{Z_{max}} \rho(x,y,z) \cdot \mathbf{SAR}(x,y,z)dz/A, \tag{1.13}$$

where the body surface is at $z = 0$, A is the averaging area (in m^2), and Z_{max} is depth of the body at the corresponding region; where Z_{max} is much larger than the penetration depth, infinity can be substituted for Z_{max}.

A more rigorous formula for absorbed power density is based on the Poynting vector (S):

$$S_A = \iint_A \mathrm{Re}[\mathbf{S}] \cdot d\mathbf{s}/A = \iint_A \mathrm{Re}[\mathbf{E} \times \mathbf{H}^*] \cdot d\mathbf{s}/A. \tag{1.14}$$

The only difference between the (1.14) and (1.12) is that in the (1.12) the electric field in free space is considered without the presence of the human tissue model. In contrast, the field is examined within the context of the human tissue model situated beneath the surface in (1.14).

When the far-field assumption is considered, the incident power density (S_{inc}) is also related to the absorbed power density (S_{ab}) through the reflection coefficient (Γ).

$$\mathbf{S_A} = \left(1 - |\Gamma|^2\right) \mathbf{S_{inc}}. \tag{1.15}$$

The reflection coefficient (Γ) is derived from the dielectric properties of the tissues, shape of the body surface, incident angle, and polarization.

Table 1.2: Penetration depth of human skin tissue (dermis), 6–300 GHz [6]

f_G (GHz)	Relative permittivity	Conductivity (S/m)	Penetration depth (mm)
6	36	4.0	8.1
10	33	7.9	3.9
30	18	27	0.92
60	10	40	0.49
100	7.3	46	0.35
300	5.0	55	0.23

In near-field exposure scenarios, the components of the Poynting vector are not real values but complex values. In such cases, a detailed investigation of the Poynting vector components may be necessary to calculate the incident power density relevant to radio-frequency safety.

The ICNIRP 2020 guidelines establish a basic restriction for the general public's absorbed power density. This limit is set at 20 W/m^2, averaged over a period of 6 minutes, and over a surface area of 4 cm^2 on the body. Additionally, to account for focal beam exposure in the frequency range of 30–300 GHz, the absorbed power density averaged over a square surface area of 1 cm^2 on the body should not exceed twice the basic restrictions

of 4 cm^2, which is 40 W/m^2. Table 1.3 provides an overview of the basic restrictions for absorbed/epithelial power density.

Table 1.3: Basic restrictions for absorbed power density (6–300 GHz), averaging intervals $\geq$ 6 min

	f_G (GHz)	Averaging area (cm^2)	Local S_{ab} (W/m^2)
ICNIRP [6]	6–300	4	20
	30–300*	1	40
IEEE C95.1 - 2019 [7]	6–300	4	20
	30–300*	1	40

* According to ICNIRP 2020, above 30 GHz, an additional constraint is imposed, such that exposure averaged over a square 1 cm^2 surface area of the body is restricted to two times that of the 4 cm^2 restriction

1.2 Objectives and outline of the thesis

The absorbed or epithelial power density is an important criterion in human exposure, particularly at frequencies above 6 GHz, where fifth-generation telecommunication is expected to demonstrate its maximum potential. Calculating the absorbed power density requires knowledge of the electric and magnetic fields beneath the air-phantom interface, as indicated in equation (1.14). Given that the absorbed power density provides a more accurate measure for evaluating exposure when the antenna is in close proximity to the human body, this thesis focuses on exploring practical methods to assess the electric and magnetic fields beneath the air-phantom interface when the human body is in the near-field region of the antenna.

Consequently, the dissertation's main objective is to develop methods for reconstructing and determining the electric and magnetic fields, initially near the antenna and then on the lower surface of the air and phantom boundary. Several studies related to the reconstruction of electric and magnetic fields in the far and near distances of antennas have been reviewed and analyzed in the context of existing literature.

Previous literature, such as [19], has extensively discussed the measurement of the near field of antennas and the characteristics of these fields. However, due to the unclear and varying conditions of the electric and magnetic fields at this distance, research efforts historically focused on accurately measuring antennas at long distances, primarily in the far field. In recent decades, however, there has been increased attention and interest in achieving accuracy and practical measurements of the near field.

In the 1970s, the use of near-field measurements as an alternative to far-field measurements was proposed to determine the radiation pattern of large antennas [20]. During that time, it was challenging to measure the far-field characteristics of large antennas, such as reflectors and Base Transceiver Station (BTS) antennas, at long distances. As a result, the concept of measuring the near field of antennas within the Fresnel zone and

converting it to the far field was introduced. Around 15 years later, in 1985, a comprehensive survey of near-field measurements revealed the establishment of approximately 50 near-field sites worldwide, highlighting the significance of this approach for important applications [21].

Recognizing the importance of near-field measurements in investigating the radiation characteristics of large antennas, significant advancements were made in field measurements and near-field to far-field conversion methods during the 1990s. In this period, various coordinate systems such as Cartesian, cylindrical, and spherical coordinates were utilized to expand the radiation modes of the antenna. The coefficients of this expansion were determined based on the field measurements in the corresponding coordinates. Subsequently, these obtained modes were expanded to determine the field at the desired location. In addition to the established methods, such as Cartesian, cylindrical, and spherical measuring techniques, new approaches such as the polar linear measuring method and bipolar measuring method were introduced in 1995 [22].

In the 1990s, as more accurate methods for measuring near fields emerged, another field of application for near-field measurements was proposed. It was discovered that, just as the near field measured at a certain distance can be converted to the far field, it also has the potential to be converted to even closer fields surrounding the antenna. This led to the introduction of back projection reconstruction in antennas, enabling the detection of errors in antennas (referred to as antenna diagnostic applications). Notably, Dr. Rahmat-Samii's works on reflector antennas played a significant role during this period [23–29]. In these articles, near-field measurements were used to recover the amplitude and phase of the surface field on reflector antennas, allowing for the identification of manufacturing errors. The resulting image, obtained by reconstructing the amplitude and phase on the antenna's surface, was referred to as a microwave holographic image. By utilizing microwave holography, various errors in reflector antenna construction, including sudden misalignments and surface distortions, could be determined. In some cases, the Root Mean Square (RMS) error of the reflector surface was also evaluated through the reconstruction of the antenna's surface fields [29]. It is important to note that the techniques and methods employed in converting the near field to surface fields in these diagnostic articles are the same as the conventional techniques used for converting the near field to the far field.

Between 1995 and 2000, alongside the advancements made in the modes or modal expansion method, another method based on the equivalence principle was introduced for converting near fields to far fields [30–32]. Dr. Tapan K. Sarkar can be recognized as the pioneering developer of these methods, which later became known as the Equivalent Current Method (EQC) or Source Current Reconstruction Method (SRM). In the SRM method, instead of reconstructing the radiation modes, the surface equivalent currents of the antenna are determined based on near-field measurements. These currents are then utilized for field assessment at desired distances. Since this method is based on solving full-wave equations using the numerical Method of Moments, it offers greater flexibility compared to the modes expansion method. However, it requires more computational resources and entails greater complexity.

The heavy computational requirements of the Source Current Reconstruction Method (SRM) caused researchers to take notice of these methods slightly later than the conventional modal expansion method. In 2007, it was demonstrated in [33] that the SRM method, unlike the modal expansion method, can be implemented in arbitrary measurements and arbitrary 3D reconstructions. In other words, while the modal expansion

method is limited to Cartesian, cylindrical, or spherical coordinates, the integral equations of the SRM can be applied to any desired surface by meshing and subsequently reconstructing the currents on three-dimensional surfaces. This article drew greater attention to the SRM method in the field of field reconstruction.

The high flexibility of the SRM method in reconstructing equivalent currents redirected much of the researchers' focus from near-to far-field conversion to the domain of antenna diagnostics in recent years. Several applications of the SRM method have emerged, including the removal of disturbing elements' effects in far-field measurements [34], correction of structural defects in radomes [35], identification of defect locations in array antennas [36, 37], and investigation of electromagnetic interference [38]. These applications are derived from articles published in this field over the past few years. Furthermore, some recent articles have proposed utilizing the SRM method for antenna design and synthesis, as well as reconstructing the shape of metallic structures.

In the realm of human exposure from fifth-generation telecommunications, existing dosimetry systems [39–41] measure the incident power density in free space near the wireless Device Under Test (DUT). In [39], the incident power density is obtained by measuring the amplitude and polarization of the electric field (E-field). In [40], it is determined through the measurement of both the E-field and magnetic field (H-field) using the two-probe method. The frequency range for measurements within 2 mm and 0.5 mm of the DUT in [39, 40] is from 6 to 110 GHz, employing field probes. In [41], a multi-probe technology with switching networks is employed for spherical near-field measurements to obtain incident power density in the frequency range of 18 to 50 GHz. However, when an antenna is positioned near a lossy medium such as human skin, electromagnetic characteristics change at the air-phantom interface, resulting in near-field interactions that alter the incident field exposed to the human body compared to free space [42, 43]. Therefore, in incident power density measurements, the changes in power density caused by the coupling of the DUT with the human body are not considered. This coupling may affect the power absorption in the human body and lead to increased heating [44].

By reviewing this brief history, the ultimate goal of this thesis can be defined as follows: In the first part, the backward plane wave reconstruction method in the spectral domain is employed. In the second part, the method of reconstructing equivalent currents is utilized. This goal can be seen as a continuation of the recent development in power density evaluation, with the distinction that this thesis focuses on considering the mutual effects between the antenna and the human body model, such as coupling and multiple reflections between the antenna and the human body. Unlike previous articles that have used incident power density or absorbed power density without considering the antenna-human body interaction effects in evaluating human exposure.

1.2.1 Thesis novelty

Although this thesis presents numerous innovations in problem-solving methods and applications, which will be discussed in the following sections, the author believes that its most significant advantage lies in achieving practical outcomes in the field of human exposure at very close distances to the antenna. Through various research conducted during the thesis, it was determined that despite the increasing attention given to near- and very near-field measurements for evaluating incident power density worldwide, specific implementations for APD evaluation are still lacking. The methods presented in this thesis

cover a wide range of applications in human exposure, taking into account the coupling and multiple reflections between the antenna and the dielectric medium (human body model).

In summary, the thesis introduces the following innovations in different parts:

1. Investigation of the feasibility of measurements inside the human tissue model at 5G mm-wave frequencies.

2. Proposal of a practical invasive/non-invasive measurement method for assessing absorbed power density from 5G mm-wave antennas.

3. Consideration of the mutual effects between the antenna and the human body when the antenna is in close proximity to the human body for APD assessment.

4. Examination of the measurement requirements and the impact of factors such as the uncertainty of the amplitude and phase of the measured electric field, the size of the sampling plane, the position of the antenna relative to the measurement plane, and the dimensions of the phantom that replaces the human body.

1.3 Organization of the dissertation

The thesis is divided into five chapters. Chapter 1 provides an overview of the deployment of 5G mobile networks, discussing their key characteristics. It also addresses potential health hazards and the interactions between electromagnetic fields and the human body. The chapter introduces parameters for quantifying this energy and presents international guidelines and European directives that specify exposure limit values and reference levels.

Chapter 2 presents the state of the art on near-field RF-EMF exposure, along with commonly used methods and protocols for assessing incident/transmitted power density induced by near-field sources through numerical simulations and measurements. The section concludes by summarizing the current methods, highlighting their limitations and applications.

Chapter 3 provides a detailed description of the case study, focusing on the analysis of human exposure in the near-field of the antenna based on transmitted power density. A new approach is proposed to directly evaluate the power density beneath the human tissue, taking into account the coupling and multi-reflection between the antenna and the human skin. The chapter compares the proposed method with the methods introduced in Chapter 2 for validation purposes and presents and interprets the results.

Chapter 4 introduces a non-invasive practical method for evaluating the absorbed power density (APD). This method considers the effect of coupling between the antenna and the human body, which alters the antenna's initial current and field. The chapter discusses the definition of multi-layer environments and dyadic Green's functions, and then inversely solves the electric field integral equation (EFIE) using the method of moments (MoM) to reconstruct the equivalent currents based on the electric field sampled on the surface of a hemisphere surrounding the antenna. The APD is evaluated using the equivalent currents below the air-phantom interface. The chapter concludes by reviewing the measurement requirements for a real test scenario, including the measurement uncertainty of the electric field and the required phantom size.

Finally, in Chapter 5, the thesis concludes by summarizing the significant contributions made in the research, including the proposed methods for assessing near-field RF-EMF exposure, evaluating power density, and considering the coupling effects between antennas and the human body. The conclusion also highlights avenues for future research, suggesting potential areas of exploration and development in the field of human exposure assessment.

Chapter 2

Literature review

2.1 Near-field region

The space surrounding the antenna can be divided into three regions: (a) the reactive near field, (b) the radiating near field (Fresnel zone), and (c) the far field (Fraunhofer region), as depicted in Figure 2.1. These regions are defined to characterize the field structure within each region. Although there are no abrupt changes in the field configurations when crossing the boundaries, there are noticeable distinctions among them. The boundaries separating these regions are not universally defined, although various criteria have been established and are commonly employed to delineate these regions [19].

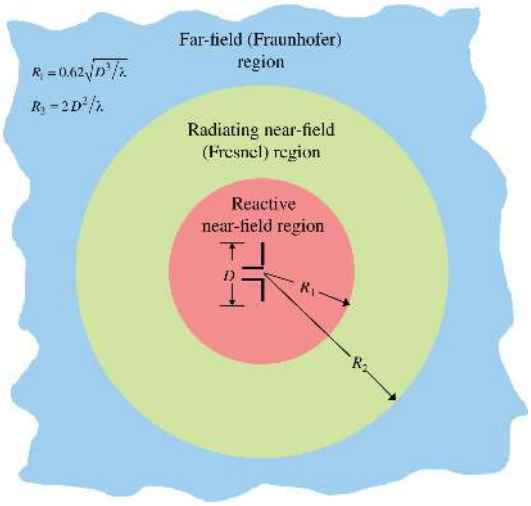

Figure 2.1: Field regions of an antenna [19].

- **Reactive near-field region:** The reactive near-field region is defined as the portion of the space in close proximity to the antenna where the reactive field predominates. Typically, the outer boundary of this region is located at a distance of R $< 0.62\sqrt{D^3/\lambda}$ from the antenna surface, where λ represents the wavelength and D denotes the largest dimension of the antenna [19].

- **Radiation near-field region (Fresnel zone):** The region between the reactive near-field region and the far-field region is referred to as the radiation near-field region or the Fresnel zone. In this region, the radiation fields dominate, and the angular field distribution depends on the distance from the antenna. In the case where the antenna's maximum dimensions are not significantly large compared to the wavelength, this region may not exist. For an infinitely focused antenna, the region close to the antenna is sometimes analogously referred to as the Fresnel region based on optical terminology. The inner boundary of this region is defined by the distance $R \leq 0.62\sqrt{D^3/\lambda}$, and the outer boundary is characterized by the distance $R < 2D^2/\lambda$, where D represents the largest dimension of the antenna. This criterion is based on the maximum phase error of $\pi/8$ [19].

- **Far-field region (Fraunhofer region):** In the far-field region, the fields exhibit a fully spherical nature, and the radial component of the field becomes negligible compared to the transverse components. This region is where the antenna's radiation pattern is formed, and most of the antenna's characteristic parameters are typically defined. Generally, the far-field region starts at a distance of $2D^2/\lambda$ from the antenna [19].

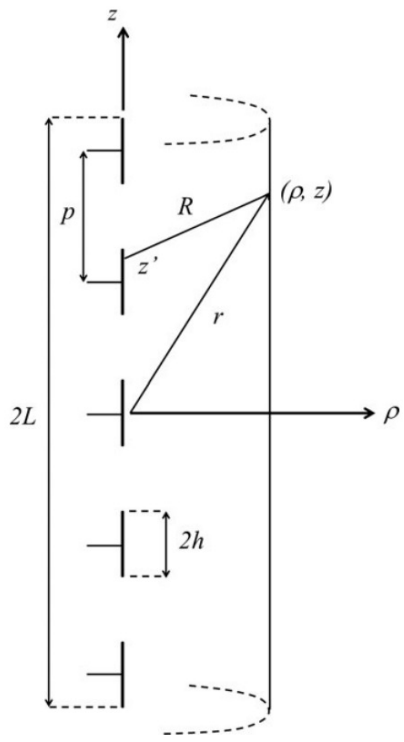

Figure 2.2: Collinear array geometry [45].

The revision of international standards necessitates the validation of power density (PD) measurements in the vicinity of RF sources. The presence of reactive energy in the near field can lead to an overestimation of PD measurements obtained using electric field probes. In the near field of antennas, strong RF fields are exchanged between the

electromagnetic sources and the surrounding space due to the exchange of EM energy among the metal parts of the antenna. This energy, known as reactive energy, does not radiate but remains localized around the antenna. Reactive energy is captured in E-field measurements and can cause high PD readings when conventional measuring instruments are placed near the metal parts of the antennas. Using such instruments, PD is assumed to be under far-field conditions, where the electric and magnetic fields are orthogonal, in phase, and naturally aligned with the direction of propagation, corresponding to the free space impedance of $\eta = 377\Omega$ (i.e., PD $= |E|^2/\eta$ or PD $= |H|^2 \times \eta$). The region around the antenna where non-propagating fields have a higher level than the propagating ones is referred to as the near-reactive field [45].

In the near-reactive field of RF sources, PD, which is a commonly used measure for far-field exposure, becomes challenging to define and measure. This is because EM emissions do not propagate in a straightforward manner due to the local E-field being the sum of contributions from different directions and amplitudes, which can rapidly change over short distances. The reactive energy from antennas can be absorbed by neighboring dissipative dielectric materials depending on the field impedance. The presence of the human body or other objects in close proximity can perturb the radiated energy and alter the antenna's current distribution, load impedance, field pattern, and energy absorption. E-field assessments conducted in the absence of the body are unable to provide an accurate evaluation [45].

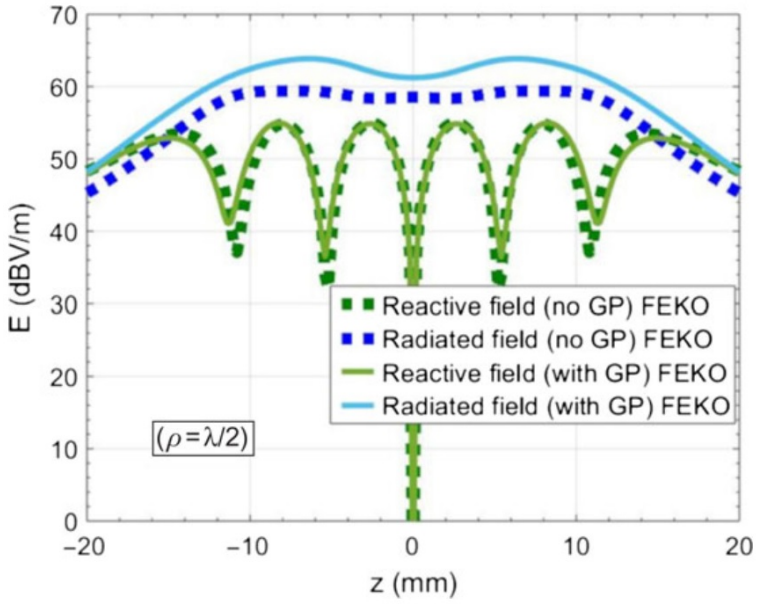

Figure 2.3: Near field of a 3-dipole collinear array with ground plane [45].

An analytical approach is presented in [45] to determine the boundary of the reactive near field and establish a method for accurate PD measurements in close proximity to collinear arrays of resonant cylindrical dipoles. Collinear arrays of dipoles antennas are commonly used in portable wireless products operating above 6 GHz. The boundary criteria for the radiative near field, defined in (2.1), represents the minimum distance at which the squared amplitude of the radiated field polarization E_z is equal to or greater

than that of the reactive field E_ρ for a dipole.

$$\min \rho \rightarrow |\mathbf{E_z}|^2 = |\mathbf{E}_\rho|^2, \tag{2.1}$$

where ρ is the distance that marks the transition from the reactive near field to radiated near field.

PD measurements at distances $\rho > \lambda/2$ can be considered appropriate for exposure assessment as they are less influenced by reactive E-field energy. If the available instrumentation can only measure $|E|^2$ without phase information, PD assessment should be limited to the radiative near field where reactive PD is significantly attenuated.

Based on the definitions of different antenna regions, two types of field conversion can be distinguished for different applications:

- **Forward propagation:** In this approach, the field measured in areas closer to the antenna is converted to the radiated field in areas further away. Typically, this method is employed to measure the radiation characteristics of small antennas. For example, the antenna field is measured in the near or very near field regions, and then the antenna pattern is calculated in the far-field region.

- **Backward propagation:** Also known as back projection, this method involves converting the field measured in areas far away from the antenna to areas closer to it. The purpose of this conversion is to conduct diagnostic studies on the antenna. Microwave holographic imaging, mentioned in the introduction section, is one of the significant examples of this type of field conversion.

When performing field conversion between different regions, it is essential to consider some general points. Firstly, the precise measurement location and its distance from the antenna under test must be known for the field to be transferred from one radiation region to another. Field transfer between different regions is possible when the field's phase, in addition to its amplitude, is available or can be determined using a suitable method. Having complete knowledge of the electric field or magnetic field information, along with the measurement location, enables the conversion of the field between different regions.

2.2 Reconstruction methods

In order to ensure the safe utilization of new wireless communication technologies, it is necessary to employ methods for assessing the compliance of wireless devices with exposure limits defined by international guidelines, standards, or national regulations. Specifically, the focus is on wireless communication devices such as mobile phones, tablets, and wearable antennas that are used in close proximity to the human body. Thus, evaluating the power density in the vicinity of these devices becomes crucial to verify compliance with exposure limits. The power density S passing through a sufficiently small area ds is expressed by the Poynting vector in Equation (1.14). This equation illustrates that obtaining the power density requires knowledge of both the electric and magnetic fields.

However, measuring both electric and magnetic fields near the device can be challenging in the compliance assessment process. The presence of coupling effects or multiple reflections between the Device Under Test (DUT) and the measurement probe can disturb the field distribution and compromise measurement accuracy.

Measuring absorbed power density near human tissue presents even greater challenges and complexities. The proximity of the antenna to the tissue, the thickness of the measurement probe, the coupling effects between the probe and the antenna, as well as the coupling effects between the antenna and the human body are parameters that hinder direct measurement of the electric field. Consequently, field conversion methods can be utilized to obtain the electric field at the desired point, which will be discussed in detail later.

2.2.1 Modal expansion method

Modal expansion methods have a long history and serve as one of the earliest approaches for converting near-fields and far-fields. These methods were initially introduced in 1965 and subsequently led to the development of test devices in 1970 [46]. The fundamental principles underlying these methods involve expressing the radiation from an antenna as an expansion of plane waves, cylindrical waves, or spherical waves with unknown coefficients. These coefficients are then determined through measurements of the field, allowing for the assessment of the radiation field throughout space. In the context of human exposure, two widely utilized modal expansion methods, namely plane-wave expansion and spherical wave expansion, are commonly employed.

2.2.1.1 Plane-wave spectrum method

In the simplest case of the modal expansion method, when both the measured and reconstructed fields are in Cartesian coordinates, the transformation of the fields can be computed using the spatial Fourier transform. The plane wave spectrum (PWS) or plane-to-plane (PTP) method is based on the representation of an electromagnetic wave as a collection of plane waves [47]. It is commonly employed for reconstructing the antenna pattern in the far-field region from near-field measurements [48]. Figure 2.4 illustrates a schematic view of power density evaluation near the device using this method. The PWS technique involves performing a back-projection (or back-transformation) of the E- and H-field components tangent to the measurement plane at $z = z_0$ onto the evaluation plane, as depicted in Figure 2.4 [49]. According to the Huygens principle, each point of a wave can be considered as a secondary source that emits a wave propagating with the same initial velocity in space. Consequently, the plane wave spectrum in the $z = z_0$ plane is obtained by summing the contributions of plane waves from all directions.

The reconstruction of the E-field, represented as the phasor E, can be obtained using the following formula [48]:

$$\mathbf{E}(\overrightarrow{r}) = \frac{1}{2\pi^2}\int_{-\infty}^{\infty}\int_{-\infty}^{\infty}\boldsymbol{\mathscr{E}}(k_x,k_y)e^{-j\overrightarrow{\mathbf{k}}\cdot\overrightarrow{r}}dk_xdk_y, \tag{2.2}$$

where $\boldsymbol{\mathscr{E}}(k_x,k_y)$ is electric field in wave-number domain, $\overrightarrow{r}$ is the Cartesian coordinates (x,y,z), therefore: $E(\overrightarrow{r}) = E_x(\overrightarrow{r})\overrightarrow{x} + E_y(\overrightarrow{r})\overrightarrow{y} + E_z(\overrightarrow{r})\overrightarrow{z}$, and $\overrightarrow{k}$ denotes the wavenumber vector in Cartesian coordinates (x,y,z): $\overrightarrow{k} = k_x\overrightarrow{x} + k_y\overrightarrow{y} + k_z\overrightarrow{z}$. $\mathbf{E}$ is the E-field in the wavenumber domain (angular spectrum of $E(x,y,z_0)$) defined as

$$\boldsymbol{\mathscr{E}}_{\boldsymbol{x,y}}(k_x,k_y) = \int_{-\infty}^{\infty}\int_{-\infty}^{\infty}\mathbf{E}_{\mathbf{x,y}}(x,y,z_0)e^{j\overrightarrow{\mathbf{k}}\cdot\overrightarrow{r}}dxdy \tag{2.3}$$

$$\boldsymbol{\mathscr{E}_z}(k_x, k_y) = -\frac{k_x \boldsymbol{\mathscr{E}_x}(k_x, k_y) + k_y \boldsymbol{\mathscr{E}_y}(k_x, k_y)}{k_z} \tag{2.4}$$

where k_z is wave number in z-direction: $k_z^2 = k_0^2 - k_x^2 - k_y^2$, where k_0 denotes the wavenumber in vacuum, which is obtained by dividing 2π by the wavelength λ. For $k_x^2 + k_y^2 \leq k_0^2$, the plane waves are propagating while the waves corresponding to $k_x^2 + k_y^2 \geq k_0^2$ decay exponentially with increasing z. The evanescent waves characterize the stored energy or the reactive near field.

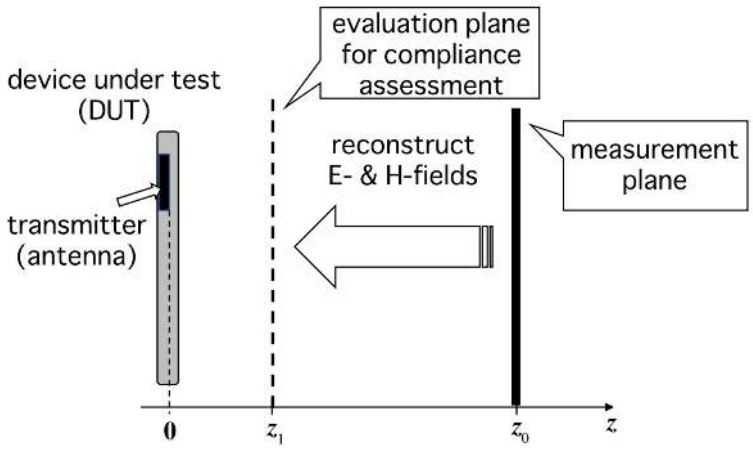

Figure 2.4: Schematic view of assessment using back-transform technique [49].

Evanescent modes, which can be dominant in close proximity to an antenna, are theoretically represented in the wavenumber domain if the Nyquist limit for the measurement plane fields is satisfied. However, in practical measurements, when the measurement plane is located at a distance of several wavelengths from the antenna under test (DUT), it becomes challenging to determine the contribution of evanescent modes to the fields accurately. These modes decay exponentially as the distance between the measurement plane and the antenna increases.

In close proximity to the human body, a portion of the energy stored around the antenna may couple into the tissue, potentially affecting human exposure. The power density evaluated in free space does not directly measure this effect. Therefore, to evaluate this factor, the transmitted field into the human body needs to be considered in the assessment of total power density (TPD). Consequently, for each wave of the angular spectrum representation incident on the body surface, denoted as $\boldsymbol{\mathscr{E}inc}$, there will be a corresponding transmitted plane wave, $\boldsymbol{\mathscr{E}tx}$, such that

$$\boldsymbol{\mathscr{E}_{tx}}(k_x, k_y) = \boldsymbol{\Pi_{skin}}(k_x, k_y) \boldsymbol{\mathscr{E}_{inc}}(k_x, k_y), \tag{2.5}$$

where Π_{skin} is the spectral transmission operator [50] for the planar interface ($z = z_{skin}$) corresponding to the tissue model surface. The PWS of the magnetic field, determined solving Maxwell's equations, is:

$$\boldsymbol{\mathscr{H}_{tx}}(k_x, k_y) = \frac{1}{\omega\mu}[\vec{\mathbf{k}} \times \boldsymbol{\mathscr{E}_{tx}}(k_x, k_y)], \tag{2.6}$$

where ω and μ are respectively the angular frequency and the permeability inside the lossy tissue media, and $\mathscr{H}_{tx}$ is the transmitted magnetic field in wave-number domain. Then the transmitted H-field in frequency domain can be evaluate by (2.2).

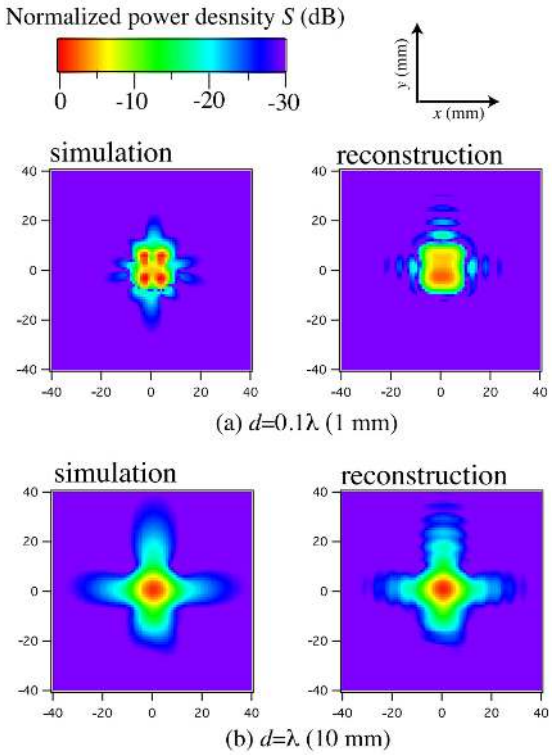

Figure 2.5: Power density distributions of the array antenna at 30 GHz with separation distances d of (a) 0.1λ (1 mm) and (b) λ (10 mm) [49].

In [49], a near-field reconstruction technique is presented for assessing power density using back-transformation based on measurements of two vector components of the electric field tangential to the measurement plane at frequencies of 15, 30, 60, and 100 GHz. The measurements were conducted in the absence of the human body, with the measurement plane located at a distance of 5λ away from the device under test (DUT). Figure 2.5 illustrates that the power density distribution is influenced by the coupling between the antenna and the human body, which becomes significant at short separation distances. The reconstruction error was found to be within 0.32 dB, ensuring accurate assessment of the maximum spatially averaged power density under conditions where the averaging area A $\geq \lambda^2$ and the separation distance d $\geq 0.2\lambda$. The study also revealed that the measurement system requires a minimum detection limit of -30 dB below the peak of the measured E-field to accurately assess the maximum power density (S_A) and minimize phase measurement uncertainty within a 20-degree range at a 95% confidence level.

In [51], the impact of measurement uncertainties in the amplitude and phase of the electric field is estimated. In addition to the findings presented in [49], it was observed that the accuracy of phase measurement has a greater influence on determining the maximum spatially averaged power density compared to the accuracy of amplitude measurement. However, these effects do not compromise the overall accuracy of the power density estimation in the near-field when using the reconstruction technique.

2.2.1.2 Spherical wave expansion

Maxwell's equations in a linear, isotropic and homogeneous medium are as follows ($\exp(-j\omega t)$ time-dependency)

$$\nabla \times \overrightarrow{\mathbf{H}} = -j\omega\varepsilon\overrightarrow{\mathbf{E}} + \overrightarrow{\mathbf{J}} \tag{2.7}$$

$$\nabla \times \overrightarrow{\mathbf{E}} = j\omega\mu\overrightarrow{\mathbf{H}} - \overrightarrow{\mathbf{M}} \tag{2.8}$$

where $\overrightarrow{H}$ and $\overrightarrow{E}$ are the magnetic and electric field vectors, ω is the angular frequency, and ε and μ permittivity and permeability, respectively, of the medium. The assumed sources are $\overrightarrow{J}$ (electric current density) and $\overrightarrow{M}$ (magnetic current density).

The electric and magnetic fields in a source-free region of space can be decomposed into spherical waves, which are defined in spherical coordinates (r, θ, φ) with corresponding unit vectors ($\hat{r}$, $\hat{\theta}$, $\hat{\varphi}$). This decomposition is known as the spherical-wave modal expansion (SWE).

$$\overrightarrow{\mathbf{E}}(r,\theta,\varphi) = \frac{k}{\sqrt{\eta}} \sum_{csmn} Q^{(c)}_{smn}\, \overrightarrow{\mathbf{F}}^{(c)}_{smn}(r,\theta,\varphi) \tag{2.9}$$

To obtain $\overrightarrow{H}$, (2.9) can be substituted into (2.8)

$$\overrightarrow{\mathbf{H}}(r,\theta,\varphi) = -jk\sqrt{\eta} \sum_{csmn} Q^{(c)}_{smn}\, \overrightarrow{\mathbf{F}}^{(c)}_{3-s,m,n}(r,\theta,\varphi) \tag{2.10}$$

where k is the propagation constant, η is the wave impedance, c is the index that represents the radial function, n is the modal degree ($n = 1, 2, 3, \cdots, \infty$), m is the order that is limited by ($m \leq |n| = -n, \cdots, -1, 0, 1, \cdots, n$), s is the index that takes the value 1 for TE and 2 for TM, $\overrightarrow{F}^{(c)}_{smn}(r,\theta,\varphi)$ is the spherical wave functions at point (r,θ,φ), $Q^{(c)}_{smn}$ are the modal coefficient which are unknown.

The wave functions $\overrightarrow{F}smn^{(c)}(r,\theta,\varphi)$ are dimensionless, and the additional factors in front of the summation signs in (2.9) and (2.10) are necessary to obtain the dimension of watts$^{1/2}$ for the wave coefficients $Qsmn^{(c)}$. With this convention, the expression for the power P radiated by outward traveling modes is simplified as much as possible [52].

$$P = \frac{1}{2} \sum_{csmn} |Q^{(3)}_{smn}|^2 \quad watts \tag{2.11}$$

The choice of $c = 3$ and 4 indicates inward and outward propagating waves, repectively.

Spherical near-field measurements have found extensive applications in the antenna industry [53]. The spherical wave expansion (SWE) technique is commonly employed to derive antenna characteristics. This technique has been utilized to determine the free-space electromagnetic field (EMF) level in the immediate vicinity of the antenna [54–56].

The measurement system, as depicted in Figure 2.6, is designed to determine the spherical modal coefficients from the tangential field on the surface of the measurement sphere. Once the modal coefficients are determined, the fields can be derived using (2.9) and (2.9) in all regions except for $r < r_0$, where r_0 represents the radius of the minimum sphere that completely encloses the antenna.

In [54], the SWE technique is utilized to determine the incident power density, which is then used as input for the total-field/scattered-field (TF/SF) finite-difference time-domain

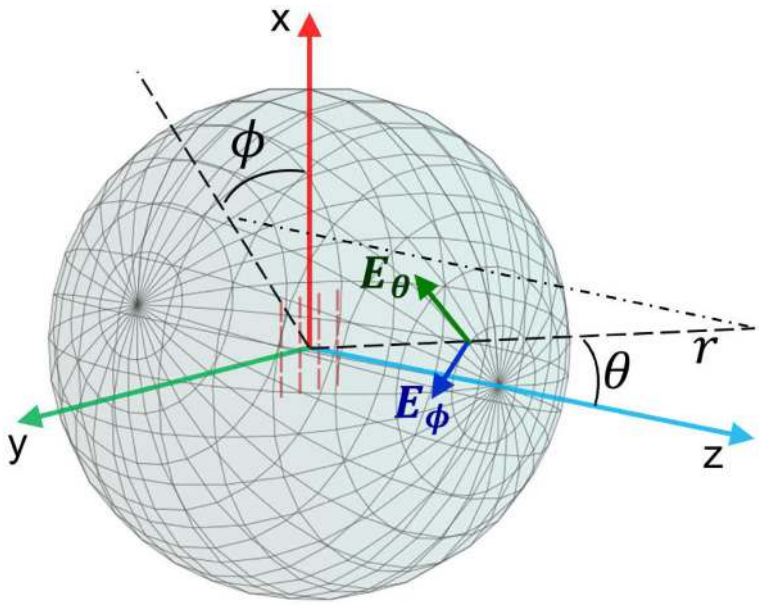

Figure 2.6: Schematic of the spherical measurement system of the antenna [54].

(FDTD) method to assess the absorbed power density at 28 GHz. The total power is also of interest to understand the power absorption. For example, in [57], a dipole antenna is positioned inside an air bubble, and both are located within a lossy medium sphere representing a human body model. The total radiated power is illustrated in Figure 2.7.

In [58], the Green's function for a layered sphere is obtained by superposition of spherical harmonic functions, and the method of auxiliary sources (MAS) is employed to model the interaction between a layered sphere head model and a dipole antenna. This approach is used to assess the specific absorption rate (SAR) inside the human head model. However, extending this method to a non-spherical shaped head model presents significant challenges.

In [59], a new hybrid numerical approach between the Method of Moments (MoM) and the Null Field Method (NFM) is rigorously analyzed to investigate the interaction of electromagnetic radiation from a cell phone antenna with a human head model. The NFM method is utilized to solve the electromagnetic scattering problem from the head model, while spherical waves are employed to determine the field inside a prolate head model based on the induced current generated by the antenna in close proximity to the model's surface. Then, the MoM is used to solve the electromagnetic radiation problem from the handset antenna. A convergent iteration process is proposed to handle the interaction between the head model and the antenna.

2.2.2 Equivalent currents method

The method of equivalent currents or surface reconstruction current was first proposed in 1990 [60]. As shown in Figure 2.8, the surface reconstruction current method is based on the equivalence principle. By applying this principle, an electric field integral equation (EFIE) or magnetic field integral equation (MFIE) for the radiated field can be formulated. These integral equations are then solved using the inverse method of moments on the

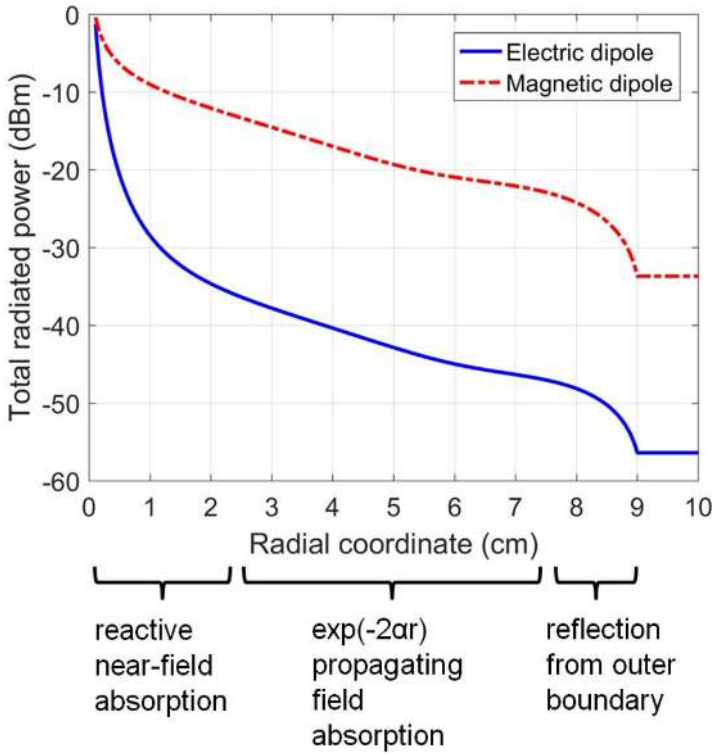

Figure 2.7: Total radiated power vs radial distance [57].

desired surface to reconstruct the current on the surface of the antenna. The reconstructed current can be used to calculate the radiated fields from the antenna at any distance.

One advantage of using surface reconstruction current methods is their applicability to complex and three-dimensional surfaces. Unlike modal expansion methods, there is no specific sampling rate requirement, and the accuracy of the reconstructed surface current improves with a higher number of samples. Additionally, these methods allow for the reconstruction of fields at any distance from the antenna, which has attracted significant attention in recent years.

Initially, the surface reconstruction current method was developed to reconstruct only the magnetic current on a flat and infinitely large perfect electric conductor (PEC) surface [30]. Subsequently, the reconstruction of the electric current on a flat and infinitely large perfect magnetic conductor (PMC) surface was investigated [31]. In 2007, the reconstruction of electric and magnetic currents simultaneously and on arbitrary surfaces was considered [33]. Since then, this method has gained more attention in diagnostic applications.

The Equivalent Current (EQC) method is based on a dual-equation formulation [61], where one equation describes the radiation of the measured field by the EQC, and the other equation enforces Love's equivalence theorem. Using this method, the electric and magnetic EQC over a reconstruction surface enclosing the Device Under Test (DUT) can be reconstructed using intermediate field (IF) or far-field (FF) data. The reconstructed EQC can then be utilized to calculate the field strength outside the reconstruction surface.

Figure 2.8 depicts an antenna in free-space with the aperture surface S_0. By considering the surface equivalent theory, the entire space can be divided into the half-space

below ($z < 0$) and the half-space above ($z > 0$). Love's equivalence principle and image theory suggest that the fields in the half-space below the plane of equivalent currents are zero, while the equivalent currents on the XY-plane radiate the fields in the half-space above the plane of equivalent currents [60].

According to Figure 2.8, the magnetic surface current $\overrightarrow{\mathbf{M}}$ exists only on S_0 and can be defined as follows:

$$\overrightarrow{\mathbf{M}} = 2\overrightarrow{\mathbf{E}} \times \hat{n}, \tag{2.12}$$

where $\overrightarrow{\mathbf{E}}$ is the E-field vector, $\hat{n}$ is the unit vector normal to the surface.

Since the field in the half-space above the plane of equivalent currents ($\overrightarrow{\mathbf{E}}(\overrightarrow{\mathbf{M}})$) is caused by $\overrightarrow{\mathbf{M}}$, the determination of $\overrightarrow{\mathbf{M}}$ can be achieved by measuring the field in the half-space above the XY-plane ($\overrightarrow{\mathbf{E}}_{\mathbf{meas}}$). The equation for finding $\overrightarrow{\mathbf{M}}$ can be solved using (2.13), yielding the following result:

$$\overrightarrow{\mathbf{E}}_{\mathbf{meas}} = \overrightarrow{\mathbf{E}}(\overrightarrow{\mathbf{M}}). \tag{2.13}$$

The E-field at any point in the half-space above the XY-plane can be found from

$$\overrightarrow{\mathbf{E}}(\overrightarrow{r}) = -\iint_{S_0} [\overrightarrow{\mathbf{M}}(\overrightarrow{r'}) \times \nabla' g(\overrightarrow{r}, \overrightarrow{r}')] ds', \tag{2.14}$$

where $\mathbf{E}(r)$ is E-field of an arbitrary observation point r, $\overrightarrow{\mathbf{M}}(r')$ is the equivalent magnetic current at the source point r', ∇' is the gradient operator according to the prime variables, and $g(r, r')$ is the three-dimensional Green's function

$$g(\overrightarrow{r}, \overrightarrow{r}') = \frac{e^{-jk_0|\overrightarrow{r}-\overrightarrow{r}'|}}{4\pi|\overrightarrow{r} - \overrightarrow{r}'|}, \tag{2.15}$$

where $k_0 = \omega\sqrt{\mu_0 \varepsilon_0}$ is the free-space wavenumber.

In the case of planar scanning, the near-field measurement is conducted over a planar surface, which is assumed to be parallel to the source plane. This configuration is depicted in Figure 2.9. The aperture of the antenna (S_0) is considered as a rectangular plate in the XY-plane with dimensions W_x and W_y. The distance between the source plane (S_0) and the measurement plane is denoted as d. During planar scanning, it is typical to measure the x and y components of the electric near fields. However, if the contribution of evanescent modes is significant, the z component of the electric near field should also be taken into account.

By considering the x-, y-, and z-components of the measured electric near fields in (2.14), we can derive the following integral equation for the equivalent magnetic currents.

$$\begin{bmatrix} \mathbf{E}_{\mathbf{meas,x}}(\overrightarrow{r}) \\ \mathbf{E}_{\mathbf{meas,y}}(\overrightarrow{r}) \\ \mathbf{E}_{\mathbf{meas,z}}(\overrightarrow{r}) \end{bmatrix} = -\iint_{S_0} \begin{bmatrix} 0 & \frac{\partial g(\overrightarrow{r}, \overrightarrow{r}')}{\partial z'} \\ -\frac{g(\overrightarrow{r}, \overrightarrow{r}')}{\partial z'} & 0 \\ \frac{g(\overrightarrow{r}, \overrightarrow{r}')}{\partial y'} & -\frac{g(\overrightarrow{r}, \overrightarrow{r}')}{\partial x'} \end{bmatrix} \begin{bmatrix} \mathbf{M}_{\mathbf{x}}(\overrightarrow{r}') \\ \mathbf{M}_{\mathbf{y}}(\overrightarrow{r}') \end{bmatrix} ds' \tag{2.16}$$

It is evident from (2.16) that the obtained integral equation is a decoupled one with respect to the two components of magnetic currents. So instead of solving (2.16), the

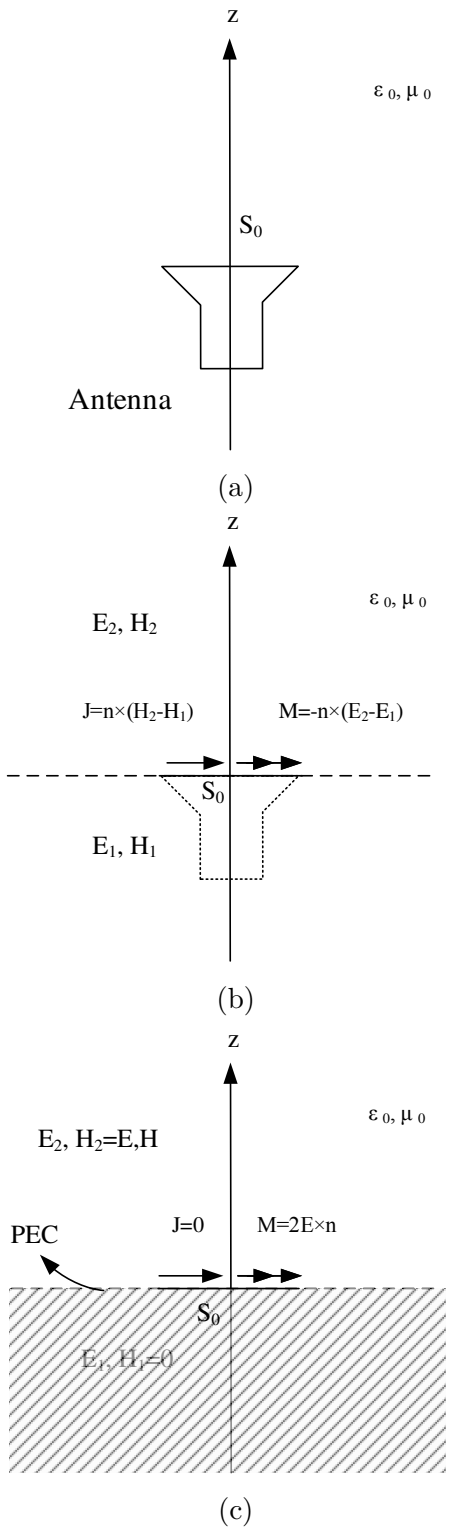

Figure 2.8: (a) structure (b) Surface equivalent theory (c) Love's equivalent principle and Image theory

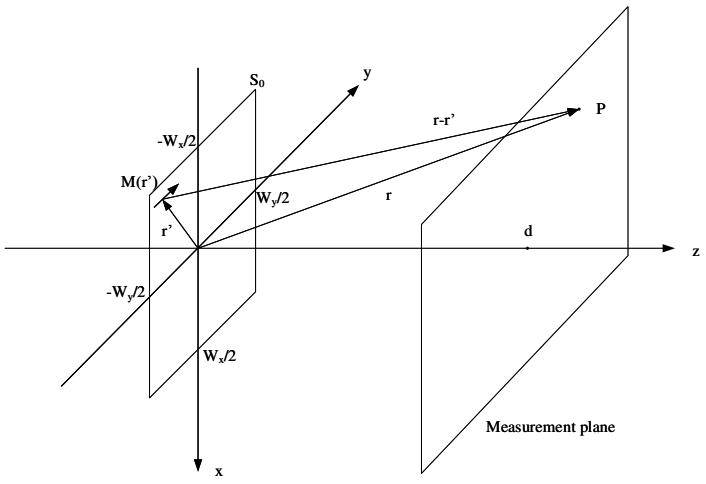

Figure 2.9: Planar scanning.

following two simple integral equations can be solved separately

$$\begin{aligned}
\mathbf{E_{meas,x}}(\overrightarrow{r}) &= -\iint_{S_0} \frac{\partial g(\overrightarrow{r},\overrightarrow{r}')}{\partial z'}\mathbf{M_y}(\overrightarrow{r}')ds' \\
\mathbf{E_{meas,y}}(\overrightarrow{r}) &= \iint_{S_0} \frac{\partial g(\overrightarrow{r},\overrightarrow{r}')}{\partial z'}\mathbf{M_x}(\overrightarrow{r}')ds' \\
\mathbf{E_{meas,z}}(\overrightarrow{r}) &= \iint_{S_0} \left(\frac{\partial g(\overrightarrow{r},\overrightarrow{r}')}{\partial y'}\mathbf{M_x}(\overrightarrow{r}') - \frac{\partial g(\overrightarrow{r},\overrightarrow{r}')}{\partial x'}\mathbf{M_y}(\overrightarrow{r}')\right) ds'
\end{aligned} \tag{2.17}$$

The current method utilizing the equivalent magnetic current approach offers numerical efficiency advantages over the equivalent electric current approach in the case of planar scanning. The integral equation decouples, simplifying the solution of large matrix problems. Once the E-field integral equations are formulated, a Method of Moment (MOM) procedure is employed to convert them into matrix equations.

2.2.2.1 Method of moment

In the previous section, we addressed the problem of determining the unknown current distribution on a surface. The key approach of the Method of Moments is to express the unknown parameter as a combination of known functions with undetermined coefficients. By imposing the boundary conditions, in this case, the electric field in the measurement plane, we transformed the equation into a system of linear equations (e.g., Eq. (2.17)). The next step involved numerically solving this linear system to find the unknown coefficients (see Section 2.2.2.1.2.1). To further advance this process, we introduce the weighted residual method or the Method of Moments. When considering the general problem, we encounter [62].

$$\mathscr{L}(f) = g \tag{2.18}$$

where $\mathscr{L}$ is a linear operator, g is a known function and f is an unknown function. In electromagnetic problems, $\mathscr{L}$ is usually an integral operator, f is electric or magnetic

current, and g is a incident field alone or together with scattered field. Now, we expand f to the sum of N weighted basis functions

$$f = \sum_{n=1}^{N} a_n f_n \tag{2.19}$$

where a_n are unknown coefficients and f_n are basis functions. Since $\mathscr{L}$ is linear, by substituting the (2.19) into the (2.18) we have

$$\sum_{n=1}^{N} a_n \mathscr{L}(f_n) \approx g, \tag{2.20}$$

and the residue is defined as follows

$$R = g - \sum_{n=1}^{N} a_n \mathscr{L}(f_n) \tag{2.21}$$

The basis functions f_n are chosen to model the expected behavior of the unknown function throughout its domain and may be scalar or vector, depending on the problem.

We now assume that the boundary conditions have already been applied. Thus, we define an inner product between the basic function $f_n(r')$ and the test or weighted function $f_m(r)$.

$$< f_m, f_n >= \int_{f_m} f_m(r) \cdot \int_{f_n} f_n(r')dr'dr \tag{2.22}$$

It can be line, surface, or volume integrals depending on the support of the basis and test functions. It is required that the inner product of each test function with the residual function must be zero

$$\sum_{n=1}^{N} a_n < f_m, \mathscr{L}(f_n) >=< f_m, g > \tag{2.23}$$

Which leads to a $N \times N$ matrix equation equal to **Za=b**, where the elements of the **Z** matrix are equal to

$$Z_{mn} =< f_m, \mathscr{L}(f_n) > \tag{2.24}$$

and the elements of the vector on the right side of the equation are equal to

$$b_m =< f_m, g > \tag{2.25}$$

In electromagnetic problems, basis functions interact with other functions through Green's function, resulting in a full matrix **Z**. This is in contrast to other methods, such as the finite element method, where the matrix is typically sparse, symmetric, and banded, with many elements of each row being zero [63].

2.2.2.1.1 Point matching

Solving the integral equation (2.18) by applying boundary conditions at discrete points is possible. By choosing the Dirac delta function as the test function, we obtain:

$$f_m(r) = \delta(r) \tag{2.26}$$

This method is known as point matching or point collocation. It has both advantages and disadvantages. One advantage is that when evaluating matrix elements, there is no need to integrate over the range of the test function; only the source function needs to be considered, which can simplify the evaluation of matrix elements. The main disadvantage is that the boundary conditions are only applied at discrete locations throughout the domain. This method is typically used in problems involving dyadic Green's functions, which include Sommerfeld integrals and do not have a closed form solution [64].

2.2.2.1.2 Galerkin method

When selecting the test function, we have the freedom to choose from various functions based on the problem at hand. However, for most problems, the choice of test function plays a crucial role in obtaining an accurate solution. One commonly used approach is the Galerkin method, where basis functions are employed as test functions. Unlike the point matching method, the advantage of the Galerkin method is that it allows for the application of boundary conditions throughout the entire domain, rather than solely at discrete points. However, this advantage comes at the expense of increased complexity and computational time required for evaluating the matrix elements. Many MoM problems in the literature adopt the Galerkin method as the standard approach.

2.2.2.1.2.1 Pulse basis function

A set of one-dimensional pulse basis functions is shown in Figure 2.10, where the domain is divided into N points with $N-1$ subsections or pulses. It is assumed that the pieces are all of equal lengths, although this requirement is not mandatory. One-dimensional pulse basis functions can be defined as follows:

$$f_n(x) = 1, \quad x_n \leq x \leq x_{n+1} \tag{2.27}$$

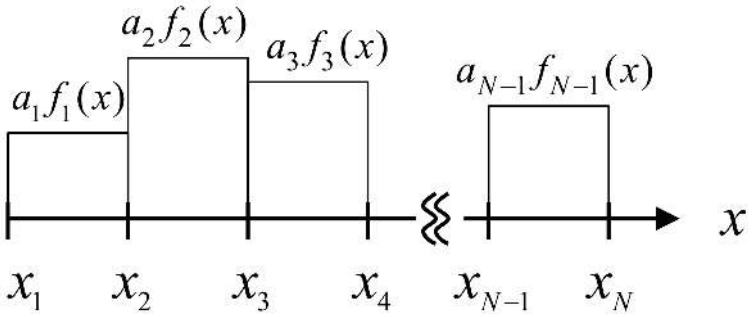

Figure 2.10: Pulse basis function [62].

The basis function is zero in the remaining points. Pulse functions provide a straightforward approximation to solve in each section but can significantly simplify the evaluation of MoM matrix elements.

In practical electromagnetism problems, two-dimensional functions are commonly employed. The problem depicted in Figure 2.9 is solved using two-dimensional pulse basis

functions as follows. Equally spaced two-dimensional pulse basis functions approximate both components of the equivalent magnetic currents ($\mathbf{M_x}$, $\mathbf{M_y}$).

$$\begin{aligned}\mathbf{M_x}(x',y') &= \sum_{i=1}^{M}\sum_{j=1}^{N}\alpha_{ij}\mathbf{\Pi_{ij}}(x',y') \\ \mathbf{M_y}(x',y') &= \sum_{i=1}^{M}\sum_{j=1}^{N}\beta_{ij}\mathbf{\Pi_{ij}}(x',y')\end{aligned} \tag{2.28}$$

where α_{ij} and β_{ij} are the unknown amplitudes of the x and y directed magnetic currents, respectively on the ijth patch, and $\mathbf{\Pi_{ij}}(x',y')$ is the two-dimensional pulse basis function of the ijth patch and defined as

$$\mathbf{\Pi_{ij}}(x',y') = \begin{cases} 1 & x_i - \frac{\Delta x}{2} \leq x' \leq x_i + \frac{\Delta x}{2}, y_i - \frac{\Delta y}{2} \leq y' \leq y_i + \frac{\Delta y}{2}, \\ 0 & otherwise. \end{cases} \tag{2.29}$$

For the above approximation, the aperture plane (S_0) on which the equivalent magnetic currents reside is assumed to be a rectangular one in the XY-plane with extensions $-W_x/2 \leq x \leq W_x/2$ and $-W_y/2 \leq y \leq W_y/2$ as shown in Figure 2.9. The aperture plane (S_0) is divided into $M \cdot N$ equally spaced rectangular patches with dimensions Δx and Δy.

$$\begin{aligned}\Delta x &= W_x/M \\ \Delta y &= W_y/N\end{aligned} \tag{2.30}$$

In 2.29, x_i and y_i are the x and y coordinates of the center of the ijth patch and are given by

$$\begin{aligned}x_i &= -W_x/2 - \Delta x/2 + i\Delta x \\ y_i &= -W_y/2 - \Delta y/2 + i\Delta y\end{aligned} \tag{2.31}$$

It is important to note that these simple pulse basis functions can be used to approximate the magnetic currents because the integral equations do not contain any derivative of these currents. This is a consequence of the previous assumption that the field points and the measurement points are always outside the current-carrying region (S_0)

Since it is assumed that the measured electric near-fields are known at discrete points on the scanning plane, a point matching procedure is chosen.

By substituting 2.28 into 2.17 and utilizing point matching, the following matrix equation are obtained:

$$\begin{bmatrix}\mathbf{E_{meas,x}} \\ \mathbf{E_{meas,y}} \\ \mathbf{E_{meas,z}}\end{bmatrix} = \begin{bmatrix}0 & -\mathbf{G_z}(r) \\ \mathbf{G_z}(r) & 0 \\ -\mathbf{G_y}(r) & \mathbf{G_x}(r)\end{bmatrix} \cdot \begin{bmatrix}\mathbf{M_x} \\ \mathbf{M_y}\end{bmatrix} \tag{2.32}$$

where $\mathbf{Emeas}, \mathbf{x}$, $\mathbf{Emeas}, \mathbf{y}$, and $\mathbf{Emeas}, \mathbf{z}$ are vectors that contain the x, y, and z components of the measured electric near-fields, respectively. $\mathbf{M_x}$ and $\mathbf{M_y}$ are vectors that contain the unknown coefficients αij and β_{ij}, respectively. $\mathbf{G_x}(r)$, $\mathbf{G_y}(r)$, and $\mathbf{G_z}(r)$ are the discretized integrals of the free-space Green's function at the point $r = (x, y, z)$, derived with respect to x, y, and z [60]. They are matrices of dimensions $1 \times n_{src}$, where

n_{src} is the length of the vectors $\mathbf{M_x}$ and $\mathbf{M_y}$. A simple matrix multiplication then yields the field components $\mathbf{E_x}$, $\mathbf{E_y}$, and $\mathbf{E_z}$ at the point r. In other words, the ith element of the matrices $\mathbf{G_x}(r)$, $\mathbf{G_y}(r)$, and $\mathbf{G_z}(r)$, denoted as G_x^i, G_y^i, and G_z^i respectively, represents the radiated field of the ith magnetic current element at the observation point r. The value of this element is found from:

$$
\begin{aligned}
G_x^i &= -\frac{1}{4\pi}\int_{S^i}\frac{\partial}{\partial x}\frac{e^{-jk_0|\overrightarrow{r}-\overrightarrow{r}_0|}}{|\overrightarrow{r}-\overrightarrow{r}_0|}ds = \frac{1}{4\pi}\int_{S^i}\frac{e^{-jk_0|\overrightarrow{r}-\overrightarrow{r}_0|}}{|\overrightarrow{r}-\overrightarrow{r}_0|^2}(x-x_0)\left(jk_0+\frac{1}{|\overrightarrow{r}-\overrightarrow{r}_0|}\right)\\
G_y^i &= -\frac{1}{4\pi}\int_{S^i}\frac{\partial}{\partial y}\frac{e^{-jk_0|\overrightarrow{r}-\overrightarrow{r}_0|}}{|\overrightarrow{r}-\overrightarrow{r}_0|}ds = \frac{1}{4\pi}\int_{S^i}\frac{e^{-jk_0|\overrightarrow{r}-\overrightarrow{r}_0|}}{|\overrightarrow{r}-\overrightarrow{r}_0|^2}(y-y_0)\left(jk_0+\frac{1}{|\overrightarrow{r}-\overrightarrow{r}_0|}\right)\\
G_z^i &= -\frac{1}{4\pi}\int_{S^i}\frac{\partial}{\partial z}\frac{e^{-jk_0|\overrightarrow{r}-\overrightarrow{r}_0|}}{|\overrightarrow{r}-\overrightarrow{r}_0|}ds = \frac{1}{4\pi}\int_{S^i}\frac{e^{-jk_0|\overrightarrow{r}-\overrightarrow{r}_0|}}{|\overrightarrow{r}-\overrightarrow{r}_0|^2}(z-z_0)\left(jk_0+\frac{1}{|\overrightarrow{r}-\overrightarrow{r}_0|}\right)
\end{aligned}
\tag{2.33}
$$

where r_0 denotes the position of the magnetic current which extends over the area S_i.

If the number of measuring points is equal to the number of current elements, the solution to (2.32) is unique. However, if the number of measured near-field points is larger than the number of current elements, a least-squares solution is obtained.

The Gaussian quadrature technique can be employed to numerically solve the integrals in (2.33) over each current patch, while the Conjugate Gradient (CG) method can be utilized to solve the matrix (2.32).

2.2.2.1.2.2 RWG basis function

Pulse basis functions used for discretizing integral equations suffer from the drawback of discontinuity in meshes. The currents obtained within each rectangular mesh using these functions are not related to the adjacent meshes. To achieve better resolution and imaging in the reconstruction, Rao-Wilton-Glisson (RWG) basis functions are employed on triangular meshes [65]. To implement this approach, the structure is first discretized with triangular meshes, ensuring that the edge length of each mesh is smaller than $\lambda/10$. The electric current on triangular meshes, using RWG basis functions, is expanded as follows:

$$
\begin{aligned}
\overrightarrow{M}_{eq}(\overrightarrow{r}') &= \sum_{n=1}^{N} I_{M_n}\overrightarrow{f_n}(\overrightarrow{r}')\\
\overrightarrow{J}_{eq}(\overrightarrow{r}') &= \sum_{n=1}^{N} I_{J_n}\overrightarrow{f_n}(\overrightarrow{r}')
\end{aligned}
\tag{2.34}
$$

where I_{M_n} and I_{J_n} are the complex coefficients corresponding to the nth edge in the triangular meshing. The RWG basis function, denoted as $\overrightarrow{f_n}(\overrightarrow{r}')$, is defined on each edge and depicted in Figure 2.11.

$$
\overrightarrow{f}_n(\overrightarrow{r}') = \begin{cases} \frac{L_n}{2A_n^+}\overrightarrow{\rho}_n^+(\overrightarrow{r}') & \overrightarrow{r}' \; in \; T_n^+, \\ \frac{L_n}{2A_n^-}\overrightarrow{\rho}_n^-(\overrightarrow{r}') & \overrightarrow{r}' \; in \; T_n^-, \\ 0 & otherwise. \end{cases}
\tag{2.35}
$$

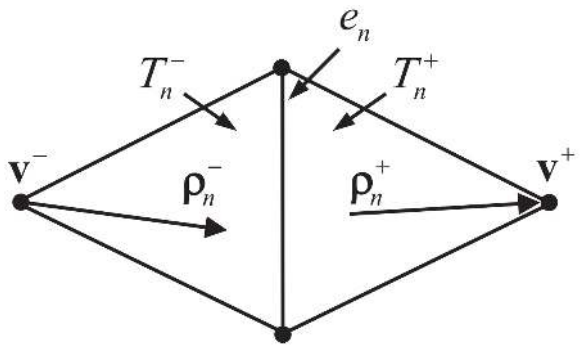

Figure 2.11: RWG basis function [62].

where T_n^+ and T_n^- are a pair of triangles with area A_n^+ and A_n^-, respectively, which share n edges and L_n is the length of the nth edge Is. In T_n^+, the vector $\overrightarrow{\rho}_n^+(\overrightarrow{r}')$ points to the vertex v^+ opposite the n edge and is equal to

$$\overrightarrow{\rho}_n^+(\overrightarrow{r}') = v^+ - \overrightarrow{r}', \quad \overrightarrow{r}' \; in \; T_n^+ \tag{2.36}$$

and in T_n^-, $\overrightarrow{\rho}_n^-(\overrightarrow{r}')$ is separated from the opposite vertex of v^- and is equal to

$$\overrightarrow{\rho}_n^-(\overrightarrow{r}') = \overrightarrow{r}' - v^-, \quad \overrightarrow{r}' \; in \; T_n^- \tag{2.37}$$

The edges in the RWG basis function correspond to the three boundary lines of each triangular element. Boundary edges are those that belong to only one triangle, while non-boundary shared edges are those shared between two triangles. In Equation (2.34), N represents the number of non-boundary shared edges. This type of meshing restricts the current from passing through the boundary edges, which violates the continuity condition between the meshes.

With the RWG basis function, it is evident that the vertical current component on an edge must exhibit continuity. This means that the current leaving one triangle must be equal to the current entering the other triangle. Further explanations on RWG basis functions can be found in [65] and [66].

Another advantage of RWG functions over pulse functions is that each unknown corresponds to the coefficient of a vector. Unlike pulse functions, which consider separate x and y coordinates, RWG functions have only one unknown determined for each edge. In general, using RWG functions reduces the number of unknowns in the problem by approximately 30% compared to pulse functions, thereby speeding up the current reconstruction process.

Finally, by substituting the RWG functions for the currents in the EFIE equations and applying divergence and curl operations to the functions, discrete matrix equations can be obtained as follows:

$$\begin{bmatrix} \mathbf{E}_{\mathbf{meas},\theta} \\ \mathbf{E}_{\mathbf{meas},\varphi} \end{bmatrix} = \begin{bmatrix} Z_{\mathbf{E}_{\theta,\mathbf{I}_{\mathbf{J_n}}}} & Z_{\mathbf{E}_{\theta,\mathbf{I}_{\mathbf{M_n}}}} \\ Z_{\mathbf{E}_{\varphi,\mathbf{I}_{\mathbf{J_n}}}} & Z_{\mathbf{E}_{\varphi,\mathbf{I}_{\mathbf{M_n}}}} \end{bmatrix} \begin{bmatrix} \mathbf{I}_{\mathbf{J_n}} \\ \mathbf{I}_{\mathbf{M_n}} \end{bmatrix} \tag{2.38}$$

2.3 Antenna/body coupling

When an antenna is in close proximity to the human body, a portion of the reactive near-field energy surrounding the antenna becomes coupled and absorbed. As the incident wave from the antenna reaches the human body, part of it gets absorbed, while another part reflects off the tissue. This reflected energy can also couple back to the source and be partially retransmitted. This iterative process may lead to multiple antenna-body interactions, resulting in the absorbed power being characterized as a sum of these interactions [67]. These multiple interactions can influence the actual current distribution on the antenna and the absorbed energy profile. Additionally, some of the reflected energy may couple through the antenna port to the generator load, thereby altering the input impedance and antenna matching. These factors play a significant role in the RF energy deposition from sources placed in close proximity to the human body. Consequently, in the near-field region, the coupling between the antenna and the human body primarily impacts the energy transmitted to the tissues.

The literature extensively discusses various aspects of the interactions between antennas and the human body in millimeter waves (mmWs). For example, in [68], several human body exposure scenarios were studied for a terminal with a 60-GHz antenna module. The results demonstrated that both the head and hand, when placed in the near-field region of the antenna, significantly affect the radiation pattern, efficiency, and antenna reflection coefficient. Changes in the antenna's radiation characteristics due to the presence of the human body in the near-field region can consequently affect the total impinging field on the body. In another study conducted at 24 GHz, with some results also at 60 GHz, it was observed that the interaction between the source and body is relatively weak [69]. However, it is important to note that these studies were conducted on electrically small antennas.

In a study presented in [70], the impact of antenna-human body interactions in the near-field on the transmitted power density (TPD) at 60 GHz was investigated. Figure 2.12 illustrates the comparison of sources with increasing complexity, including plane waves with and without free-space losses, antenna-equivalent sources, and patch antenna arrays. The presence of the human body affects the spatial distribution of the TPD due to constructive or destructive interferences, impacting both the peak and averaged TPD. The study revealed that the presence of the human body in the vicinity of a source increases the average TPD.

These studies suggest that, as a result of antenna-body interactions, it is not possible to obtain the precise distribution of transmitted power density (TPD) and the corresponding peak and averaged values solely through free-space measurements of incident power density in the absence of a human body model. Therefore, to achieve accurate measurements of absorbed power density and epithelial power density, which are important dosimetric quantities for frequencies above 6 GHz, it is crucial to conduct measurements with the wireless device under test perturbed in the same manner as it would be by the presence of the human body in practical applications.

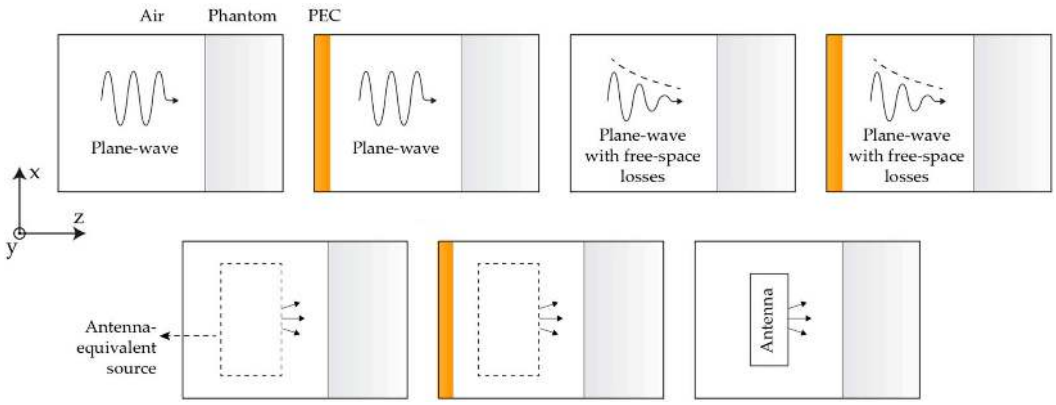

Figure 2.12: Schematic representation of considered exposure scenarios [70].

2.4 Dosimetry measurement systems

Dosimetry measurement systems, classified into invasive and noninvasive systems, specifically designed for assessing electromagnetic field exposure. Invasive systems, requiring probes, include E-field, electro-optical (EO), and optical fiber thermal sensor-based systems. Noninvasive systems, without sample disturbance, comprise infrared (IR), power density, and thermal scanner [71]. A comparative analysis of these systems is presented in Table 2.1.

Single E-field probe systems, involve a robotic arm scanning within a phantom. While standardized, they pose challenges in time consumption, calibration, and resolution limitations [39, 72, 73]. Array E-field probe systems, developed for faster SAR estimations, encounter issues with interactions and potential inaccuracies [74, 75].

EO probe-based systems utilize single or vector array probes, offering advantages like minimal disturbance and measuring amplitude and phase of the E field. However, challenges exist in the required movement inside the phantom and potential inaccuracies at higher frequencies [76, 77].

Optical fiber thermal sensor-based systems employ 3D arrays for SAR evaluation, showing good agreement with E-field probe measurements. Pros include frequency independence, but limitations include spatial resolution and heat diffusion effects [78, 79].

Incident power density measurements quantify radiation from antennas in the far-field quickly, though lacking spatial information and facing potential overestimation issues [49].

Thermal magnetic resonance scanner systems utilize MRI for noninvasive SAR assessment, offering volumetric thermometry with millimeter resolution. Pros include wideband assessment, but limitations involve the inability to measure E-field phase relationships [80, 81].

IR systems, leveraging thermometry, offer non-contact temperature measurements. Pros include speed and efficiency, but limitations involve potential underestimation of maximal exposure and surface measurements [82].

Identifying the system parameters that contribute to the overall uncertainty of the measurement system is crucial for ensuring accurate and reliable measurements. Two key factors influencing uncertainty include precise dielectric property measurements and E-field probe calibration. The dielectric properties of the materials involved play a significant

Table 2.1: Comparison of the measurement system features from [71]

Meas. System	Frequency	Meas. Sensivity	Multiple Simultaneous Freq.	Speed of Acquisition
E-field probe	DC–6 GHz	0.15 mV/m	No	Slow
E-field probe scanning	0.5–6 GHz	Unknown	No	Fast
EO probe	0.7–15 GHz	0.002 W/kg	Yes	Slow
EO probe vector array	0.7–15 GHz	Unknown	No	Fast
Optical fiber thermal sensor	DC–6 GHz	<0.1°C	Yes	Fast
Incident power density	6–>100 GHz	Unknown	No	Fast
MRI thermal scanning	DC–>100 GHz	<0.1°C	Yes	Fast
IR imaging	DC–>100 GHz	0.05°C	Yes	Fast

role in measurement in liquid-filled phantom, and any uncertainties in these properties can lead to inaccuracies in measurements. Additionally, the calibration of E-field probes is a critical step, as inaccuracies in probe calibration directly impact the reliability of the measurements. For a detailed exploration of the technique involving probe calibration, as well as insights into the uncertainties associated with practical measurements and the challenges encountered at mm-wave frequencies, please refer to [83–85]

Millimeter-wave devices demand updates in exposure compliance testing technologies. Challenges include shallow penetration and diverse directional antennas. Potential solutions include advancements in sensing technologies, thermal mapping with MRI, EO probe systems, and ongoing research in test-time reduction.

Considering the advancements, there has been notable progress in measuring the E-field at millimeter-wave frequencies. For instance, the Schmid & Partner Engineering AG (SPEAG) team has developed a compact mm-Wave probe employing two dipoles for pseudo-vector information. Operating from 750 MHz to 110 GHz, with a dynamic range of <20 V/m to 10,000 V/m, this system minimizes field perturbation and is tailored for E-field measurements in close proximity (<2 mm) to 5G devices and mm-wave transmitters above 6 GHz [72]. Additionally, KAPTEOS has introduced EO probes spanning 10 Hz to 100 GHz, featuring interference-free optical RX antennas. These probes ensure compliance in challenging conditions and offer a broad measurement range from below 25 mV_{peak}/m to 1.4 MV_{peak}/m, covering the RF spectrum up to 60 GHz for high-speed probes [76].

2.5 Summary

As explained in this chapter, the first issue to consider is the distance from the antenna, which is typically within the reactive near-field region. In this region, the antenna field does not have a specific profile, making it challenging to establish an analytical and precise relationship between the electric field and the magnetic field. The phase of the fields, which is crucial for determining power density in the reactive near-field, is dependent on the spatial coordinates, further complicating field analysis. Another important aspect is the proximity of the human body to the antenna, leading to interactions between them. These interactions, including coupling and multiple reflections, significantly impact the field both on the surface and inside the human tissue. Despite the importance and influence of these factors on power density estimation, no articles have fully addressed the scenario of an antenna in close proximity to a human model at high frequencies. Most of the published articles focus on determining incident power density or transmitted power density without considering coupling effects, and all measurements have been conducted on the antenna in free-space.

Measurement systems for millimeter-wave device compliance testing exhibit diverse technologies, each with its pros and cons. Challenges persist, emphasizing the need for ongoing research and advancements in testing methodologies to meet the evolving landscape of millimeter-wave devices.

Regarding field reconstruction methods, previous studies such as [49] and [69] have demonstrated that the incident power density can be obtained by using back-transform and forward-transform methods, respectively, assuming the antenna is in free-space. In [86], the transmitted power density is determined using the transmission coefficient method, assuming the far-field condition. Generally, algorithms for transforming mea-

sured fields into power density at the evaluation surface employ one or more of the following techniques:

- Methodologies to extract field information from measured data (e.g., retrieving phase from amplitude)
- Techniques to resolve the H-field from the E-field (or vice versa)
- Backward/Forward transformation of the fields when the evaluation surface is closer to the DUT than the closest measurement region (or vice versa)
- Transmission transformation of the fields into the human skin

In [45], the distance (d) from the antenna marking the transition from the reactive near-field, where the energy-storing E-fields are predominant, to the radiative near-field zone is evaluated as 0.14λ, which is close to $\lambda/2\pi \approx 0.16\lambda$ established in [87]. Additionally, [69] confirmed that the contribution from the reactive near-field is not expected to be dominant for distances greater than $\lambda/2\pi = 2$ mm at 24 GHz.

Based on the current state of the art, the coupling and multiple reflections between the antenna and the human skin tissue have been largely neglected in analyses. This study focuses on this significant aspect and its contribution to power density. In Table 2.2, a comparison of the articles published so far on human exposure is briefly presented, highlighting the limitations and challenges of each study. Articles specifically related to absorbed power density are marked with a pink background.

Therefore, there are three possible approaches to evaluate APD: 1) measuring the E-field inside the phantom [88–90], 2) measuring the E-field in the interval between the DUT and the phantom, where establishing the relation between the measured E-field and the transmitted E-field into the phantom is complex, and as explained in Section I, measurements in this area, particularly at close DUT-phantom separation distances, are challenging due to coupling effects, and 3) measurement in free space outside the DUT-phantom interval and the phantom itself, which is a non-invasive approach addressed in this article.

Table 2.2: Comparison of papers around human exposure

	Paper	Year	Freq. (GHz)	Parameter	Method	Layers	Meas.	Com. Soft.	Description	Limitation
1	[58]	2000	0.9, 1.71	SAR	DGF (SWE) + MAS	1, 3	×	×	The dipole antenna is positioned near a dielectric sphere, and the SWE method is used to analyze the field in different regions. Boundary conditions are applied to obtain the unknown coefficients, considering the dipole as a collective of small currents.	This analysis is limited to the spherical model of the human body, with an assumed distance of 10 cm between the antenna and the human body model.
2	[56]	2002	0.89	Max E-field	SWE	-	✓	✓	The SWE equations are formulated separately for each array of the antenna. The overall SWE of the antenna is obtained by transferring the coordinates to the center of the antenna and summing up the SWE of each array. Unknown coefficients are determined by measuring the field on a sphere surrounding the entire antenna.	This analysis does not consider the coupling between the antenna and the human body.

3	[59]	2012	0.9, 1.8	SAR	NFM (SWE) + MoM	2	×	✓	The antenna is discretized using RWG basis functions, allowing the determination of surface currents by applying a voltage source on the meshes. Simultaneously, the SWE for the two-layer model of the human head is formulated, enabling the calculation of induced currents at the layer boundaries through the application of boundary conditions. To account for the coupling effect, an iterative method is employed, considering the reciprocal influence between the source current and the currents induced by the phantom.	This approach is specific to the spherical human body model, and the minimum distance between the antenna and the human body is assumed to be 15 mm.
4	[68]	2017	60	Local SAR, Total AP, IPD_{eq}	CST, HFSS	1	✓	✓	The article focuses on studying the exposure of the head and hand to a mm-wave antenna. It investigates the effects of the proximity of the human body on the radiation parameters of the antenna.	It does not propose a method for assessing the absorbed power density (APD), but rather aims to understand the impact of the human body's proximity on the antenna's radiation characteristics.

5	[55]	2017	2.4	SAR	SWE + FDTD	multi-layer	✓	✓	The unknown coefficients of the antenna field's SWE are determined by measuring on a surrounding sphere. These fields are then utilized as incident plane waves for calculating the SAR using the FDTD method.	It relies on the far-field assumption or plane-wave assumption.
6	[45]	2018	10, 30	IPD	Analytical + FEKO	-	×	✓	The analytical formula of the dipole array ((10-74) and (10-75) in [91]) is used.	It assumes the far-field assumption and does not consider the coupling between the arrays.
7	[92]	2018	1-300	SAR, TPD	FDTD	7	×	✓	The article investigates parameters such as the averaging area of the power density, the transition frequency at which the metric is changed from SAR to PD, and the exposure averaging time. Its purpose is to modify the existing standards by examining radiation parameters.	It does investigate the parameters to modify the existing standards
8	[69]	2018	24-60	APD	PWS + FEKO	1	×	✓	The article describes obtaining the field in a hypothetical plane in free space using FEKO. It then determines the APD by performing a spatial Fourier transformation of the field and applying the plane wave expansion transmission coefficient in the wavenumber domain.	It does not consider the coupling between the antenna and the human body. Additionally, it assumes a minimum distance of $d < 10$ mm.

9	[93]	2018	2.5	SAR	EQC (MoM)	1	✓	✓	The article proposes a non-invasive method for evaluating SAR. It starts by formulating electric and magnetic integral equations in the PMCHWT formula. The moment impedance matrix is then determined through meshing and discretization using RWG basic functions on the antenna and phantom. The moment voltage matrix is obtained by measuring the field on the sphere surrounding the antenna and phantom. Finally, the inverse matrix equation is solved using the moment method to calculate the currents on the phantom.	It cannot be applied in the shadow area and is not applicable for 5G due to high attenuation in mm-wave frequencies.
10	[49]	2019	15-100	IPD	PWS + FEKO	-	✓	✓	The article focuses on measuring the field at a distant location and transferring it near the antenna using the PWS method.	The dimensions of the measurement plane relative to the distance from the antenna can be large and pose challenges.

11	[57]	2019	0.403	IPD	SWE	1	×	✓	The article describes the setup where an antenna is placed inside an air-filled sphere, which is further enclosed within a dielectric sphere. The SWE is formulated and boundary conditions are applied for both the phantom located at the origin and the implant area by considering coordinate transformations. By solving these equations, the unknown coefficients are determined.	This approach is applicable only to the spherical model of the human body.
12	[70]	2020	60	TPD	PWS + CST	1	×	✓	The article proposes a method that combines the PWS and the transmission coefficient in the wavenumber domain to evaluate the electromagnetic field. It also considers the impact of successive reflections between the antenna and the phantom by introducing a PEC plate as a reflector.	The method does not account for the coupling effect between the antenna and the human body and its impact on the antenna's current alteration, which may limit its accuracy in certain scenarios.

13	[94]	2020	38	IPD	EQC (MoM) + CST	-	✓	✓	The article focuses on reconstructing the equivalent currents on the antenna's surface by measuring the radiation field on a spherical surface surrounding the antenna.	The minimum distance considered in the study is limited to $d = 3$ mm, which may affect the applicability of the findings in scenarios with larger distances.
14	[95]	2020	10-90	IPD	EQC (MoM) + FDTD	-	✓	✓	In the article, the field near the antenna is measured at a distance of 2 mm using the EUmmWVx probe. The measured fields are then used to reconstruct the equivalent currents on the antenna. The field and the IPD are also determined at further distances.	The method is limited by considering a minimum distance of 2 mm.
15	[86]	2020	6-300	TPD	Analytical	6	×	×	The article focuses on assessing the transmitted power density to the tissue of the human body. This is done by considering the reflection and transmission coefficients and using a layered model of the human body for TE and TM plane waves with incident angles ranging from 0 to 90 degrees.	The analysis relies on the far-field assumption, which may limit its applicability in scenarios where near-field effects are significant or when dealing with close-proximity interactions between the antenna and the human body.

16	[44]	2020	28	IPD, TA	FDTD	1	×	✓	The article investigates the relationship between skin temperature increase and IPD for various incident angles. It explores how different incident angles affect the skin temperature rise	The article does not consider the coupling effect between the antenna and the human body, and it is limited to distances less than 15 mm.
17	[96]	2020	3-30	APD	Analytical + Modified Image Theory (MIT)	1	×	×	The article presents APD assessment using analytical equations, transmission and reflection coefficients, and modified image theory for the infinitesimal antenna (Hertz dipole) above a lossy half-plane (human body)	The method does not consider antenna-body coupling, limiting its applicability.
18	[54]	2021	28	IPD, TPD	SWE + FDTD	multi-layer	×	×	Finding the SWE for the antenna in free space, and then converting these waves to the plane wave as an incident wave to the flat model of the human body.	The method ignores the coupling effect between the antenna and the human body, limiting its accuracy.
19	[97]	2021	28	IPD	EQC (MoM)	-	✓	✓	The article describes finding the SWE for the antenna in free space and converting these waves to the plane wave as an incident wave to the flat model of the human body.	The minimum distance of 5 mm

20	[98]	2021	2.5	non-invasive SAR	EQC (MoM) + FDTD	1	✓	✓	In the article, a dipole is placed in a dielectric sphere, and the SAR is assessed by measuring the field on a spherical surface and reconstructing the equivalent currents on the phantom and dipole's surface.	This method is not applicable for 5G due to high losses in these frequencies.
21	[82]	2021	60	APD Distribution	Infrared (IR) camera + CST	1	✓	✓	In the article, a high-power millimeter wave generator signal is used to stimulate the antenna under the phantom. The thermal pattern on the phantom is then obtained from above using a high-resolution infrared camera.	It requires expensive equipment and can only provide temperature observations for finding the APD distribution.
22	[99]	2021	2, 28	SAR, APD, TA	FDTD	multi-layer	×	✓	The article examines the simultaneous effect of human exposure to mobile phones operating at 2 and 28 GHz. It investigates the superposition of SAR and APD on temperature increase.	The study has a limitation in that it considers a minimum distance of 5 mm.
23	[100]	2021	<6	SAR, APD, TA	FDTD	multi-layer	×	✓	The article is a review paper that examines studies on human exposure and body modeling in relation to the revision of guidelines and standards. It provides a comprehensive overview of the existing research in this field.	It does not present any new experimental data or findings of its own.

24	[101]	2021	10-90	IPD	SWE + PWE + FDTD	-	×	✓	The article describes a method to assess the IPD of an antenna by obtaining the SWE at a minimum distance surrounding the antenna. The SWE is then converted to the PWS in the spectral domain and transferred closer to the antenna for IPD assessment.	The method is limited to a minimum distance of 2 mm.
25	[102]	2021	28	IPD	EQC (MoM)+ PWE	-	✓	✓	The article presents a method for obtaining the IPD by reconstructing equivalent currents and transferring the PWE in the spectral domain near the antenna.	The measurement plane should be sufficiently large to ensure accurate results.
26	[88]	2021	<10	APD	SAR measurment + FDTD	1	✓	✓	The article proposes using low-frequency equipment to assess the APD based on measured data and an algorithm for conventional peak spatial-average SAR estimation.	The method has been extended for frequencies below 10 GHz.
27	[103]	2021	10-90	IPD + TA	FDTD + FIT + GB-IBEM	-, multi-layer	×	✓	Review paper comparing IPD errors from FDTD, FIT, and GB-IBEM methods developed by six groups using different antennas and commercial software.	Limited to comparing existing methods and their errors.

28	[104]	2021	2.1, 2.6	IPD	Stochastic geometry frame-work	-	×	✓	Field measurement in Brussels obtains downlink exposure from base station antennas using a statistical random model.	The study is limited to frequencies below 3 GHz and does not encompass higher frequency ranges.
29	[105]	2021	60	APD	PWS + CST	1	×	✓	This article examines the influence of antenna-human body coupling on increasing APD relative to IPD.	The study specifically considers the effect of antenna-human body coupling by placing the PEC plane behind the antenna, without exploring additional coupling scenarios or factors.
30	[106]	2021	0.1-300	SAR, IPD, TPD	-	-	×	×	This article investigates recent standards and studies on human exposure evaluation, highlighting the distinction between radiation standards and the assessment of human-used products and medical applications.	Review paper
31	[107]	2021	26, 60	APD	CST	1	×	✓	This article examines the effect of clothes and people's age on human exposure.	The study considers a minimum distance of 5 mm.

32	[108]	2022	3-30	IPD	EQC (MoM) + FDTD	-	✓	✓	This article focuses on reconstructing source equivalent currents by measuring near the antenna and determining far-field IPD.	The study assumes a minimum distance of 2 mm.
33	[90]	2022	10-30	APD	S_{ab} probe + FDTD	5	✓	✓	This article aims to find APD by developing a power density measurement probe and integrating it with the SAR scanner system, conducting measurements inside the human body liquid-filled phantom	The study focuses solely on APD measurement using the developed probe and does not consider the amount of radiation power for field penetration into the tissue.
34	[109]	2023	10-90	APD	FDTD + FIT + FEM + TLM + GB-IBEM	multi-layer	×	✓	This review paper compares the errors of APD evaluated by methods developed by nine groups, including group-specific FDTD, FIT, FEM, GB-IBEM, and TLM using commercial software.	The study provides a summary of the methods developed by the groups but does not offer a detailed analysis or propose new evaluation techniques.

Chapter 3

APD assessment by back-transformation from inside skin tissue

Measuring electric and magnetic fields near the antenna presents challenges and complexities due to various factors: 1) the very short distance between the antenna and the tissue, 2) the measurement of probe thickness and its impact on field distribution, and 3) the presence of coupling and multiple reflections between the antenna and the human body. These factors make accurate measurement almost impossible. Additionally, the field phase reconstruction method encounters errors due to the lack of a clear and regular field distribution.

To address these challenges, we propose a method that considers the field inside the skin and utilizes back-propagation to achieve PD on the skin's surface. This approach offers the advantage of accounting for the fields inside the tissue, as many interactions between the antenna and human tissue do not penetrate the tissue but still contribute to the overall effect. By considering the field inside the tissue to evaluate the field just below the surface, we can obtain APD with maximum accuracy.

This technique simplifies the measurement process of PD with reliable accuracy, reproducibility, and reasonable measurement time. The goal of this study is to enhance the applicability and understand the limitations of conventional techniques for assessing compliance with wireless technologies operating in the quasi-millimeterwave (quasi-MMW) and MMW bands. These technologies are used in wireless communication devices that operate above 6 GHz and are expected to become widespread in the near future, particularly in close proximity to the human head/body.

3.1 Antenna configuration

According to the desired frequency ranges in 5G communications, frequencies above 6 GHz are selected to represent the power characteristics fully [110]. For beamforming and MIMO capabilities, a 2x2 microstrip patch array is used, with all metal parts modeled as PEC. The antenna's geometries and dimensions relative to the wavelength (λ) are illustrated in Figure 3.1, where λ represents the wavelength in free space. The red dot indicates the antenna's feeding port. In the worst-case scenario, the human body is

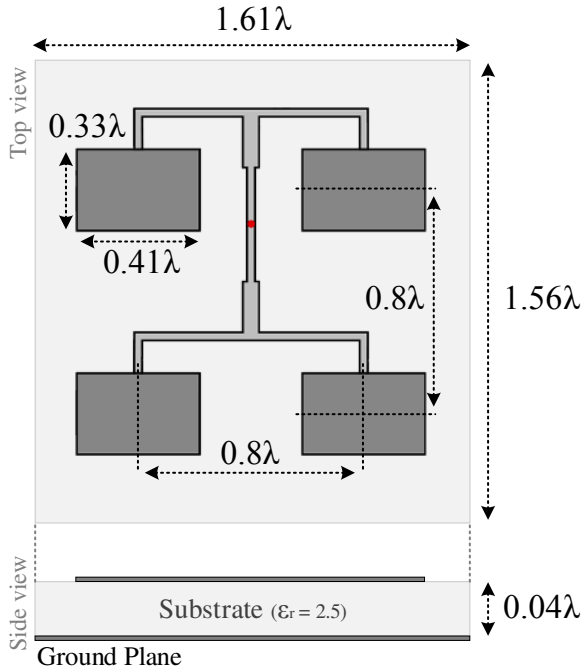

Figure 3.1: 2×2 patch array antenna geometry.

exposed to the main beam of the antenna. The antenna radiation power is set to 200 mW (23 dBm), which corresponds to the maximum power output of both 5G and previous communication generations [111].

To evaluate human body exposure, the conditions specified in IEEE and ICNIRP standards are considered, focusing on the worst-case scenario involving the maximum radiation absorbed by the human body [6, 7]. If a radiating device does not pose harm to humans under worst-case radiation conditions, it is considered safe under other conditions as well. Simulations are performed with the main beam of the antenna perpendicular to the dielectric half-space to represent this worst-case scenario. This configuration is also chosen to maximize the coupling between the antenna and the human tissue model.

3.2 Human skin modeling

The exposed body is modeled as a homogenous half-space with dielectric properties equal to the average between wet and dry skin The complex dielectric permittivity of the skin as a function of frequency is estimated using the ColeCole dispersion model. The parameters for the ColeCole model are extracted through experimentally by Gabriel et al. [112].

$$\varepsilon(\omega) = \varepsilon_\infty \sum_{n=1}^{N} \frac{\Delta\varepsilon_n}{1 + (j\omega\tau_n)(1-\alpha_n)} + \frac{\sigma_i}{j\omega\varepsilon_0} \tag{3.1}$$

Due to the shallow field penetration in the millimeter-wave frequency range (see Table 1.2), the homogenous skin model is considered for this study. The dielectric properties for the frequencies investigated in this study are summarized in Table 3.1.

The simulations are conducted with the antenna oriented to make its main beam point

Table 3.1: Dielectric properties of the skin ($\varepsilon = (\varepsilon_{wet} + \varepsilon_{dry})/2$)

f (GHz)	10	15	24	30	45	60	100
ε	32.41	27.27	19.99	16.6	11.61	9.1	6.42
σ (S/m)	8.48	14.24	23.02	27.3	34.16	37.96	42.78

perpendicularly to the tissue half-space. This configuration is selected since it is expected to maximize the antenna-tissue coupling.

3.3 Backward PWS method

The method structure is illustrated in Figure 3.2. To obtain the electric field (E-field) distribution of the antenna for the near-field exposure analysis, the following steps are followed. Firstly, the field distributions of E_x and E_y are measured using FEKO [113] within the skin tissue when the antenna is in close proximity to the skin at a separation distance of $dDUT$ from the human skin surface. The sampling plane is defined as the XY-plane over an area of $40\lambda \times 40\lambda$ with a resolution of $\lambda/10$ inside the skin tissue at a separation distance of $dRec$ from the human skin surface. Subsequently, the PWS (Plane Wave Spectrum) back transformation is utilized to evaluate E_x and E_y on the surface inside the human skin. From there, the magnetic field (H-field) components H_x and H_y are derived from E_x and E_y (refer to Section 2.2.1.1). Finally, the absorbed power density averaged over a square area of A [cm^2], denoted as S_A [W/m^2], is calculated using the H- and E-fields (Eq. 1.14). In accordance with recently published guidelines [6, 7], the maximum value of S_A is assessed with an averaging area (A) of 1 cm^2 and 4 cm^2.

The absorbed power density (APD) averaged over a square area of A [cm^2], denoted as S_A [W/m^2]:

$$S_A(d_{DUT}) = \frac{1}{2A} \iint_A \mathrm{Re}[\mathbf{E}(\overrightarrow{r}) \times \mathbf{H}^*(\overrightarrow{r})] \cdot \overrightarrow{n}\, dxdy \tag{3.2}$$

For validation purposes, a comparison is made between the proposed method and the results obtained through computational simulations. The simulations are conducted using the commercial electromagnetic solver FEKO, which is based on the Method of Moments.

In this scenario, the proposed technique utilizes the PWS back-transformation inside the human skin to fully consider the interaction of the incident field with the tissue. However, it is important to note that a portion of the reflected energy may be scattered by the antenna, leading to multiple scattering and reception-emission phenomena. These interactions can modify the field and have an impact on the tissue surface. As a result, transmitted and reflected waves may generate a partial standing wave. To assess this effect, a comparison is made between the electric field beneath the skin surface, evaluated using the proposed technique, and the results obtained through the PWS forward-transformation, employing the spectral transmission coefficient as detailed in Section 2.2.1.1.

The obtained results encompass different frequencies and various separation distances for d_{DUT} (ranging from 1 mm to 300 mm) and d_{Rec} (ranging from 1 mm to 10 mm). It is important to acknowledge that the detectability of the field inside the tissue can pose a

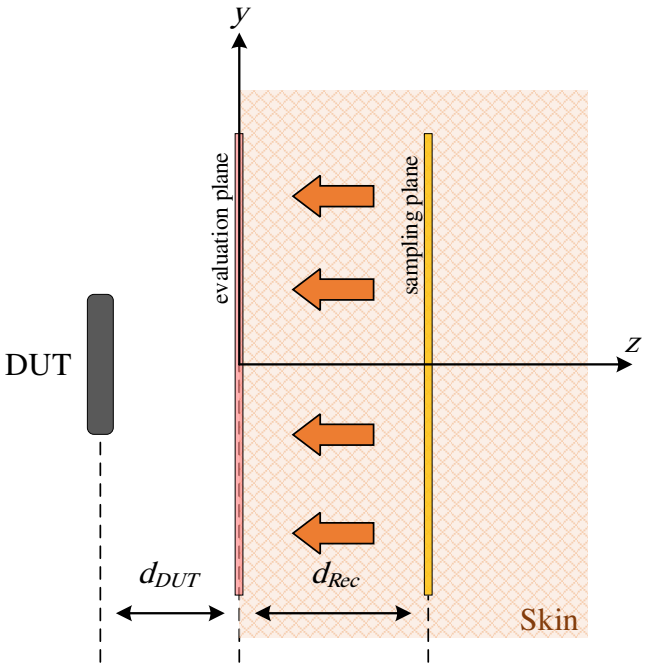

(a) backward-transformation PWS (proposed method)

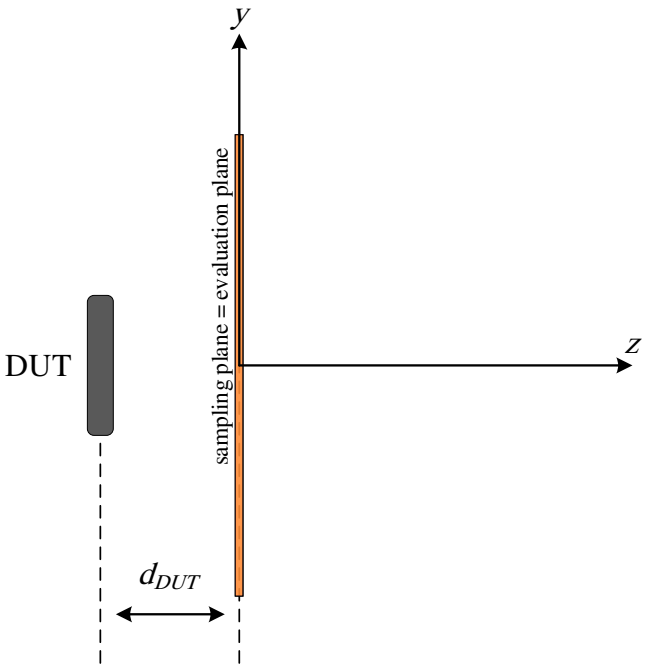

(b) forward-transformation PWS

Figure 3.2: PWS method structure for assessing absorbed power density

challenge and limitation due to the low penetration depth at millimeter frequencies. To address this, the E-field amplitude on the sampling plane (inside the skin) is examined from detectable viewpoints, ensuring the method's applicability.

3.4 Results and discussion

Accuracy and precision are crucial factors when analyzing near-field exposure, and the absorbed power density serves as a well-established metric due to its consideration of antenna-body interaction. In this chapter, the focus is on examining the distribution of the absorbed power density, determining the maximum values of S_{4cm^2} and S_{1cm^2}, assessing the level of error, evaluating the practicality of the proposed technique by considering the detectable amplitude of the electric field on the measuring plane, exploring the concept of penetration depth through the consideration of coupling and multiple reflections, and determining the required plane size for accurate power density measurement. These factors collectively contribute to a comprehensive analysis of the absorbed power density and provide insights into its distribution, error characteristics, and the practical aspects of the proposed technique.

Results in the figures below are divided into 3 scenarios as follows:

- **Free space:** using PWS forward-transformation technique to evaluate APD on the human skin surface for the antenna in free space
- **Reference:** using FEKO to evaluate APD on the human skin surface
- **Inside skin (d_{Rec}):** using PWS back-transformation from measurement inside the tissue to assess APD on the human skin surface

"d_{Rec}" may be used instead of "Inside skin (d_{Rec})", for simplicity.

3.4.1 APD distribution

The distribution of power density is crucial in understanding the direction and concentration of power on the surface of the human skin. Figures 3.3, 3.4, and 3.5 illustrate the APD (S_A) distributions of the 2×2 array antenna operating at 10 GHz, 24 GHz, and 60 GHz, respectively. These figures provide valuable insights into the spatial distribution of power density at different frequencies, aiding in the assessment of potential exposure levels on the human skin's surface. The obtained APD distributions are normalized to the peak value obtained by the reference measurement at each separation distance.

To examine the similarity more closely among values obtained from different scenarios, the correlation coefficient is employed. This coefficient is calculated using the equation (3.3), representing the two-dimensional correlation coefficient between matrices A and B.

$$correlation\ coefficient = \frac{\sum_m \sum_n (A_{mn} - \bar{A})(B_{mn} - \bar{B})}{\sqrt{(\sum_m \sum_n (A_{mn} - \bar{A})^2)(\sum_m \sum_n (B_{mn} - \bar{B})^2)}} \tag{3.3}$$

where $\bar{A}$ and $\bar{B}$ denote the averages of all matrix elements in matrices A and B, respectively.

In the case of the d_{Rec} scenario, the APD distributions closely follow the reference at all d_{DUT} distances, although the correlation decreases as d_{Rec} increases. The minimum correlation coefficient between the APD distributions of the d_{Rec} scenario and the reference is 0.7063, observed at 10 GHz for $d_{Rec} = 30$ mm and $d_{DUT} = 1$ mm. On the other hand, the maximum correlation coefficient between the APD distributions of the free space scenario and the reference is 0.9489, achieved at 60 GHz for $d_{DUT} = 150$ mm.

Qualitatively, the pattern of S_A obtained by the d_{Rec} scenario agrees with the reference, while a different pattern is observed between the reference and the free space scenario. This difference arises because the PWS in free space neglects the effects of coupling and multiple reflections, which are dominant at close antenna-body distances. It should be noted that at 10 GHz, the antenna is much closer to the skin model in terms of λ compared to 60 GHz. Although it maintains the same d_{DUT} distance, the antenna size is six times larger, resulting in a more powerful near-field situation at 10 GHz. As the distance from the antenna increases and the coupling/multiple reflections become negligible, it can be expected that the PWS in free space would closely resemble the reference distribution, albeit with some errors.

3.4.2 Maximum S_A

Figures 3.6, 3.8 and 3.10 show the maximum values of S_{4cm^2} and figure 3.12 shows the maximum values of S_{1cm^2} for 1 mm $\leq d_{DUT} \leq$ 300 mm, 1 mm $\leq d_{DUT} \leq$ 125 mm,and 1 mm $\leq d_{DUT} \leq$ 150 mm at 10, 24, and 60 GHz, respectively. Note that A is set considering the values in the ICNIRP guidelines [6], which can be chosen as 4 cm^2 or 1 cm^2 at 30-300 GHz under a condition. The vertical and horizontal axes of the figures are the maximum S_A and the separation distance from the antenna (d_{DUT}), respectively. The orange and black lines in the figures denote S_A derived by the free space and the refrence, respectively, and the rest of the lines derived by d_{DUT} scenarios.

According to the figures, the antenna-body interaction results in resonance at around 0.4λ and 0.8λ, which forms the most and the minor error with the free space scenario. These variations are caused by the constructive and destructive incident and reflected waves. The results show that both maximum S_{4cm^2} and S_{1cm^2} obtained by d_{Rec} scenarios, unlike free space scenario, are in good agreement with that obtained from the reference. For $d_{DUT} \geq \lambda$, the maximum S_A obtained by the free-space scenario follows the reference with an almost constant error in all frequencies. In conclusion, the coupling/multireflection between the DUT and the skin tissue is negligible when $d_{DUT} \geq \lambda$.

The important issue that attracted attention is the location of averaging area (A). Figure 3.7, 3.9, and 3.11 show the location and the distribution of S_{4cm^2} and figure 3.13 shows the location and the distribution of S_{1cm^2} at separation distances from the antenna (d_{DUT}) at 10, 24 and 60 GHz, respectively. Each row is dedicated to specific separation distances from the antenna (d_{DUT}) and each column is dedicated to a different scenario from Free space, Reference, and Inside skin at separation distances from the skin surface (d_{Rec}). APD distribution graphs may have asymmetric axes concerning the origin due to the location of the maximum S_A in the evaluation plane.

The results demonstrate the location and distribution of the S_{4cm^2} and S_{1cm^2} which obtained by the free space scenarios is very different from the reference. It can be deduced that at a greater distance from the antenna outside the reactive near-field region,

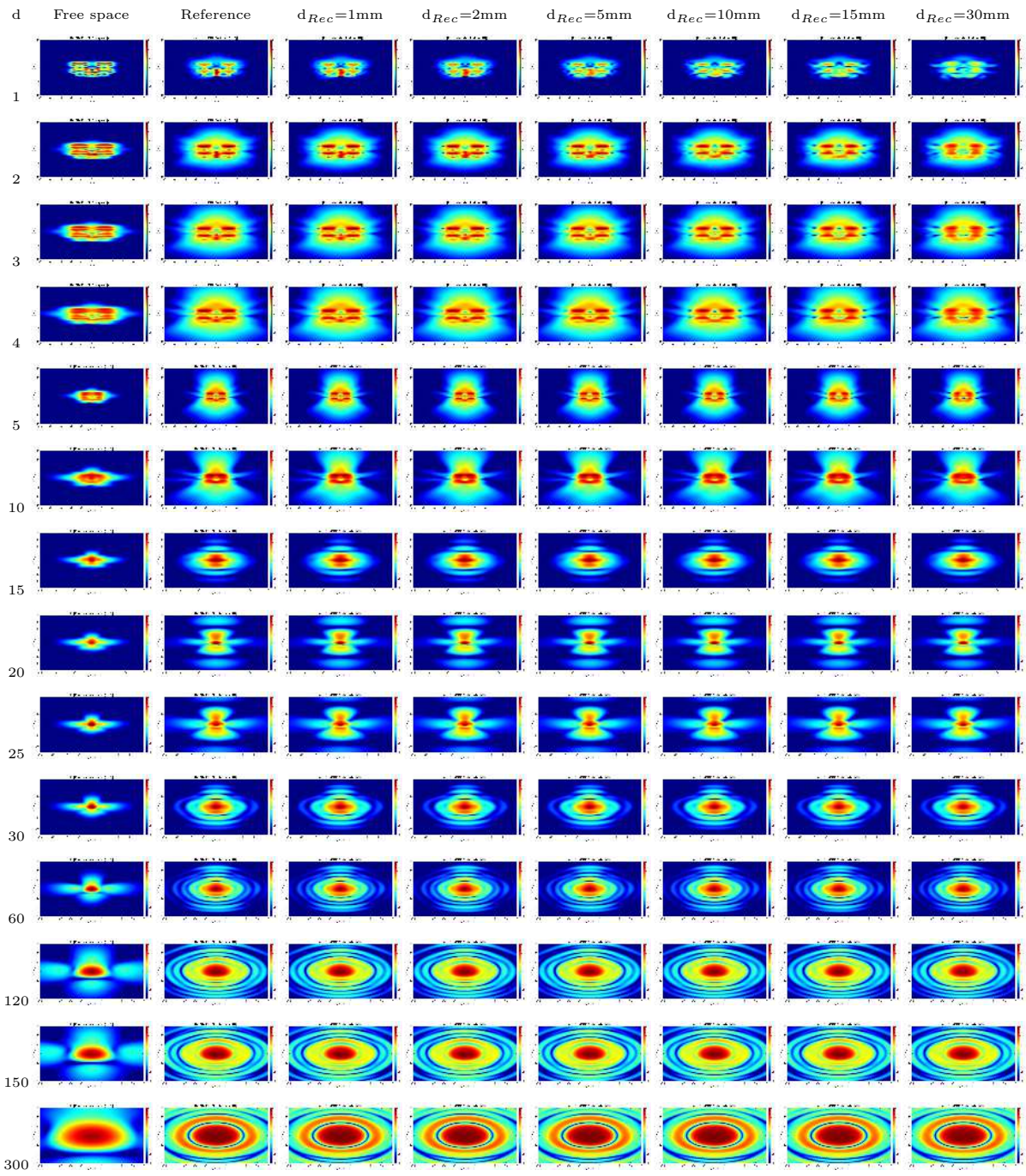

Figure 3.3: APD distribution [dB] at skin surface (f = 10 GHz) [d = d$_{DUT}$ (mm)]

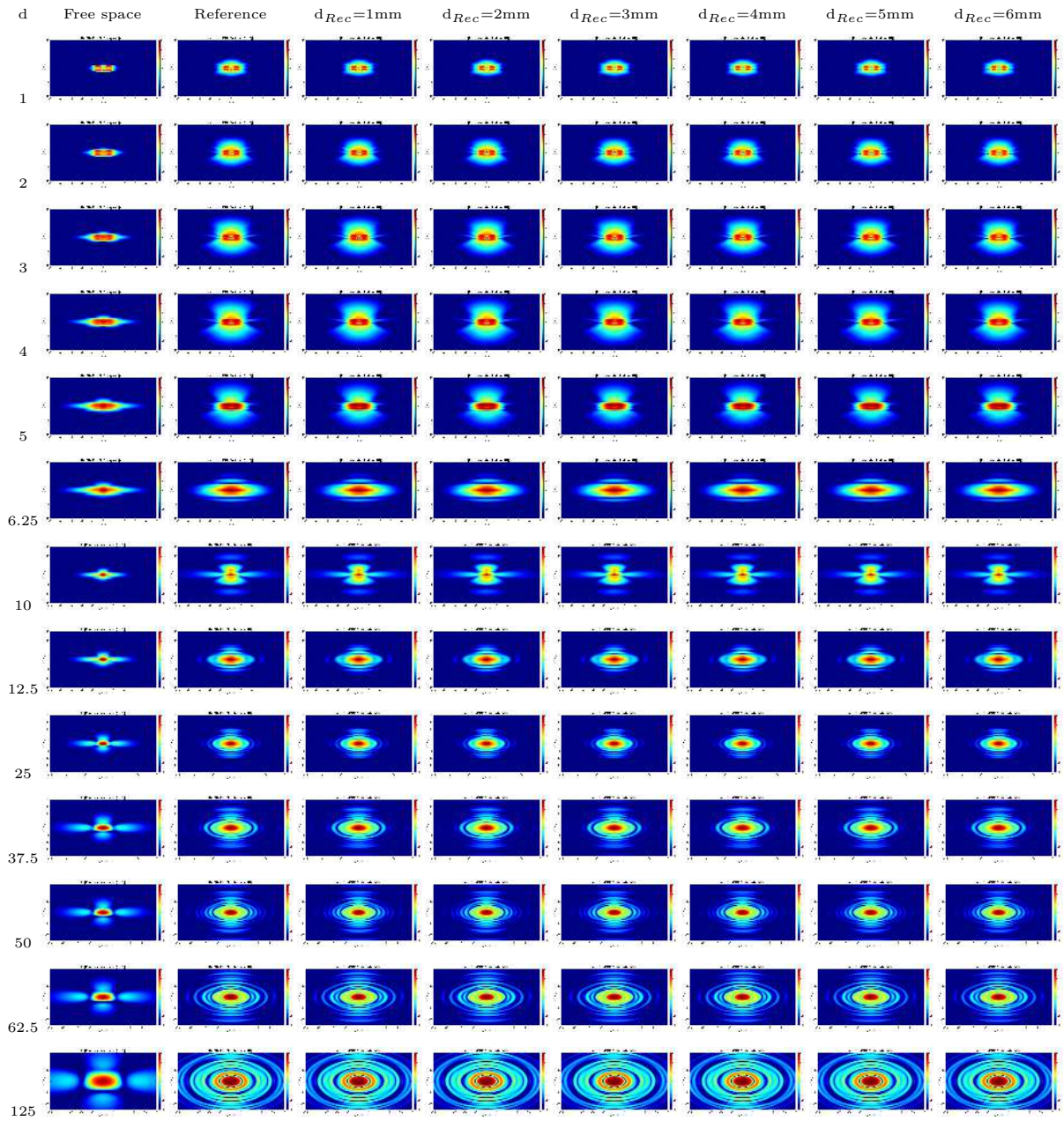

Figure 3.4: APD distribution [dB] at skin surface (f = 24 GHz) [d = d$_{DUT}$ (mm)]

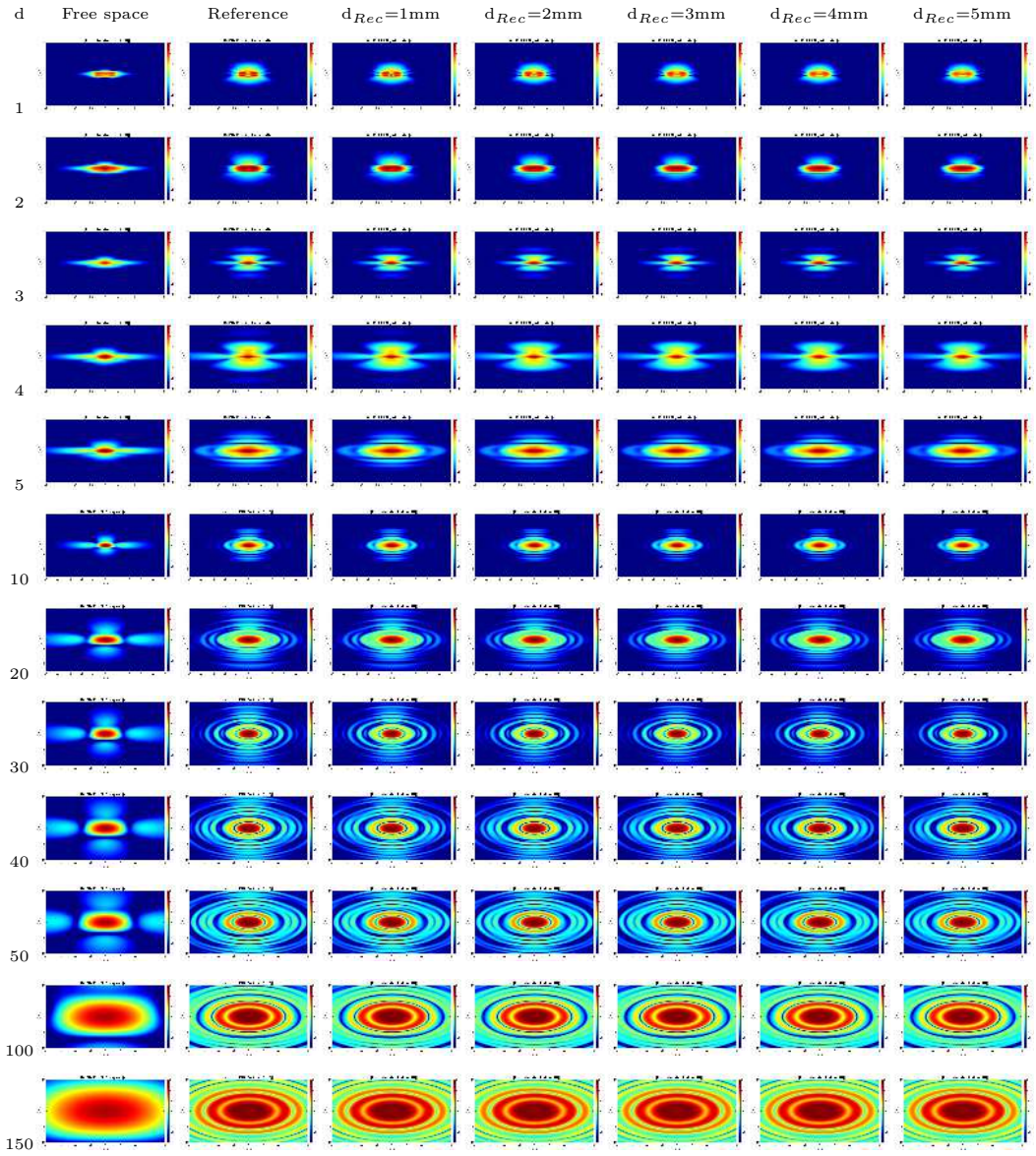

Figure 3.5: APD distribution [dB] at skin surface (f = 60 GHz) [d = d$_{DUT}$ (mm)]

where coupling/multiple reflections can be ignored, the free-space scenario can follow the reference distribution, including some errors.

3.4.2.1 Error of maximum S_A

The values of S_A obtained by the PWS include the numerical error. The reconstruction error is estimated using the following equation:

$$err^{\%}_{Rec} = \left[\frac{|\max\{S_A^{Ref}\} - \max\{S_A^{Rec}\}|}{\max\{S_A^{Ref}\}}\right] \times 100, \tag{3.4}$$

where $\max\{S_A^{Rec}\}$ and $\max\{S_A^{Ref}\}$ are the maximum S_A obtained by backward PWS (inside skin) and the reference value obtained by computational simulation, respectively.

Figures 3.14, 3.15, and 3.16 illustrate the error in the maximum S_A for different d_{DUT} at 10, 24, and 60 GHz, respectively. The vertical axis represents the maximum S_A, while the horizontal axis represents the separation distance from the antenna (d_{DUT}). The light blue bars in the figures represent the error of the maximum S_A obtained using the PWS technique in free space, while the other bars correspond to the backward PWS method.

These figures reveal that the error in the free space PWS method varies for different d_{DUT}, making the method unreliable. The variation in the error between the free space scenario and the reference can be attributed to the lack of consideration for the coupling effect. A more accurate response is expected when the sampling is closer to the surface of the phantom since it enables the detection of evanescent waves carrying field information due to the coupling effect. Conversely, as d_{Rec} increases, the reconstruction accuracy decreases.

Based on Figure 3.14, for the d_{Rec} scenarios of 1, 2, 5, 10, and 15 mm, the error is less than 10% at $d_{DUT} \geq 2$ mm, $d_{DUT} \geq 2$ mm, $d_{DUT} \geq 3$ mm, $d_{DUT} > 5$ mm, and $d_{DUT} > 10$ mm, respectively. Similarly, Figure 3.15 shows that for the d_{Rec} scenarios of 1, 2, 3, 4, and 5 mm, the error is less than 10% at $d_{DUT} \geq 1$ mm, $d_{DUT} \geq 2$ mm, $d_{DUT} > 2$ mm, $d_{DUT} > 3$ mm, and $d_{DUT} \geq 4$ mm, respectively. In Figure 3.16, the error is less than 10% at $d_{DUT} > 1$ mm, $d_{DUT} \geq 2$ mm, $d_{DUT} > 4$ mm, $d_{DUT} > 4$ mm, and $d_{DUT} > 4$ mm for the d_{Rec} scenarios of 1, 2, 3, 4, and 5 mm, respectively.

According to international standards, the agreement between the results obtained using the backward PWS method and the reference within a 10% margin is considered acceptable for compliance assessment during system check and validation procedures [114]. Therefore, since the agreement between the values obtained by the backward PWS method and the computational simulation falls within this satisfactory range, it indicates that the proposed method meets the standards' requirements.

In conclusion, for all frequencies, the $d_{Rec} = 2$ mm scenario yields errors of less than 10% at $d_{DUT} \geq 2$. In this thesis, the $d_{Rec} = 2$ mm scenario is considered acceptable for practical measurements [75]. It is important to note that all results are obtained under the assumption that the distance does not affect the measurement probe.

3.4.2.2 Maximum S_A position error

By analyzing the center of a square area A at the maximum absorbed power density (S_A) for 4 cm^2 and 1 cm^2 areas, we can determine the position error of the area (A). The

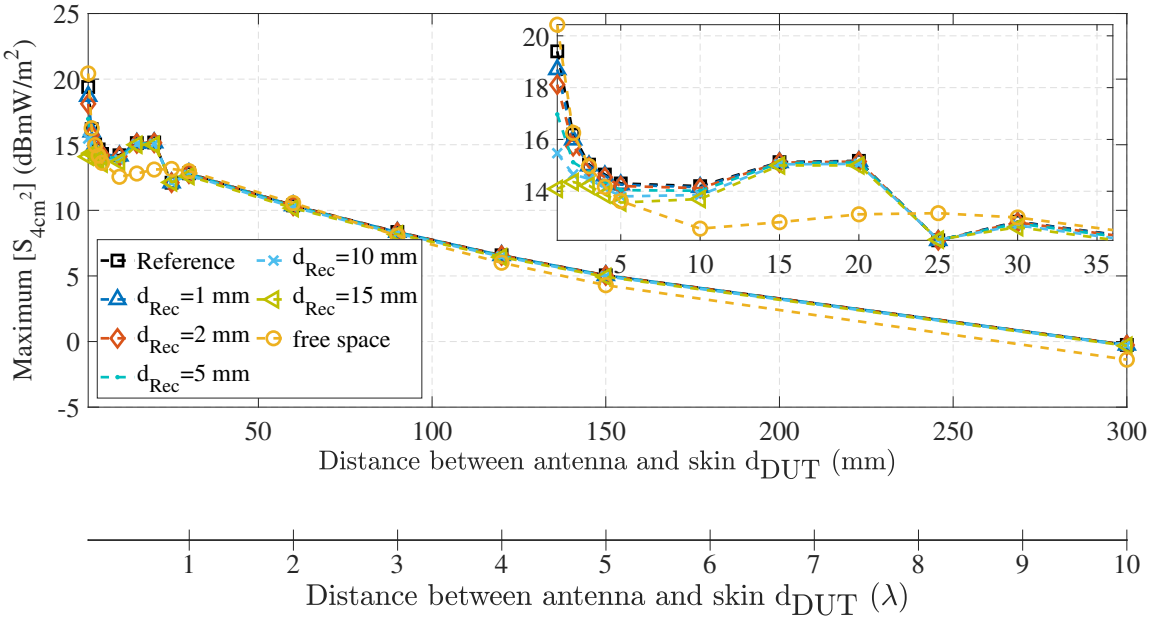

Figure 3.6: Max S_{4cm^2} (f = 10 GHz) [dB]

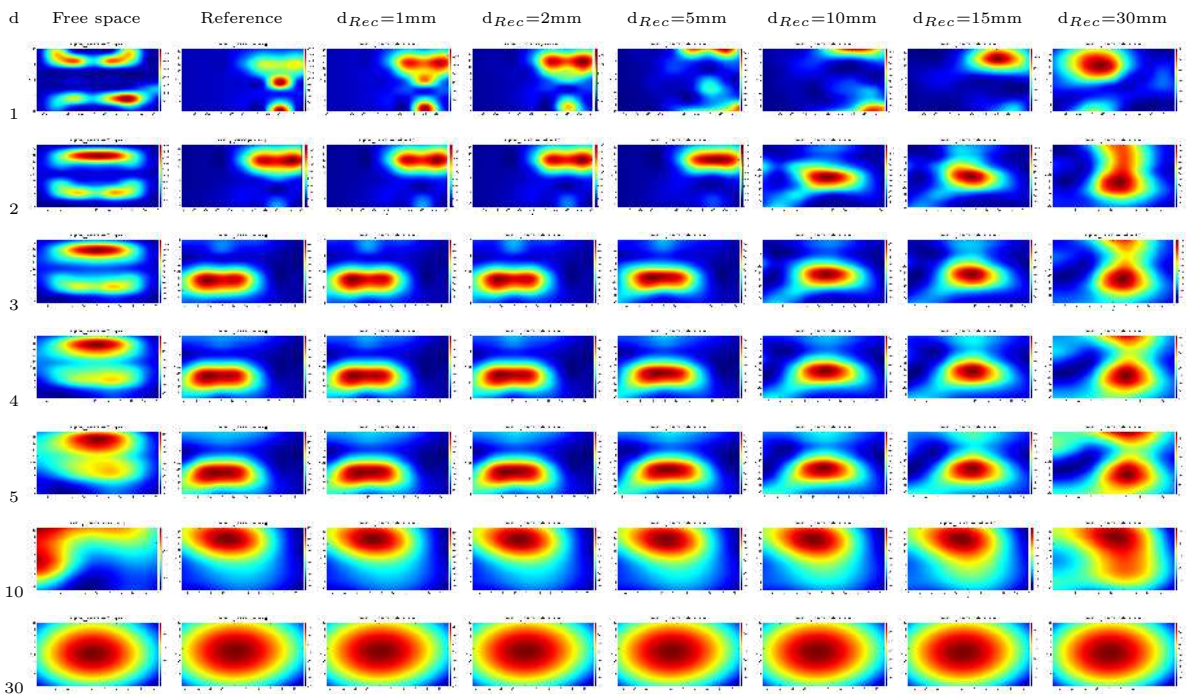

Figure 3.7: Distribution and position of Max S_{4cm^2} [dB] (f = 10 GHz) [d = d_{DUT} (mm)]

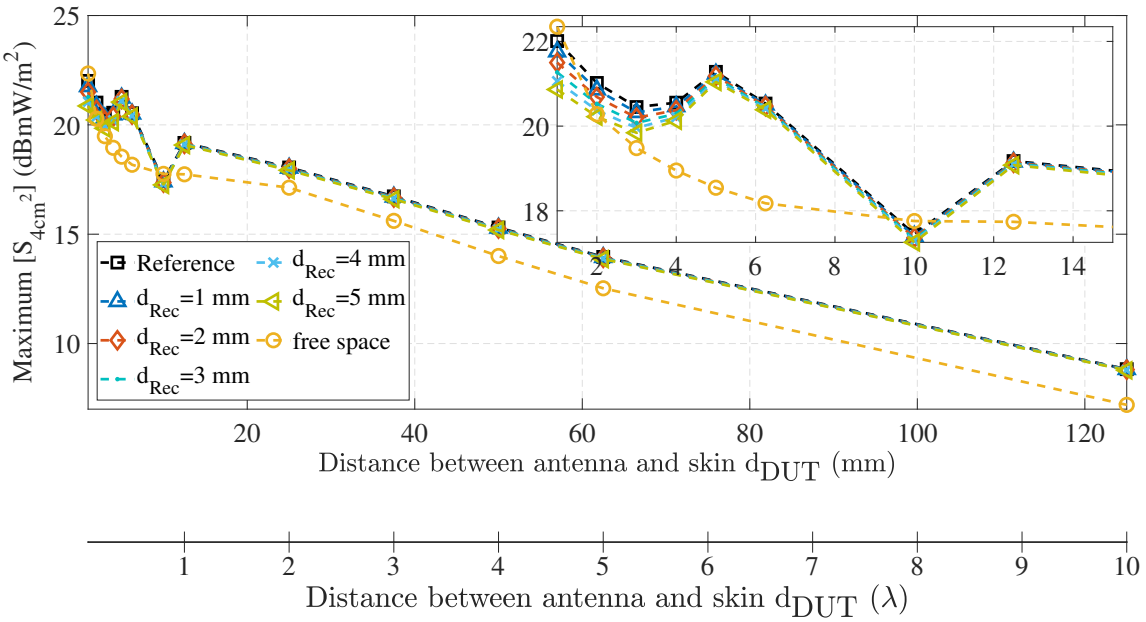

Figure 3.8: Max S_{4cm^2} (f = 24 GHz) [dB]

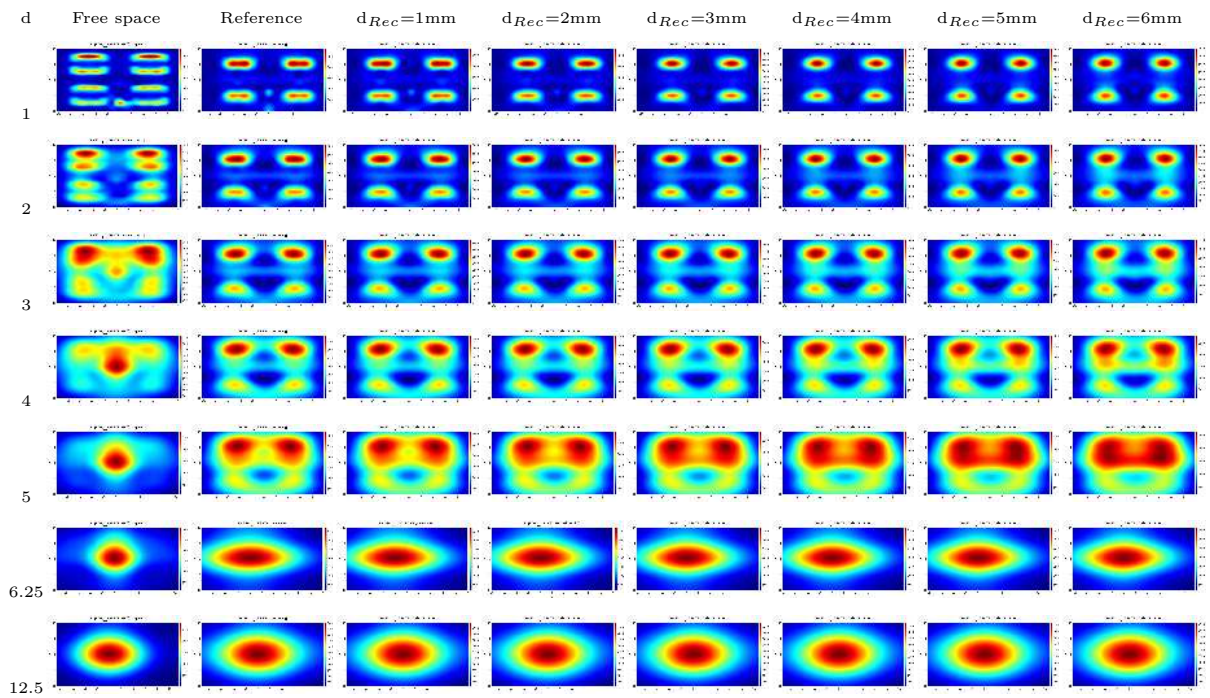

Figure 3.9: Distribution and position of Max S_{4cm^2} [dB] (f = 24 GHz) [d = d_{DUT} (mm)]

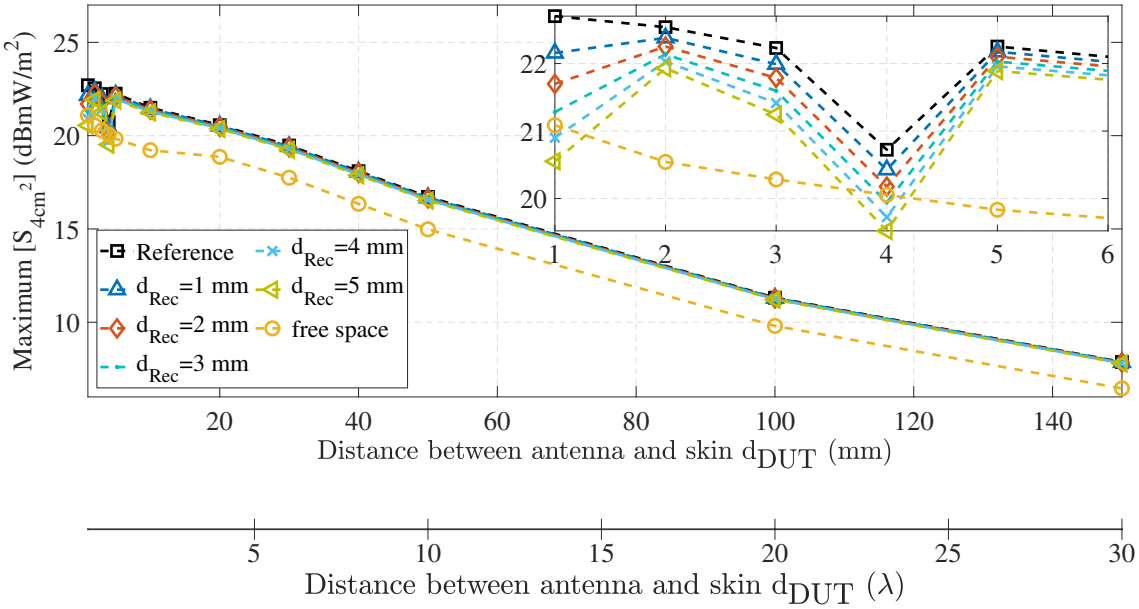

Figure 3.10: Max S_{4cm^2} ($f = 60$ GHz) [dB]

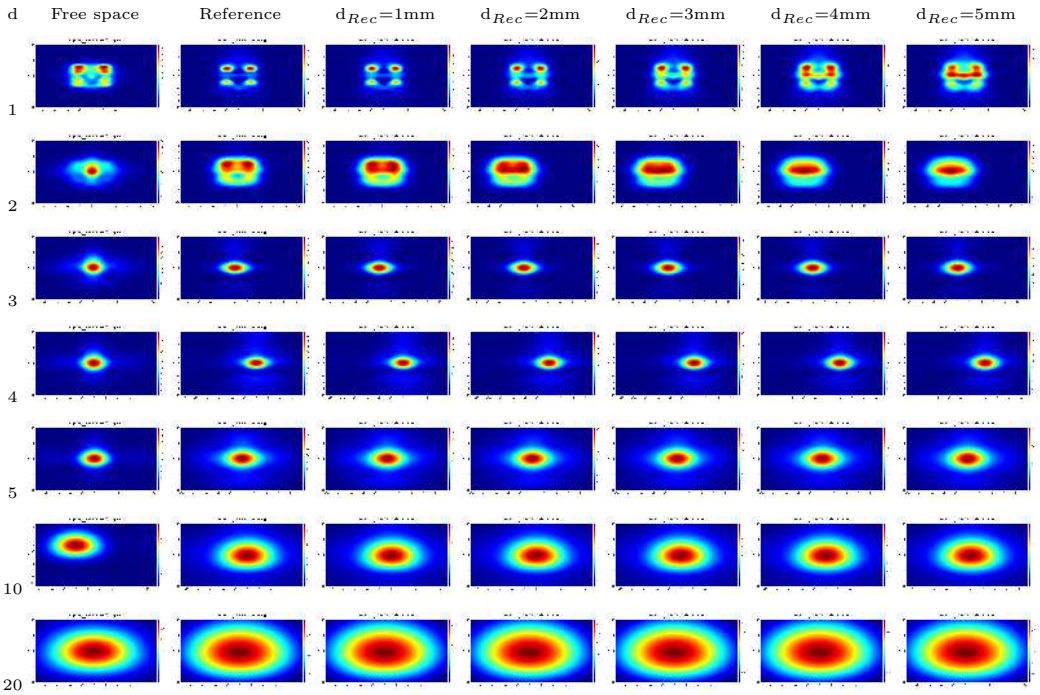

Figure 3.11: Distribution and position of Max S_{4cm^2} [dB] ($f = 60$ GHz) [$d = d_{DUT}$ (mm)]

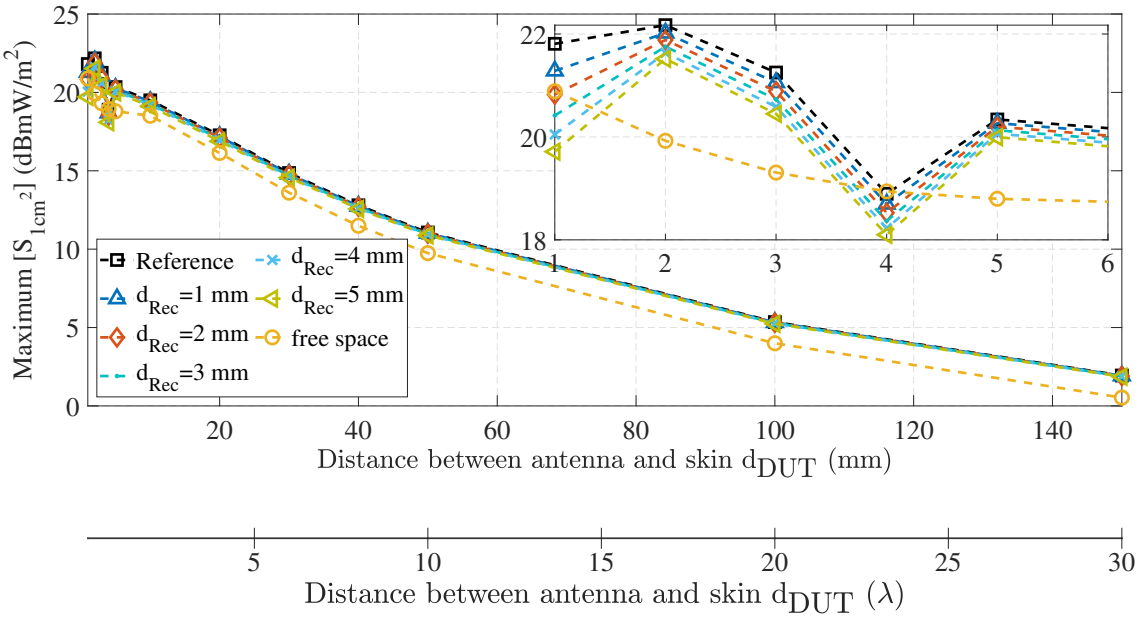

Figure 3.12: Max S_{1cm^2} (f = 60 GHz) [dB]

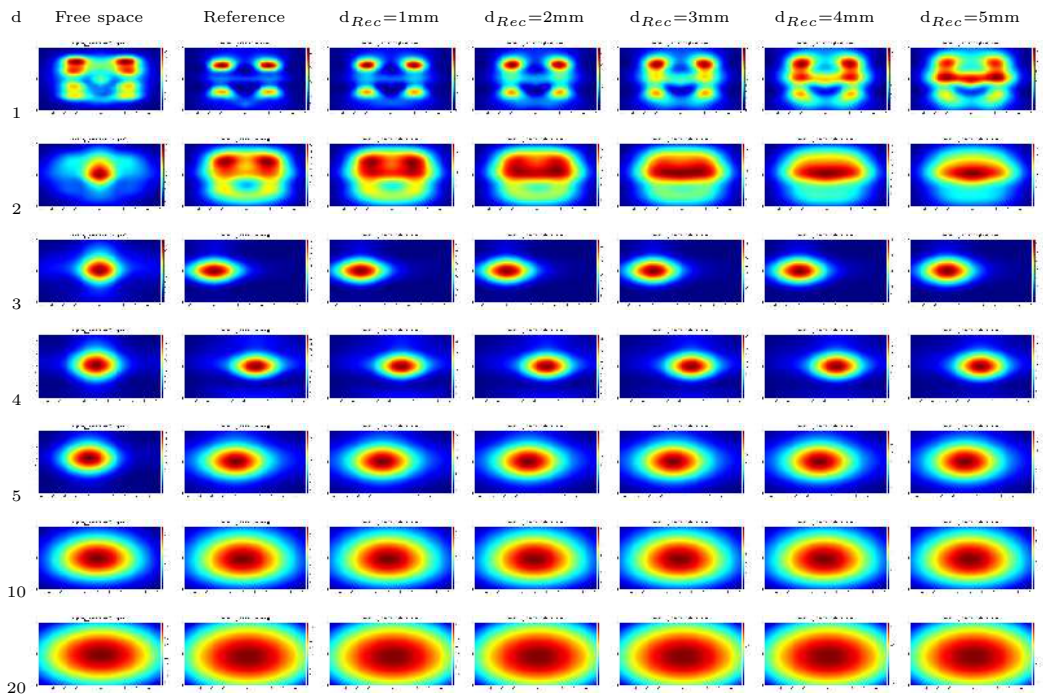

Figure 3.13: Distribution and position of Max S_{1cm^2} [dB] (f = 60 GHz) [d = d_{DUT} (mm)]

position error is defined as the distance between the centers of A obtained by the d_{Rec} scenarios and the reference, where the maximum S_A occurs. The position errors, measured in millimeters, are presented in Tables 3.2, 3.3, and 3.4 for frequencies of 10 GHz, 24 GHz, and 60 GHz, respectively. Each row in the tables corresponds to a specific d_{Rec} scenario, ranging from $\lambda/30$ to λ (1 mm to 30 mm) at 10 GHz, 1 mm $\leq d_{Rec} \leq$ 6 mm at 24 GHz, and 1 mm $\leq d_{Rec} \leq$ 5 mm at 60 GHz. Each column represents a specific separation distance from the antenna (d_{DUT}). The average error for each scenario is shown in the last column of the tables.

Analyzing the tables, we observe that the error in the free space scenario varies for different d_{DUT} values, rendering the method unreliable. This variation in error arises from the neglect of the coupling effect in the free space scenario. The accuracy of the response is expected to increase as the sampling point approaches the surface of the phantom, allowing for the detection of evanescent waves carrying field information due to the coupling effect. As the separation distance (d_{Rec}) increases, the reconstruction accuracy decreases.

In Table 3.2, the minimum error in the free space scenario occurs at d_{DUT} = 30 mm. The average errors range from less than 1 mm for d_{Rec} = 1 mm and 2 mm scenarios to between 1 mm and 10 mm for other d_{Rec} scenarios. In Table 3.3, the average error is less than or equal to 0.1 mm for d_{Rec} = 1 mm, 2 mm, and 3 mm scenarios, and between 0.1 mm and 0.21 mm for other d_{Rec} scenarios. In Table 3.4, for A = 4 cm^2, the average error is less than 0.1 mm for d_{Rec} = 1 mm scenario, and ranges from 0.34 mm to 0.36 mm for other d_{Rec} scenarios. For A = 1 cm^2, the average error is less than 0.1 mm for d_{Rec} = 1 mm, 2 mm, 3 mm, and 4 mm scenarios, and is 0.12 mm for the d_{Rec} = 5 mm scenario.

As expected, the error decreases as the separation distance (d_{DUT}) increases. As the distance increases, the human body model moves from the reactive near-field region to the radiation near-field region. Consequently, at further distances from the antenna, where the beam is formed, the centers of the averaged areas for APD evaluation from the proposed method and the reference align more closely. Similarly, the error decreases as the separation distance (d_{Rec}) decreases.

Comparing the three tables, we observe that at 60 GHz, the average error is significantly reduced compared to 24 GHz, and 24 GHz has lower errors compared to 10 GHz. Overall, all scenarios yield better results than the free space scenario.

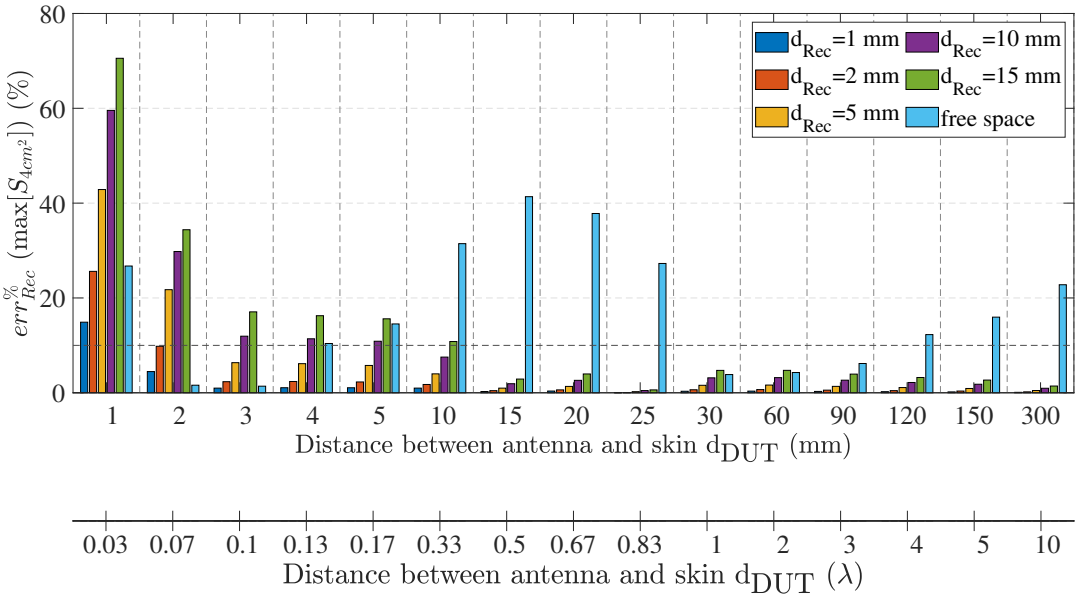

Figure 3.14: Error of max S_{4cm^2} (f = 10 GHz)

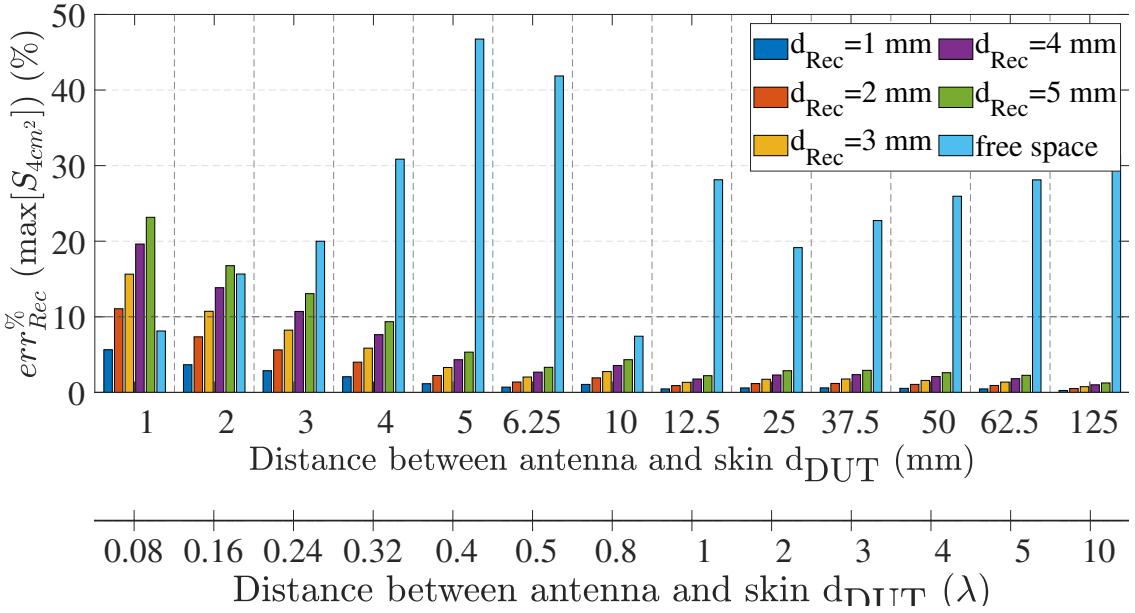

Figure 3.15: Error of max S_{4cm^2} (f = 24 GHz)

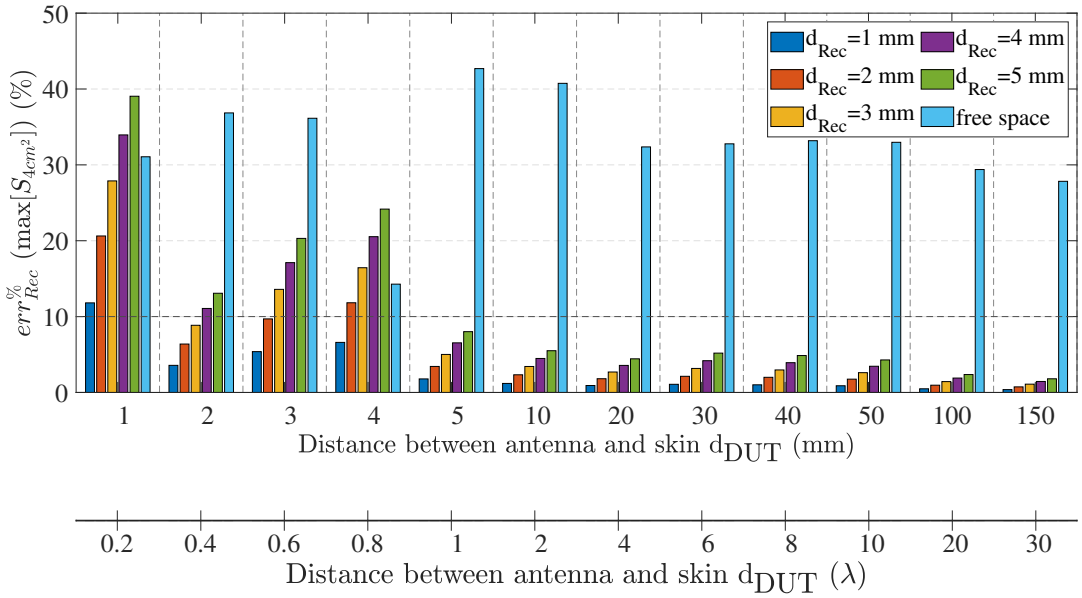

(a)

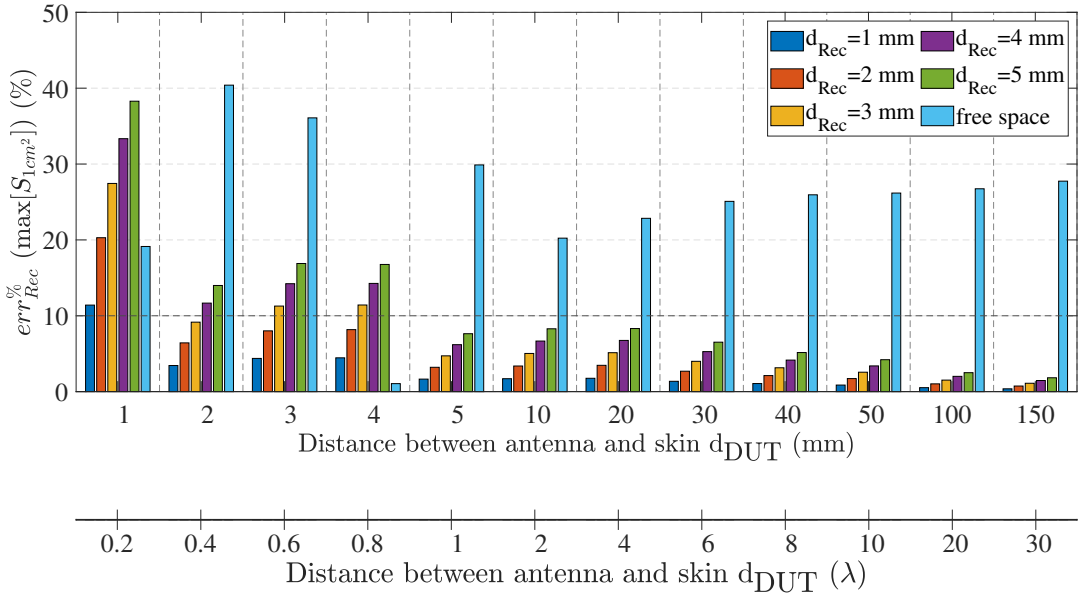

(b)

Figure 3.16: Error of (a) max S_{4cm^2} (b) max S_{1cm^2} (f = 60 GHz)

Table 3.2: Position error of A where max S_A happens [in mm] (f = 10 GHz)

A	d_{DUT} =	1mm	2mm	3mm	4mm	5mm	10mm	30mm	$error_{ave}$
$4cm^2$	Free space	9.9	30.5	21.24	20.57	19.86	7.02	0.51	15.66
	d_{Rec}=30mm	10.04	33.36	5.54	5.94	5.72	2.80	0.61	9.14
	d_{Rec}=15mm	2.26	34.83	4.87	5	4.53	1.26	0.3	7.58
	d_{Rec}=10mm	6.8	34.31	4.96	4.71	3.96	0.76	0.2	7.96
	d_{Rec}=5mm	7.2	0.42	1.1	1.48	2.21	0.5	0.1	1.86
	d_{Rec}=2mm	1.17	0.32	0.22	0.36	0.45	0.29	0	0.4
	d_{Rec}=1mm	0.61	0.22	0.22	0.22	0.32	0.14	0	0.25

Table 3.3: Position error of A where max S_A happens [in mm] (f = 24 GHz)

A	d_{DUT} =	1mm	2mm	3mm	4mm	5mm	6.25mm	12.5mm	$error_{ave}$
$4cm^2$	Free space	0.7	0.5	0.4	0.5	0.5	1.6	0.6	0.69
	d_{Rec}=6mm	0.8	0.1	0	0.1	0	0.4	0.1	0.21
	d_{Rec}=5mm	0.6	0.1	0	0.1	0	0.3	0.1	0.17
	d_{Rec}=4mm	0.4	0.1	0	0.1	0	0.2	0.1	0.13
	d_{Rec}=3mm	0.3	0	0	0.1	0	0.2	0.1	0.1
	d_{Rec}=2mm	0.3	0	0	0.1	0	0.1	0	0.07
	d_{Rec}=1mm	0.4	0	0	0.1	0	0	0	0.07

Table 3.4: Position error of A where max S_A happens [in mm] (f = 60 GHz)

A	d_{DUT} =	1mm	2mm	3mm	4mm	5mm	10mm	20mm	$error_{ave}$
$4cm^2$	Free space	0.32	0.3	0.6	2.8	0.4	5.3	0	2.08
	d_{Rec}=5mm	0	2.01	0.5	0.6	0	0.3	0.10	0.36
	d_{Rec}=4mm	0	2.21	0.4	0.6	0	0.2	0	0.36
	d_{Rec}=3mm	0	2.31	0.3	0.5	0	0.2	0	0.34
	d_{Rec}=2mm	0	2.4	0.2	0.5	0	0.1	0	0.34
	d_{Rec}=1mm	0	0.1	0.1	0.3	0	0.1	0	0.09
$1cm^2$	Free space	0.1	0.1	2.6	1.2	0.51	0	0.1	2.43
	d_{Rec}=5mm	0	0	0.6	0.1	0.3	0.1	0	0.12
	d_{Rec}=4mm	0	0	0.4	0	0.3	0.1	0	0.09
	d_{Rec}=3mm	0	0	0.3	0	0.2	0.1	0	0.08
	d_{Rec}=2mm	0	0	0.2	0	0.2	0.1	0	0.08
	d_{Rec}=1mm	0	0	0.1	0	0.1	0	0	0.05

3.4.3 Sampling plane size

In the PWS method, spatial integration is required to calculate the power density (see (2.2)). However, it is not feasible to consider an infinite plane that encompasses all the fields' power. Therefore, it is necessary to truncate the integration plane appropriately to introduce only a minor error in the power density calculation. The size of the truncated plane becomes smaller when the antenna has a directional radiation pattern or when the distance between the integration plane and the antenna is small. Consequently, it is the extent of the antenna's radiation pattern that determines the maximum size of the sampling plane.

On the other hand, the sampling grid step size (Δ) needs to be chosen carefully. It should be small enough to capture all the critical data accurately, while also being large enough to minimize the sampling and computation time. To determine the appropriate grid size, various plane sizes ranging from $0.8\lambda \times 0.8\lambda$ to $8\lambda \times 8\lambda$ and different step sizes ranging from $2\lambda/5$ to $\lambda/10$ are considered. By experimenting with different plane sizes and step sizes, the optimal combination can be determined, balancing the need for accuracy and efficiency in the PWS method.

Figure 3.17 illustrates that the highest errors occur at $d_{DUT} < \lambda/3$ when using a smaller number of samples, and these errors decrease as the frequency increases. At 10 GHz, for $d_{DUT} < 5$ mm, a smaller error occurs with a larger Δ because the sampling positions are varied and the peak of the power is captured. At frequencies of 10, 24, and 60 GHz, when $d_{DUT} > \lambda/3$, the errors are acceptable even for smaller plane sizes such as $1.2\lambda \times 1.2\lambda$, $1.6\lambda \times 1.6\lambda$, and $2\lambda \times 2\lambda$ with corresponding step sizes of $\Delta = 2\lambda/5$,

Table 3.5: Sampling plane and grid step size.

	f (GHz)	Δ (mm)	Sampling plane size
[49]	15	8	3.2 m × 3.2 m (401 × 401 points)
	30	4	1.6 m × 1.6 m (401 × 401 points)
	60	2	80 cm × 80 cm (401 × 401 points)
This thesis	10	6	4.8 cm × 4.8 cm (9 × 9 points)
	24	2.5	2 cm × 2 cm (9 × 9 points)
	60	2	1 cm × 1 cm (6 × 6 points)

respectively. It is important to note that larger antenna patterns require larger plane sizes. In this study, a plane size of $1.6\lambda \times 1.6\lambda$ and an optimal step size of $\lambda/5$ were chosen at 10 and 24 GHz, while a plane size of $2\lambda \times 2\lambda$ with $\Delta = 2\lambda/5$ was selected at 60 GHz. It is worth mentioning that all the results were obtained with the sampling plane's center aligned with the center of the antenna.

In a previous study [49], a measurement plane with dimensions of 401×401 points was employed at a separation distance of 5λ as d_{DUT} (in the absence of human skin) to evaluate the IPD. By comparing the information presented in Table 3.5 with the previous results obtained in this current study, it can be concluded that, despite differences in the exposure criterion between the proposed method and the previous study, the proposed method generally achieves higher accuracy with a smaller sample plane size.

3.4.4 Antenna position error

To ensure the practicality and realism of the proposed method, it is important to have a small and appropriate size for the sampling plane. However, the position of the maximum S_A is dependent on factors such as the size of the antenna, the radiation beam pattern, and the separation distance (d_{DUT}). In real-world scenarios, the exact position of the antenna within the user's device is often unknown, leading to potential misalignment between the sampling plane and the actual location where the maximum S_A occurs (as shown in Figure 3.18(a)). The parameter d_{offset} represents the horizontal deviation distance between the center of the antenna and the center of the sampling plane. Therefore, an analysis was conducted to examine the sensitivity of the antenna position in the proposed method.

Figure 3.18(b) presents a color-coded table displaying the errors in the maximum S_{1cm^2} for $d_{DUT} = 2$ mm, resulting from the deviation between the centers of the antenna and the sampling plane at 60 GHz. Please note that the errors displayed in this figure are not relative to the reconstructed APD with zero misalignment, but rather to the reference with zero misalignment. The deviations are considered in the XY-direction within the ranges of -12 to 12 mm, -10 to 10 mm, and -5 to 5 mm, with step sizes of 3 mm, 2.5 mm, and 1 mm, respectively. As depicted in Figure 3.18(b), the errors exhibit symmetry with respect to the y-axis. The asymmetry observed along the x-axis can be attributed to the antenna's structural configuration, specifically the interruption of symmetry caused by

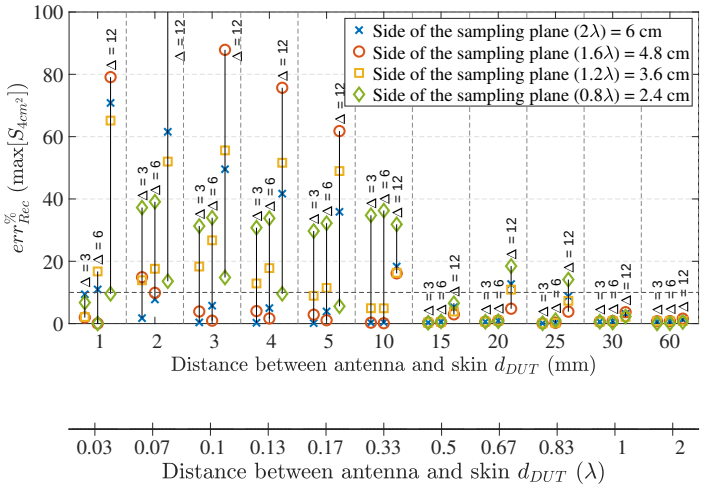

(a)

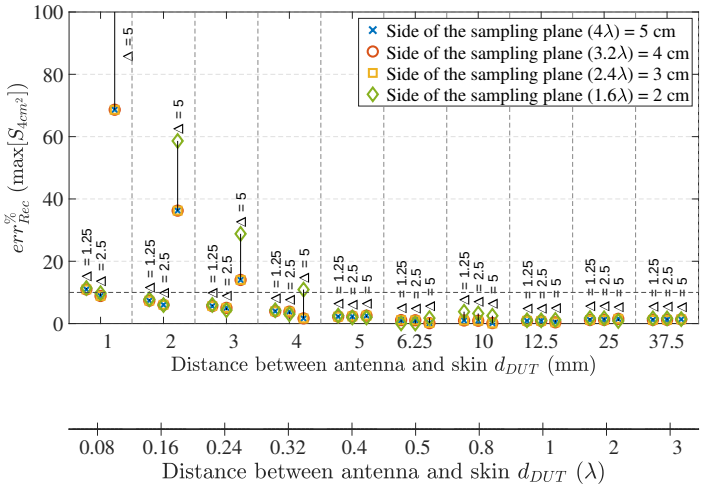

(b)

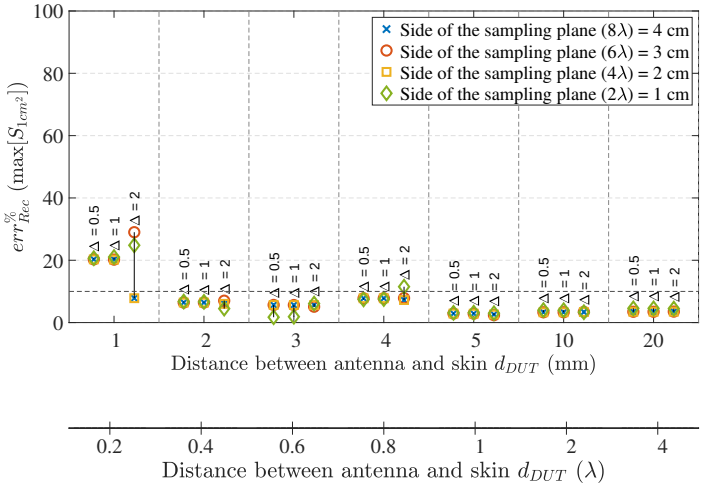

(c)

Figure 3.17: Sensitive analysis of sampling plane size to assess maximum S_A using an averaging area of (a) 4cm^2 at 10 GHz, (b) 4cm^2 at 24 GHz, and (c) 1cm^2 at 60 GHz for a d_{Rec} = 2 mm.

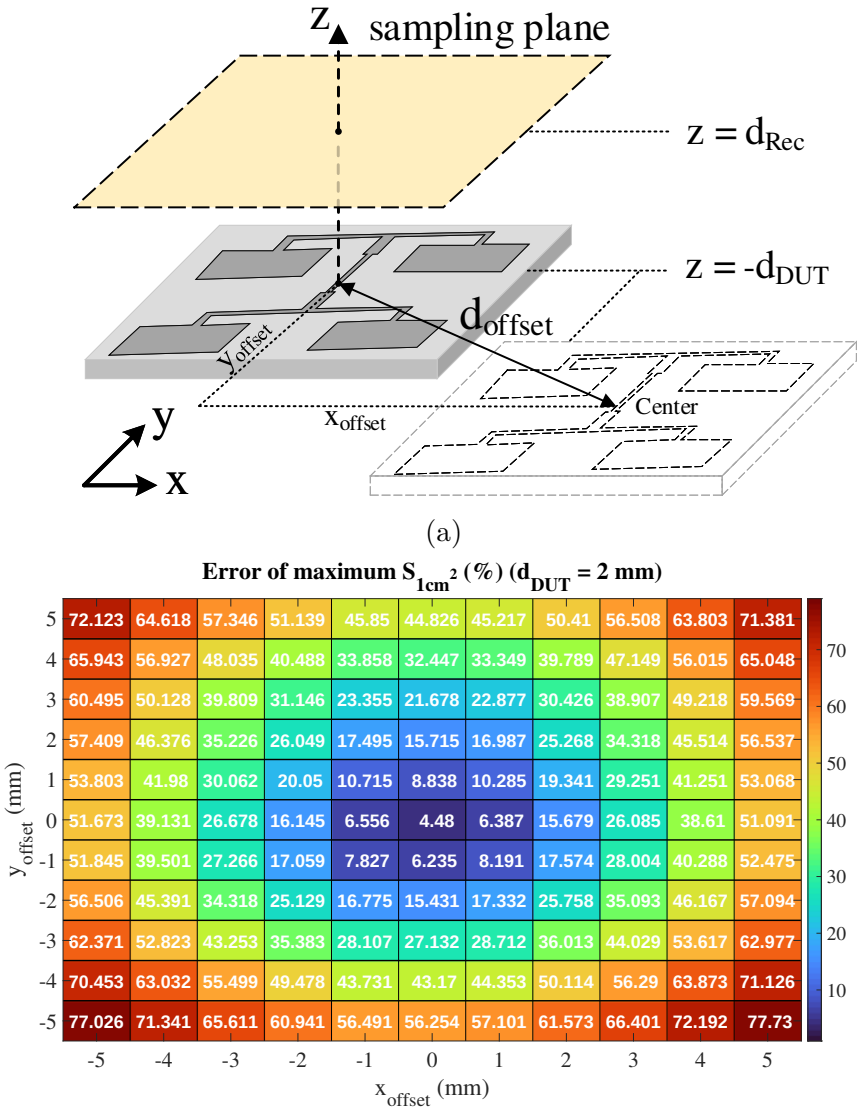

Figure 3.18: (a) Antenna position offset compared to the sampling plane and (b) its relevant maximum S_A error for a sampling plane size of 1 cm × 1 cm and $\Delta = 2$ mm at 60 GHz for a $d_{Rec} = 2$ mm and $d_{DUT} = 3$ mm.

the feeding lines. Figure 3.19 illustrates the mean errors for each antenna-body interval corresponding to the same deviation distance from the center.

Based on the analysis, it is observed that the errors remain below 10% for $d_{offset} \leq 3$ mm, except for the case of $d_{DUT} = 2$ mm at 10 GHz. Similarly, for $d_{offset} \leq 2.7$ mm, the errors stay within acceptable limits, except for the scenario of $d_{DUT} = 1$ mm at 24 GHz. At 60 GHz, the errors remain below the 10% threshold for $d_{offset} \leq 2.7$ mm, except for the cases of $d_{DUT} = 1$ mm and $d_{DUT} = 2$ mm.

From these findings, it can be concluded that the contribution of deviation error, for a fixed d_{offset} (mm), becomes more significant as the frequency increases. Therefore, careful consideration should be given to minimizing the deviation between the antenna

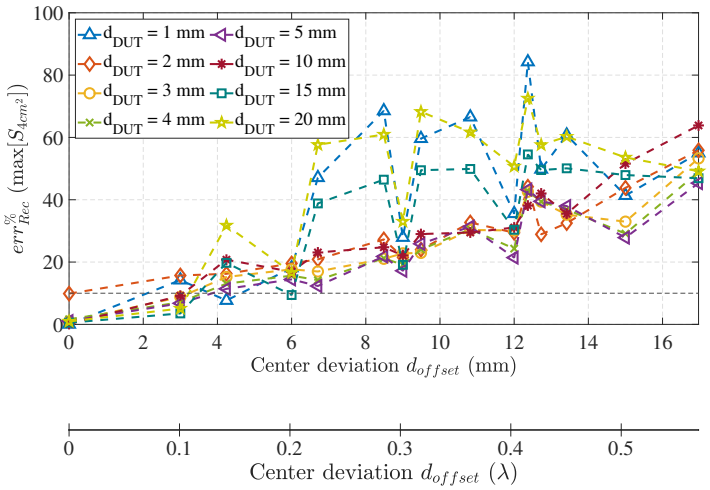

(a)

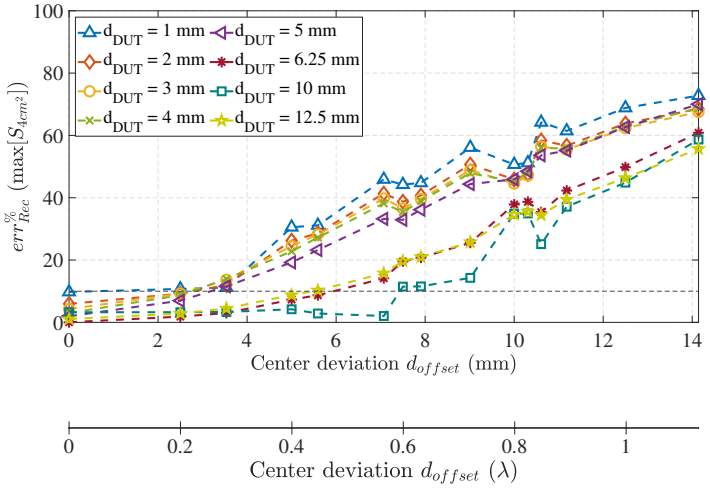

(b)

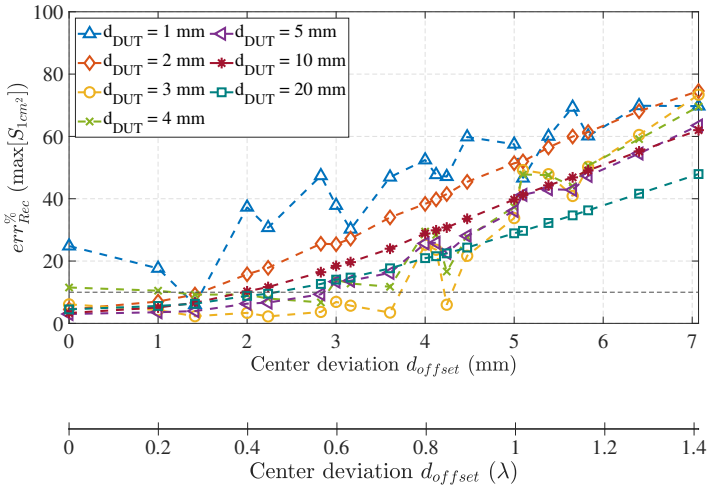

(c)

Figure 3.19: Error of maximum S_A due to antenna's and sampling plane's center deviation using the plane size of (a) 4.8 cm × 4.8 cm and $\Delta = 6$ mm at 10 GHz, (b) 2 cm × 2 cm and $\Delta = 2.5$ mm at 24 GHz, and (c) 1 cm × 1 cm and $\Delta = 2$ mm at 60 GHz for a d_{Rec} = 2 mm.

and the sampling plane, particularly at higher frequencies, to ensure accurate results within acceptable error limits.

3.4.5 E-field measurement requirement

When measuring the field inside human tissue at high frequencies, the first question is if the field is detectable inside the tissue. Thus, in this section, two important issues of electric field amplitude detection and electric field phase error are discussed.

3.4.5.1 E-field's amplitude detection

To address a potential challenge to the method, we can re-simulate the scenarios while considering the detection limit imposed by the minimum detection limit (MDL) of the measurement probe. In this case, we set the MDL values to 0.5 V/m, 1 V/m, and 2 V/m. The new results, accounting for this limitation, are denoted with superscripts of "0.5V/m," "1V/m," and "2V/m."

For the "0.5V/m" scenario, if the amplitude of the electric field at any sampling point on the sampling plane is less than 0.5 V/m, its value is set to zero. Similarly, for the "1V/m" and "2V/m" scenarios, the threshold values are set to 1 V/m and 2 V/m, respectively. By applying these thresholds, we can evaluate the impact of the MDL on the obtained results.

Performing the simulations with the MDL consideration allows us to assess the robustness of the method and analyze the effects of the detection limit on the calculated field values. The new results provide insights into the scenarios where the measured electric field is close to or below the MDL of the measurement probe.

Figure 3.20 illustrates the contribution error resulting from the MDL at the skin surface. The error is obtained by considering the "0.5V/m," "1V/m," and "2V/m" limit scenarios when $d_{Rec} = 2$ mm, considering various distances between the antenna and the skin at 60 GHz. The size of the sampling plane and the grid step size are determined according to Table 3.5.

For $d_{DUT} \leq \lambda$, where the antenna beam is still forming and is narrow compared to the sampling plane, the contribution errors increase significantly as the MDL increases from 0.5 V/m to 2 V/m. The contribution of MDL errors is limited to 0.15%, 0.58%, and 1.69% for MDL values of 0.5 V/m, 1 V/m, and 2 V/m, respectively. It is worth noting that the MDL for high-frequency measuring probes is typically around 0.8 V/m [115,116]. The maximum contribution error observed for this MDL limit is 0.31%, which occurs at $d_{DUT} = 3$ mm.

As d_{Rec} increases, it becomes more challenging to detect the electric fields accurately. Therefore, considering $d_{Rec} = 2$ mm, which yields the lowest error, remains suitable for assessing the APD.

3.4.5.2 E-field's phase error

To assess the phase uncertainty, a random error (ϕ^{error}) is introduced to the phase of the electric field on the sampling plane. This error follows a normal distribution with a standard deviation of σ. To estimate the contribution error, a Monte Carlo (MC)

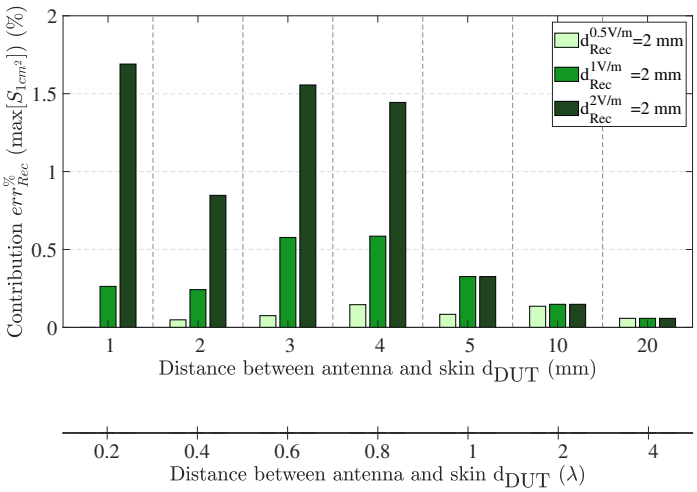

Figure 3.20: Contribution error due to MDL to assess the maximum S_{1cm^2} with the sampling plane of 1 cm × 1 cm and $\Delta = 2$ mm at 60 GHz.

simulation is performed with 1000 iterations. The phase distribution of the electric field, taking into account the errors, on the sampling plane is modeled as follows:

$$\measuredangle E^{MC}_{x,y}(x, y, d_{Rec}) = \measuredangle E^{Rec}_{x,y}(x, y, d_{Rec}) + \phi^{error}(\sigma), \tag{3.5}$$

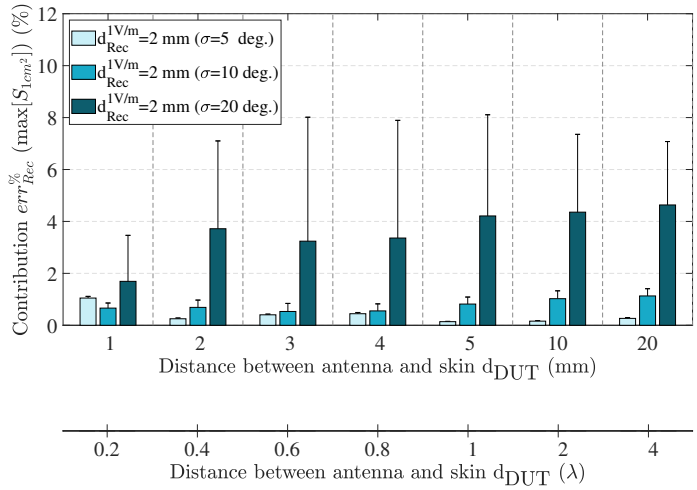

Figure 3.21: Mean contribution of combined error due to MDL of 1 V/m and phase error with the standard deviation of 5, 10, 20 degrees to assess the maximum S_{1cm^2} with the sampling plane of 1 cm × 1 cm and $\Delta = 2$ mm at 60 GHz.

where $\measuredangle E^{MC}_{x,y}$ and $\measuredangle E^{Rec}_{x,y}$ are the E-field's phase at the sampling plane with and without error, respectively.

The average contribution errors due to phase uncertainty are as follows: 0.33% for $\sigma = 5$ degrees, 1.2% for $\sigma = 10$ degrees, and 4.61% for $\sigma = 20$ degrees. These errors were estimated using Monte Carlo simulation with 1000 iterations, considering normally distributed random errors added to the E-field's phase on the sampling plane.

Figure 3.21 illustrates the combined contribution error due to both phase uncertainty and MDL for the maximum S_{1cm^2} at d_{Rec} = 2 mm and 60 GHz. The means of the combined errors are represented by the bars in the figure. The standard deviations, indicating the range of variation, are displayed at the top of each bar. The maximum mean combined contribution error, considering an MDL of 1 V/m, is obtained as 1.05%, 1.13%, and 4.63% for σ = 5, 10, and 20 degrees, respectively. It is interesting to note that the phase contribution error shows less sensitivity to the distance between the antenna and the DUT (d_{DUT}) compared to the MDL contribution error.

These findings highlight the importance of considering both phase uncertainty and MDL in the evaluation of the combined contribution error in the measurement system. While the phase contribution error increases with larger phase uncertainties (higher values of σ), the MDL contribution error is influenced by the detection limit of the measurement probe. By understanding and quantifying these sources of error, more accurate and reliable assessment of the APD can be achieved, providing valuable insights for compliance testing and safety evaluations in the field of electromagnetic radiation.

Chapter 4

APD assessment by equivalent current reconstruction method

When studying the APD in human exposure scenarios, it is common to place the antenna in close proximity to the human body, where the surface of the body can be approximated as a flat plane from the antenna's perspective. This approximation is valid when the investigated wavelength is significantly smaller than the dimensions of the body part under consideration. This assumption is justified in studies such as [69, 89], particularly in the context of millimeter-wave frequencies. Some research reports have explored the curvature radius of body parts to account for non-planar phantoms in studies like [117–119]. As a result, the problem space can be divided into two semi-infinite layers. The upper layer ($z > 0$) represents the air with properties of permittivity (ε_0) and permeability (μ_0), where the antenna is situated, while the lower layer represents the human body with its liquid/solid model. Here, ε_0 and μ_0 correspond to the vacuum permittivity and permeability, respectively. Therefore, this consideration leads to formulating and solving a problem involving a planar two-layered medium, as described in [120] and detailed in the following sections.

4.1 2-Layered planar medium

The electromagnetic problem in two half-space media was initially solved by Arnold Johannes Wilhelm Sommerfeld, a German theoretical physicist, in 1909 [121]. This simple yet ideal scenario sparked extensive discussions on the existence of surface waves along the boundary between the two media. A comprehensive review of these debates and subsequent developments can be found in [122]. Over time, the study of half-space media was extended to encompass multilayered mediums, forming the basis for several important topics and works [123–125]. The investigation of planar multilayered media provides a platform for addressing numerous scenarios encountered in geophysics, radio frequency (RF) devices, and nanostructures. Various techniques have been introduced to solve these problems, with the spectral domain transmission line (TL) model standing out as the most comprehensive and complete formulation. The TL model leverages the structural symmetry inherent in these configurations and offers an efficient solution [126].

In Figure 4.1, we address the scenario of a 2-layered planar structure consisting of isotropic media aligned along the z-axis. For simplicity, we assume there are two layers

of finite thickness, denoted as Layer 1 (air-filled) and Layer 2 (phantom). Each layer occupies the respective regions $0 \leq z \leq z_1$ and $z_2 \leq z \leq 0$, where z_1 and z_2 are the termination points of Layer 1 and Layer 2. Notably, each layer extends infinitely in the transverse x-y plane. This setup allows for numerical boundary specifications in field calculations. Additionally, this approach enables the definition of semi-infinite layers at Layer 1 and Layer 2 by appropriately setting boundary values at z_1 and z_2, respectively.

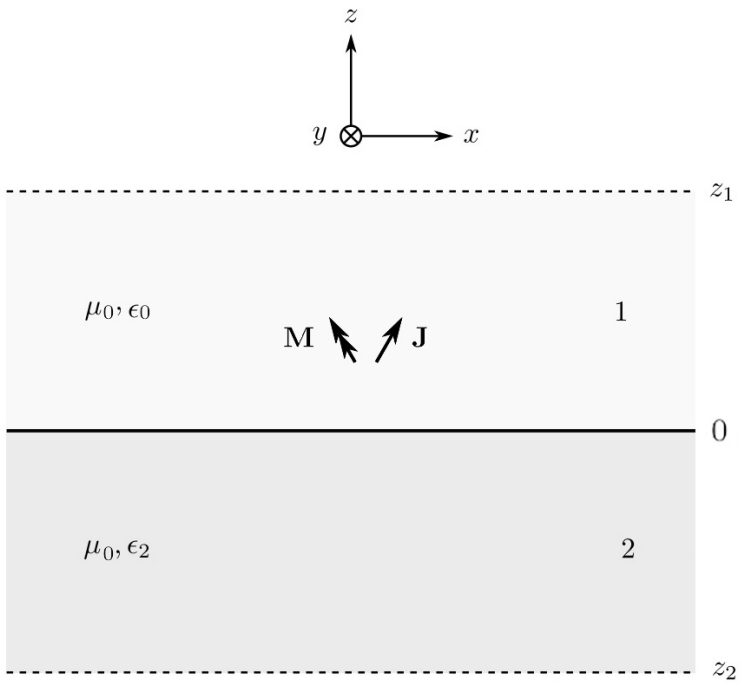

Figure 4.1: Structure of the 2-layered planar medium.

The problems to be addressed in this context involve determining the distribution of electric and magnetic currents, denoted as J and M, respectively, within the structure in Layer 1. By considering the fields in the time domain and their time dependence as $e^{j\omega t}$, Maxwell's equations can be expressed as follows:

$$\begin{aligned} -\nabla \times E &= j\omega\mu_0\mu H + M \\ \nabla \times H &= j\omega\varepsilon_0\varepsilon E + J \end{aligned} \tag{4.1}$$

The boundary conditions that ensure the continuity of transverse fields at $z = 0$:

$$\begin{aligned} \hat{z} \times [E_1 - E_2] &= 0 \\ \hat{z} \times [H_1 - H_2] &= 0 \end{aligned} \tag{4.2}$$

It should be noted that once the continuity of transverse fields is satisfied between two adjacent layers, the boundary conditions are automatically fulfilled.

4.1.1 Formulation

The goal is to ascertain the spatial Dyadic Green's Function, and this can be achieved through the utilization of the PWS method within the framework of a two-layered medium.

We can break down Maxwell's equations into transverse and longitudinal components based on the XY-plane boundary. By substituting Ez and Hz with the transverse component, we isolate the equation, retaining only the transverse component. This allows the implementation of the PWS method, as only x- and y-components remain. Further, field decomposition in the direction of propagation on the XY-plane and its orthogonal vector removes the dependency on k (radial wavenumber in Cylindrical coordination). After manipulation, separated Green's functions in the spectral domain for each source are obtained. Finally, formulations for each element of the Dyadic Green's Function matrix, involving Sommerfeld Integrals, are derived through the inverse Fourier Transform. The specific expressions for the components of the dyadic Green's functions in the spatial domain are as follows:

$$G_{xx}^{EJ}(\rho,\varphi,z|z') = -\frac{1}{2}S_0\left\{V_i^e + V_i^h\right\} + \frac{\cos(2\varphi)}{2}S_2\left\{V_i^e - V_i^h\right\} \tag{4.3}$$

$$G_{xy}^{EJ}(\rho,\varphi,z|z') = \frac{\sin(2\varphi)}{2}S_2\left\{V_i^e - V_i^h\right\} \tag{4.4}$$

$$G_{yx}^{EJ}(\rho,\varphi,z|z') = \frac{\sin(2\varphi)}{2}S_2\left\{V_i^e - V_i^h\right\} \tag{4.5}$$

$$G_{yy}^{EJ}(\rho,\varphi,z|z') = -\frac{1}{2}S_0\left\{V_i^e + V_i^h\right\} - \frac{\cos(2\varphi)}{2}S_2\left\{V_i^e - V_i^h\right\} \tag{4.6}$$

$$G_{xz}^{EJ}(\rho,\varphi,z|z') = \frac{\eta_0}{jk_0\varepsilon'}\cos(\varphi)S_1\left\{k_\rho V_v^e\right\} \tag{4.7}$$

$$G_{yz}^{EJ}(\rho,\varphi,z|z') = \frac{\eta_0}{jk_0\varepsilon'}\sin(\varphi)S_1\left\{k_\rho V_v^e\right\} \tag{4.8}$$

$$G_{zx}^{EJ}(\rho,\varphi,z|z') = \frac{\eta_0}{jk_0\varepsilon}\cos(\varphi)S_1\left\{k_\rho I_i^e\right\} \tag{4.9}$$

$$G_{zy}^{EJ}(\rho,\varphi,z|z') = \frac{\eta_0}{jk_0\varepsilon}\sin(\varphi)S_1\left\{k_\rho I_i^e\right\} \tag{4.10}$$

$$G_{zz}^{EJ}(\rho,\varphi,z|z') = -\frac{\eta_0^2}{jk_0^2\varepsilon\varepsilon'}S_0\left\{k_\rho^2 I_v^e\right\} - \frac{\eta_0}{jk_0\varepsilon}\delta(\rho)\delta(z-z') \tag{4.11}$$

$$G_{xx}^{HJ}(\rho,\varphi,z|z') = \frac{\sin(2\varphi)}{2}S_2\left\{I_i^h - I_i^e\right\} \tag{4.12}$$

$$G_{xy}^{HJ}(\rho,\varphi,z|z') = \frac{1}{2}S_0\left\{I_i^h + I_i^e\right\} - \frac{\cos(2\varphi)}{2}S_2\left\{I_i^h - I_i^e\right\} \tag{4.13}$$

$$G_{yx}^{HJ}(\rho,\varphi,z|z') = -\frac{1}{2}S_0\left\{I_i^h + I_i^e\right\} - \frac{\cos(2\varphi)}{2}S_2\left\{I_i^h - I_i^e\right\} \tag{4.14}$$

$$G_{yy}^{HJ}(\rho,\varphi,z|z') = -\frac{\sin(2\varphi)}{2}S_2\left\{I_i^h - I_i^e\right\} \tag{4.15}$$

$$G_{xz}^{HJ}(\rho,\varphi,z|z') = -\frac{\eta_0}{jk_0\varepsilon'}\sin(\varphi)S_1\left\{k_\rho I_v^e\right\} \tag{4.16}$$

$$G_{yz}^{HJ}(\rho,\varphi,z|z') = \frac{\eta_0}{jk_0\varepsilon'}\cos(\varphi)S_1\left\{k_\rho I_v^e\right\} \tag{4.17}$$

$$G_{zx}^{HJ}(\rho,\varphi,z|z') = \frac{1}{j\eta_0 k_0\mu}\sin(\varphi)S_1\left\{k_\rho V_i^h\right\} \tag{4.18}$$

$$G_{zy}^{HJ}(\rho,\varphi,z|z') = -\frac{1}{j\eta_0 k_0\mu}\cos(\varphi)S_1\left\{k_\rho V_i^h\right\} \tag{4.19}$$

$$G_{zz}^{HJ}(\rho,\varphi,z|z') = 0 \tag{4.20}$$

$$G_{xx}^{EM}(\rho,\varphi,z|z') = -\frac{\sin(2\varphi)}{2}S_2\left\{V_v^e - V_v^h\right\} \tag{4.21}$$

$$G_{xy}^{EM}(\rho,\varphi,z|z') = -\frac{1}{2}S_0\left\{V_v^e + V_v^h\right\} + \frac{\cos(2\varphi)}{2}S_2\left\{V_v^e - V_v^h\right\} \tag{4.22}$$

$$G_{yx}^{EM}(\rho,\varphi,z|z') = \frac{1}{2}S_0\left\{V_v^e + V_v^h\right\} + \frac{\cos(2\varphi)}{2}S_2\left\{V_v^e - V_v^h\right\} \tag{4.23}$$

$$G_{yy}^{EM}(\rho,\varphi,z|z') = \frac{\sin(2\varphi)}{2}S_2\left\{V_v^e - V_v^h\right\} \tag{4.24}$$

$$G_{xz}^{EM}(\rho,\varphi,z|z') = \frac{1}{j\eta_0 k_0\mu'}\sin(\varphi)S_1\left\{k_\rho V_i^h\right\} \tag{4.25}$$

$$G_{yz}^{EM}(\rho,\varphi,z|z') = -\frac{1}{j\eta_0 k_0\mu'}\cos(\varphi)S_1\left\{k_\rho V_i^h\right\} \tag{4.26}$$

$$G_{zx}^{EM}(\rho,\varphi,z|z') = \frac{j\eta_0}{k_0\varepsilon}\sin(\varphi)S_1\left\{k_\rho I_v^e\right\} \tag{4.27}$$

$$G_{zy}^{EM}(\rho,\varphi,z|z') = -\frac{j\eta_0}{k_0\varepsilon}\cos(\varphi)S_1\left\{k_\rho I_v^e\right\} \tag{4.28}$$

$$G_{zz}^{EM}(\rho,\varphi,z|z') = 0 \tag{4.29}$$

$$G_{xx}^{HM}(\rho,\varphi,z|z') = -\frac{1}{2}S_0\left\{I_v^h + I_v^e\right\} + \frac{\cos(2\varphi)}{2}S_2\left\{I_v^h - I_v^e\right\} \tag{4.30}$$

$$G_{xy}^{HM}(\rho,\varphi,z|z') = \frac{\sin(2\varphi)}{2}S_2\left\{I_v^h - I_v^e\right\} \tag{4.31}$$

$$G_{yx}^{HM}(\rho,\varphi,z|z') = \frac{\sin(2\varphi)}{2}S_2\left\{I_v^h - I_v^e\right\} \tag{4.32}$$

$$G_{yy}^{HM}(\rho,\varphi,z|z') = -\frac{1}{2}S_0\left\{I_v^h + I_v^e\right\} - \frac{\cos(2\varphi)}{2}S_2\left\{I_v^h - I_v^e\right\} \tag{4.33}$$

$$G_{xz}^{HM}(\rho,\varphi,z|z') = \frac{1}{j\eta_0 k_0\mu'}\cos(\varphi)S_1\left\{k_\rho I_i^h\right\} \tag{4.34}$$

$$G_{yz}^{HM}(\rho,\varphi,z|z') = \frac{1}{j\eta_0 k_0 \mu'}\sin(\varphi)S_1\left\{k_\rho I_i^h\right\} \tag{4.35}$$

$$G_{zx}^{HM}(\rho,\varphi,z|z') = \frac{1}{j\eta_0 k_0 \mu}\cos(\varphi)S_1\left\{k_\rho V_v^h\right\} \tag{4.36}$$

$$G_{zy}^{HM}(\rho,\varphi,z|z') = \frac{1}{j\eta_0 k_0 \mu}\sin(\varphi)S_1\left\{k_\rho V_v^h\right\} \tag{4.37}$$

$$G_{zz}^{HM}(\rho,\varphi,z|z') = -\frac{1}{\eta_0^2 k_0^2 \mu\mu'}S_0\left\{k_\rho^2 V_i^h\right\} - \frac{1}{j\eta_0 k_0 \mu}\delta(\rho)\delta(z-z') \tag{4.38}$$

where μ' and ε' are medium parameters in z'. For arbitrary source location, the following substitutions can be applied:

$$\begin{aligned} \rho \rightarrow & \rho = \sqrt{((x-x')^2 + (y-y')^2)} \\ \varphi \rightarrow & \varphi = \tan^{-1}\left[\frac{y-y'}{x-x'}\right] \end{aligned} \tag{4.39}$$

A comprehensive and detailed derivation is available in [120].

4.2 Problem definition

In the proposed method, the necessary data is obtained by sampling the electric fields on the surface of a hemisphere within the air layer. The selection of a hemispherical surface is advantageous as it ensures complete coverage of the regions, allowing for the capture of all incident fields from the source and scattered fields from the phantom, irrespective of the radiation pattern of the DUT. The problem configuration is depicted in Figure 4.2, where E-field probes are positioned on the air side of the interface, specifically on the surface of the hemisphere with a radius of R. The evaluation plane is assumed to be located below the air-phantom interface.

The radiated electric field is related to the electric current source by the DGF as follows [127]:

$$\overrightarrow{E}(r) = \int \overline{\overline{G}}(r,r') \cdot \overrightarrow{J}(r')dr', \tag{4.40}$$

where $\overrightarrow{E}$ and $\overrightarrow{J}$ are the radiated electric field and electric current density, respectively, and r and r' are the position vector of the electric field and electric current, respectively. The term $\overline{\overline{G}}$ is the spatial domain DGF.

The DUT is modeled as a sum of discrete point sources in the air layer. By decomposing the antenna to the discrete point sources in the x-, y-, and z-direction, there exists a total of nine DGFs for each observation and source point. Thus, (4.40) can be expressed in the form of a matrix equation for each observation-source point pair

$$\begin{bmatrix} E_x\hat{x} \\ E_y\hat{y} \\ E_z\hat{z} \end{bmatrix} = \begin{bmatrix} G_{xx}^{EJ}\hat{x}\hat{x} & G_{xy}^{EJ}\hat{x}\hat{y} & G_{xz}^{EJ}\hat{x}\hat{z} \\ G_{yx}^{EJ}\hat{y}\hat{x} & G_{yy}^{EJ}\hat{y}\hat{y} & G_{yz}^{EJ}\hat{y}\hat{z} \\ G_{zx}^{EJ}\hat{z}\hat{x} & G_{zy}^{EJ}\hat{z}\hat{y} & G_{zz}^{EJ}\hat{z}\hat{z} \end{bmatrix} \begin{bmatrix} J_x\hat{x} \\ J_y\hat{y} \\ J_z\hat{z} \end{bmatrix}, \tag{4.41}$$

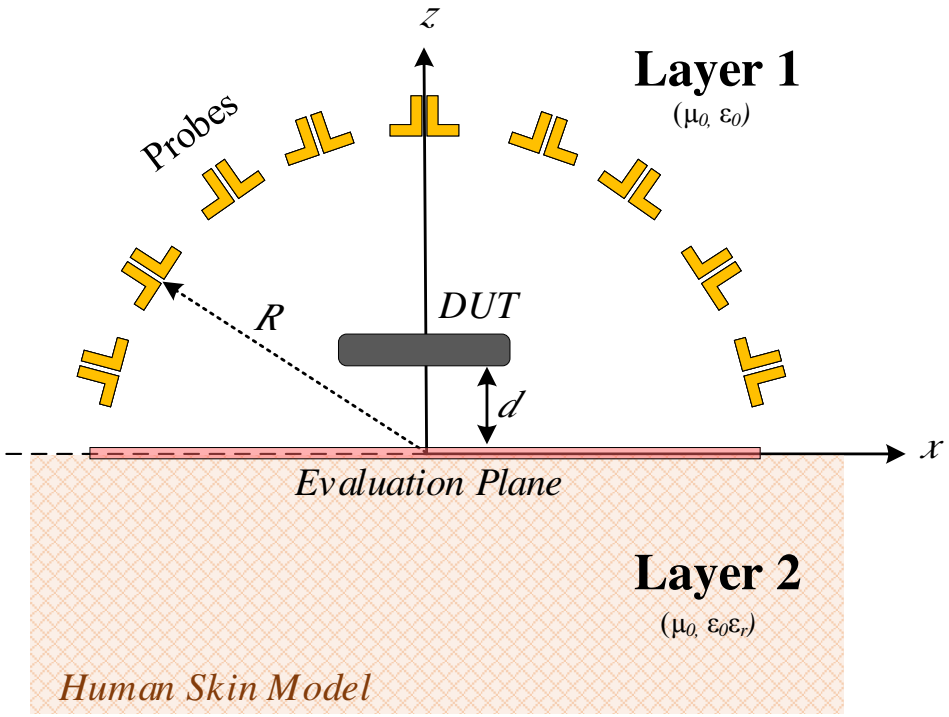

Figure 4.2: Schematic of the layered medium for the non-invasive APD assessment approach.

where $[G^{EJ}]$ is the DGF matrix for each observation-source point pair, $[E]$ is the sampled E-field matrix for each observation point, and $[J]$ is the source matrix for each source point. By considering the surface equivalence theorem [128], The antenna's surface is divided into multiple numbers (S) of infinitesimal point sources (I_n), representing the equivalent current sources (I_{Rec}). Therefore, the I_{Rec} can be expressed as the sum of S points.

$$I_{Rec} \approx \sum_{n=1}^{S} I_n, \tag{4.42}$$

where I_s is the unknown infinitesimal current for the nth point source. To obtain reasonable accuracy and avoid losing the vital data of the discrete sources, the distance of these sources is considered less or equal to $\lambda/10$.

Integrating (4.41) for all observation (N) and source (S) points results in a matrix equation as given in the following

$$\begin{bmatrix} [G^{EJ}]_{11} & \dots & [G^{EJ}]_{1S} \\ \vdots & \ddots & \vdots \\ [G^{EJ}]_{N1} & \dots & [G^{EJ}]_{NS} \end{bmatrix} \begin{bmatrix} [J]_1 \\ \vdots \\ [J]_S \end{bmatrix} = \begin{bmatrix} [E]_1 \\ \vdots \\ [E]_N \end{bmatrix}, \tag{4.43}$$

which can be linked to the MoM matrix equation

$$[Z]_{3N\times 3S}[I]_{3S\times 1} = [V]_{3N\times 1}, \tag{4.44}$$

where $[V]$ is the sampled/measured E-field's xyz-components, including the incident field plus the scattered field from the phantom on the hemisphere's surface. $[Z]$ is the DGF matrix, the MoM impedance matrix. (4.44) can be viewed as an inverse source problem and solved inversely to determine the equivalent source current ($[I]$). In the inverse source problem, the inverse of the $[Z]$ matrix is regularized by Tikhonov regularization, whose regularization parameter is specified by the L-curve method, to avoid ill-conditioning and minimize the measurement noise [129]. With the reconstructed equivalent currents, (4.44) is solved again, but this time directly to assess transmitted fields through the phantom with the observation points on the evaluation plane. Then, the APD is evaluated using the obtained E- and H-field on the evaluation plane. The code is developed within chaire C2M, Télécom Paris, drawing inspiration from Dr. Mazin Mustafa's code [130, 131]

Since the DGF matrix includes Sommerfeld integrals, basis functions (e.g., RWG) could not help explicit the solution. Thus, the point-matching method is used to solve the inverse equations. Finally, the approach proposed here assumes the following steps:

1. First, the electric fields on the surface of the upper hemisphere (in $z > 0$ space) are sampled when the antenna is located at a distance d above the lossy half-space (human tissue model).

2. Forming the MoM impedance matrice considering the observation points on the surface of the upper hemisphere and the source points on the antenna structure

3. Reconstruction of electric (J) equivalent currents on the antenna structure by inversely solving the matrix equation (4.44)

Table 4.1: The characteristics of the human skin model [112, 132].

f (GHz)	15	30	60
ε_r	27.27	16.6	9.1
σ (S/m)	14.24	27.3	37.96
δ (mm)	2	0.87	0.48

4. Evaluating the electric and magnetic field on the evaluation surface by directly solving the matrix equation (4.44) by considering the observation points on the evaluation surface and Current sources obtained in the previous step

5. Assessing the APD (1.14) by the electric and magnetic fields obtained in the previous step

4.2.1 Human skin model

The shallow field penetration at millimeter-wave frequencies allows us to model the human body as a homogeneous semi-infinite dielectric layer with the average of wet and dry skin properties. Thus, semi-infinite layer 2 is filled with an isotropic medium specified by $\varepsilon_0\varepsilon_r$ and μ_0, representing a lossy medium as a human skin equivalent, whose dielectric properties and conductivity are shown in Table 4.1 [112, 132]. A complete study around the dielectric properties assessment of biological tissues can be found in [133].

4.3 Validation

For validation purposes, a dipole antenna with a length of approximately $\lambda/2 \approx 4.28$ mm and a radius of approximately 0.3 mm has been simulated at a frequency of 30 GHz. The dipole antenna is positioned at a distance of $d = 1$ mm, which is approximately $\lambda/10$, from the lower half-space. The dipole antenna is assumed to be made of PEC. The lower half-space ($z \leq 0$) is modeled with the electrical and magnetic characteristics of human tissue, as determined in Section 4.2.1.

To reconstruct the equivalent currents, the electric fields on the upper hemisphere (in the $z > 0$ space) with a radius of $R = 5$ cm are sampled. In this problem, we assume that only electric currents are present on the antenna structure, and the magnetic currents are zero, as the PEC conditions are considered for the antenna structure. Therefore, the electric current distribution on the antenna structure, with 718 unknown points, has been obtained. The E-field is sampled at 741 points on the hemisphere's surface is evaluated using FEKO.

Figure 4.3 shows the amplitude of the electric current vector ($\overrightarrow{J} = J_x\hat{x} + J_y\hat{y} + J_z\hat{z}$) at each point. In the context of inverse problems, it should be noted that the reconstructed current serves as an approximation of the reference and may not resemble it exactly, given the infinite possible solutions inherent in these problems. However, the objective is to construct E- and H-fields using these reconstructed current with minimal errors.

The Table 4.2 provides the RMS (Root Mean Square) error of amplitude ($J_T = \sqrt{J_x^2 + J_y^2 + J_z^2}$) and the pattern similarity value (correlation coefficient) between the reconstructed and simulated currents. The determination of the RMS error is employed to quantify the average magnitude of errors between reconstructed and reference values. The formula for the $A_{m\times n}$ matrix is as follows

$$\text{RMS error} = \sqrt{\frac{\sum_{i=1}^{m\times n} |A^{rec} - A^{ref}|^2}{m \times n}}. \tag{4.45}$$

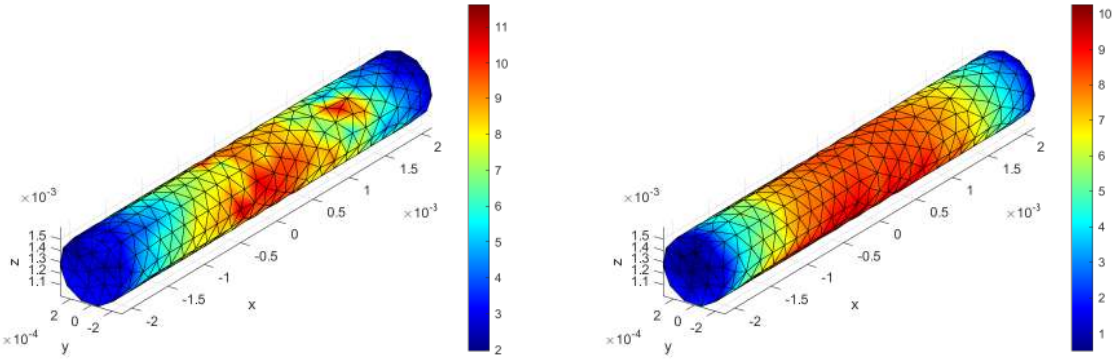

(a) (b)

Figure 4.3: The amplitude of electric currents (J_T) of the antenna (a) reconstructed (b) simulated by FEKO.

Table 4.2: RMS amplitude error and correlation coefficient of reconstructed and simulated current components

Current	RMS error	Correlation coefficient
J_T	62.8	0.92

In the next step, we use the reconstructed equivalent currents to calculate the electric and magnetic fields on the evaluation plane, which is the boundary between the air and the human tissue model. The evaluation plane has the following specifications: $-\lambda \leq x \leq \lambda$, $-\lambda \leq y \leq \lambda$, and $z = -1\mu$m. The fields are obtained using the matrix equation of dyadic Green functions.

Figure 4.4 shows the amplitude of the total electric field at each point on the evaluation plane, while Figure 4.5 shows the amplitude of the total magnetic field at each point. The table in Figure 4.3 provides the RMS error and the pattern similarity value (correlation coefficient) between the obtained fields and the fields obtained from the FEKO simulator.

Next, we calculate the distribution of the APD on the evaluation plane using the electric and magnetic fields obtained in the previous step. Figure 4.6 illustrates the amplitude of the real part of the APD at each point on the evaluation plane. Table 4.4 provides the RMS amplitude error and the correlation coefficient between the reconstructed and simulated APD.

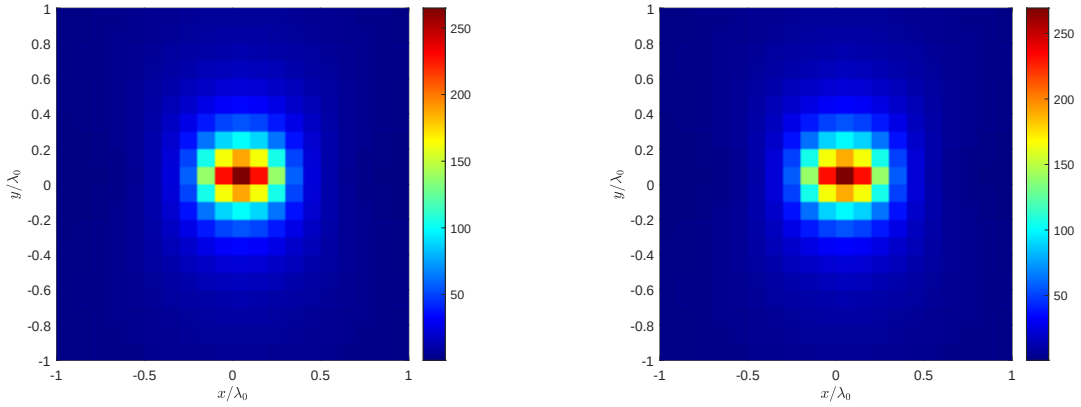

(a) (b)

Figure 4.4: Total electric field's amplitude: (a) reconstructed (b) simulated by FEKO.

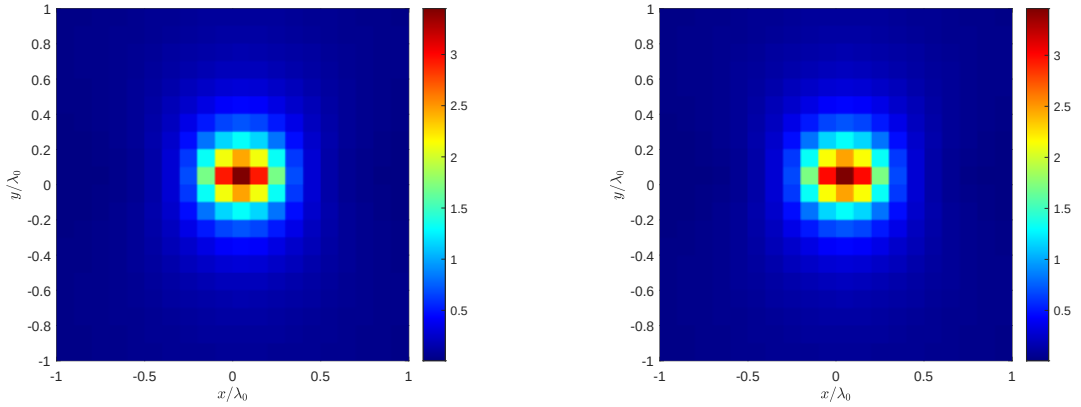

(a) (b)

Figure 4.5: Total magnetic field's amplitude: (a) reconstructed (b) simulated by FEKO..

Table 4.3: Amplitude RMS error and correlation coefficient of reconstructed and simulated electric field elements

Field	RMS error	Correlation coefficient
E_x	3.44	0.999
E_y	52.78	0.999
E_z	33.92	0.999
H_x	50.8	0.999
H_y	3.32	0.999
H_z	310.3	0.999

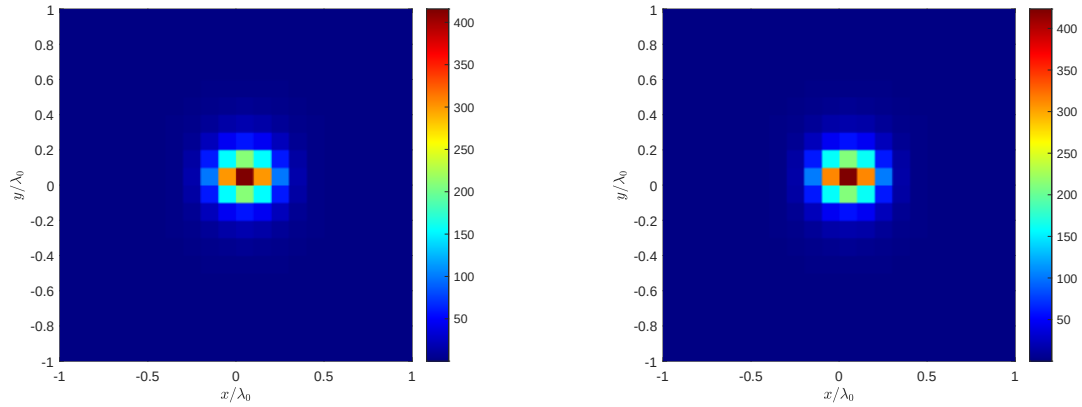

(a) (b)

Figure 4.6: The amplitude of the real part of the absorbed power density: (a) reconstructed (b) simulated by FEKO.

Table 4.4: Amplitude RMS error and correlation coefficient of reconstructed and simulated absorbed power density

APD	RMS error	Correlation coefficient
$PDz\{-\hat{z}\}$	3.04	0.999

Finally, we compare the maximum values of S_{4cm^2} obtained from the reconstruction and simulation methods. In the reconstruction method, the maximum value is determined as 3.3802 milliwatts per square meter, while in the simulation method, it is found to be 3.4466 milliwatts per square meter. The error rate between the two methods is approximately 1.927%. These results demonstrate the accuracy, applicability, and practicality of the proposed method.

In the following analysis, we aim to provide a comprehensive evaluation by considering different types of antennas, frequencies, and the effects of separation distance on the human tissue model.

4.4 Antennas' configurations

The selection of antennas in this analysis was based on their relevance to 5G mobile phone communications, specifically considering features such as MIMO and beamforming. Two different placements for the antenna array were considered: one on the edge and the other on the corner of the mobile phone. This configuration was inspired by antenna designs found in references [134, 135].

The frequencies chosen for the analysis were 15, 30, and 60 GHz, covering the frequency range above 6 GHz, which is significant for next-generation communication systems. The mobile phone's electrical circuit board, acting as a reflector, was modeled as a PEC plate. The dimensions of the PEC plate were assumed to be $W = 70$ mm and $L = 130$ mm.

The radiating elements were modeled as $\lambda/2$ PEC dipole arrays with a radius of 0.06λ,

where λ represents the wavelength in free space. The dimensions and configurations of the antennas, expressed in terms of λ, are shown in Figure 4.7. The red dots indicate the feeding ports of the antennas.

After optimization, the radiation patterns and return loss of the antennas in free space were obtained and are shown in Figure 4.8. The radiation patterns are normalized with respect to the desired frequency and the maximum gain value. The $\varphi = 0°$ and $\varphi = 90°$ planes are regarded as the H-plane and E-plane, respectively. It is worth noting that due to the symmetry of the antennas, the characteristics of the corresponding pairs in the edge and corner configurations are nearly identical. Therefore, only the return loss of port 1 (S_{11}) and port 2 (S_{22}) are shown in Figure 4.8.

For the worst-case scenario, the human body is exposed to the main beam of the antennas, simulating a realistic situation.

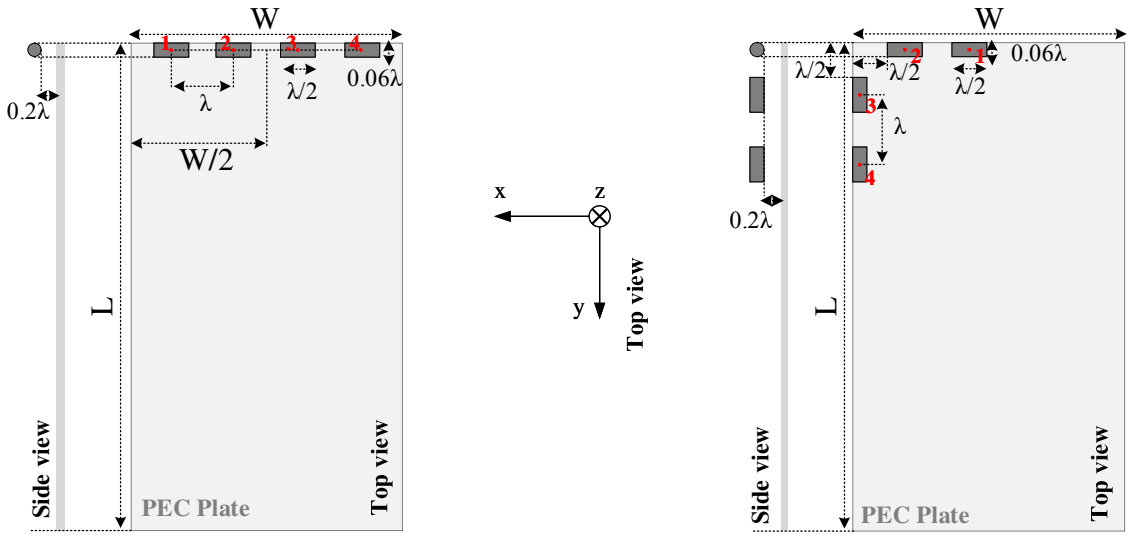

(a) (b)

Figure 4.7: Configuration and geometry of (a) egde-type, and (b) corner-type array antenna.

4.5 Results and discussion

In this analysis, the antennas are positioned above the human skin model, with the PEC plane parallel to the air-body interface, at different separation distances (d) in order to investigate the effectiveness of the proposed method. As the separation distance between

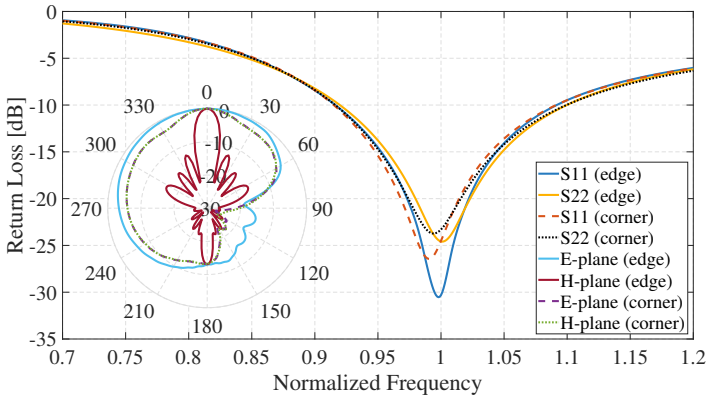

Figure 4.8: Return loss and the radiation pattern (E-plane and H-plane) of the antennas.

the antenna and the human skin model decreases, the interactions between the antenna and the body become more significant. Different separation distances are considered to study this effect. The separation distances, considered as $d = 1$, 2, 3, 4, 5, 10, and 20 mm, are defined as the normal distance between the phantom and the nearest part of the antenna. At each frequency, the distance between the PEC plane and the phantom can be regarded as $d + 0.26\lambda$.

The radius of the hemisphere (R), which is related to the dimensions of the antenna's reflector (70 mm $\times$ 130 mm) and the maximum separation distance between the Device Under Test (DUT) and the phantom ($d = 20$ mm), is chosen as 10 cm to fully encompass the DUT. As depicted in Figure 4.2, the center of the DUT is positioned on the z-axis. Consequently, the minimum separation distance between the DUT and the probes is estimated to be approximately 1.1λ, 2.3λ, and 4.7λ for frequencies of 15, 30, and 60 GHz, respectively. Thus, the probes are assumed to be in the radiative near-field of the DUT, in accordance with [136, 137, eq. (1)].

The reactive near-field region of a probe decreases as the probe size decreases, following the relationship $0.62\sqrt{D^3/\lambda}$ [136]. Consequently, a smaller probe can be positioned closer to the radiation source without significant coupling to the DUT. The EUmmWVx probe developed by the SPEAG team [72] is capable of measuring up to 2 mm in proximity to the radiating source at millimeter-wave frequencies, making it suitable for use in the proposed measurement system. This allows the probes to be positioned close enough to detect the evanescent wave while ensuring minimal impact on the radiation source.

It is important to note that a minimum probe-phantom distance of 2 mm is considered to ensure accurate measurements. This distance is chosen to maintain sufficient separation between the probe and the phantom while still capturing the desired field information accurately.

The reconstructed spatial averaged APD (S_A) includes some numerical errors. The reconstruction errors are calculated as follows:

$$\text{relative error } (\%) = \left[\frac{|\max[S_A^{Ref}] - \max[S_A^{Rec}]|}{\max[S_A^{Ref}]}\right] \times 100, \tag{4.46}$$

where $\max[S_A^{Rec}]$ and $\max[S_A^{Ref}]$ are the maximum S_A evaluated by the proposed method and the reference, respectively.

4.5.1 APD distribution

The effectiveness of the proposed method is assessed based on the reconstructed fields' absolute value, phase, and distribution on the evaluation plane. Figure 4.9 illustrates the reconstructed APD distributions at selected frequencies for separation distances of $d = 2$ mm and $d = 5$ mm. These reconstructed APD distributions are compared to the reference values obtained from FEKO, a commercial electromagnetic solver that utilizes the Method of Moments (MoM) [113].

To facilitate comparison, the reconstructed APD distributions are normalized with respect to the maximum value obtained from the corresponding reference data at each separation distance. This normalization allows for a relative evaluation of the accuracy and similarity between the reconstructed and reference APD distributions.

Figure 4.9 clearly illustrates the wider radiation pattern of the corner-type antenna compared to the edge-type antenna, as demonstrated in Figure 4.8. The reconstructed APD distributions exhibit a remarkable similarity to the reference distributions. The correlation coefficients between the reconstructed APD and the reference data exceed 94.77% for all cases.

It is worth noting that as the frequency increases from 15 GHz to 60 GHz, the separation distance d in terms of wavelength λ also increases. For instance, when $d =$ is 5 mm, this constant distance equates to $\lambda/4$ at 15 GHz and λ at 60 GHz. This amplified distance in terms of λ results in a weaker coupling between the antenna and the body. The diminished coupling contributes to enhanced accuracy in reconstructing the APD at higher frequencies and larger separation distances.

Overall, these results indicate the effectiveness and reliability of the proposed method in accurately reconstructing the APD distributions for different antenna types, frequencies, and separation distances.

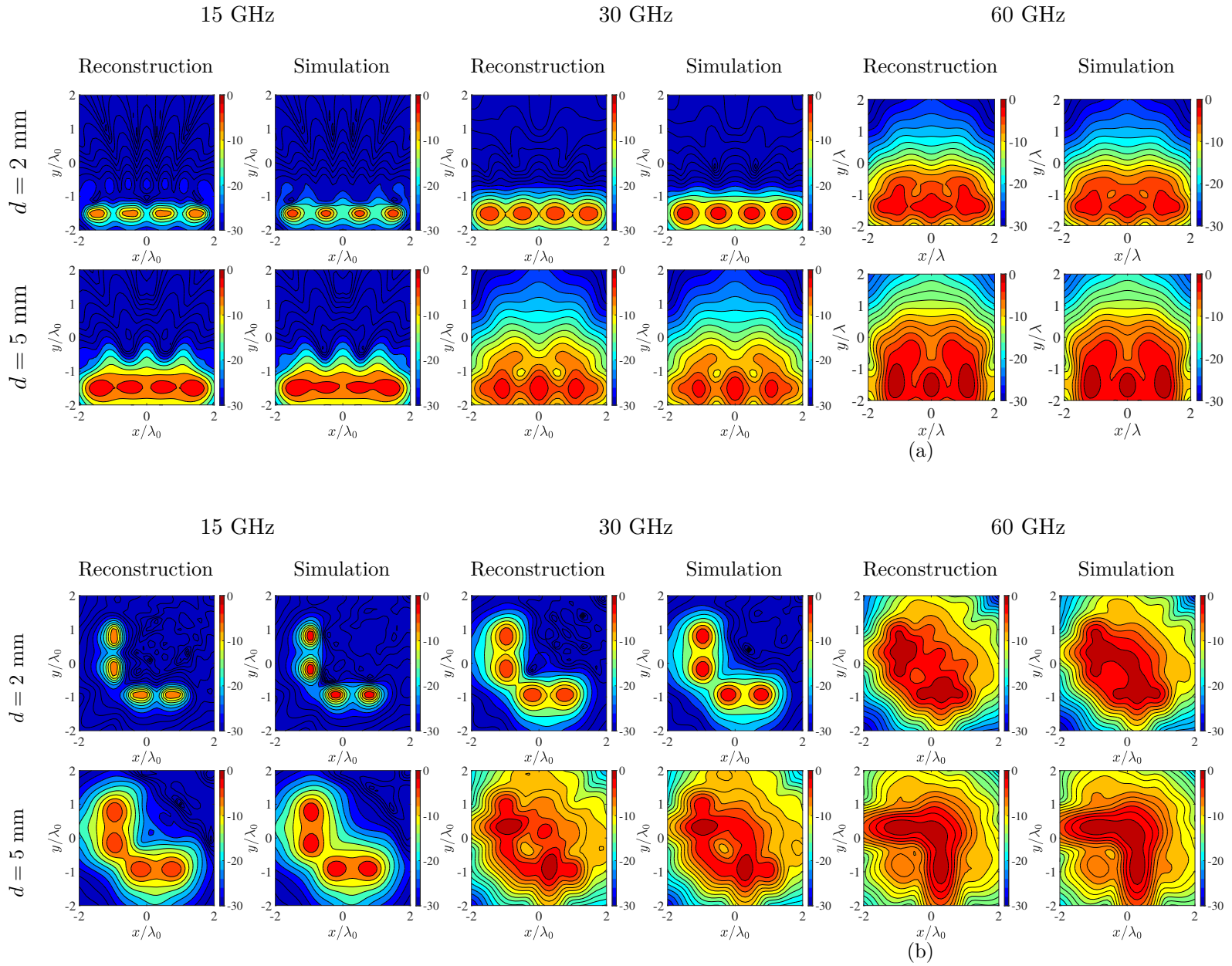

Figure 4.9: APD distribution [dB] of (a) edge-type and (b) corner-type antenna at 15, 30 and 60 GHz for $d = 2.5$ mm.

4.5.2 Maximum S_A

In Figure 4.10(a) and 4.11(a), the maximum values of S_{4cm^2} are shown for separation distances ranging from 1 mm to 20 mm at 15, 30, and 60 GHz for edge-type and corner-type antennas, respectively. The corresponding relative errors are presented in Figure 4.10(b) and 4.11(b). Additionally, the results for the maximum S_{1cm^2} and its error are depicted in Figure 4.12 and 4.13 for 30 and 60 GHz, considering edge-type and corner-type antennas.

The variations in the maximum S_A at separation distances $d < 5$ mm indicate the interactions between the antenna and the skin model. These interactions become more pronounced as the frequency decreases. Notably, in certain separation distances, the maximum S_A is higher compared to smaller separation distances, suggesting the occurrence of constructive and destructive interference between incident and reflected waves at specific distances.

These findings demonstrate the complex nature of antenna-skin model interactions and highlight the importance of considering separation distances and frequency effects when evaluating the maximum S_A values.

The comparison of maximum S_A values with the reference, along with the associated errors, reveals that the edge-type antenna exhibits lower errors compared to the corner-type antenna. This suggests that the radiated fields of the corner-type antenna are more concentrated in the sandwich area, which is located away from the probe positions.

Furthermore, the errors in maximum S_A decrease as the frequency increases and as the separation distance d increases. This highlights the influence of d (in terms of wavelength λ) on the strength of coupling between the antenna and the skin model. Decreasing d narrows the window through which the E-field exits the sandwich area between the antenna and the skin model. Consequently, certain portions of the E-field information necessary for accurate reconstruction of the equivalent currents do not reach the probes, leading to higher errors in the maximum S_A estimation.

At 15 GHz, the maximum errors in S_{4cm^2} are below 8.6% for the edge-type antenna at $d \geq 3$ mm, and below 10% for the corner-type antenna at $d \geq 8$ mm. At 30 GHz, the maximum errors in S_{4cm^2} and S_{1cm^2} are less than 7.4% and 8.3%, respectively, for the edge-type antenna at $d \geq 2$ mm. For the corner-type antenna, the errors are 3.6% at $d \geq 5$ mm for S_{4cm^2}, and 5.8% at $d \geq 4$ mm for S_{1cm^2}.

At 60 GHz, the maximum errors in SA are generally below 10%, except for S_{4cm^2} at $d = 1$ mm and S_{1cm^2} at $d = 1$ mm and 2 mm for the corner-type antenna, which have errors of 10.16% and 11.7%, respectively. These findings indicate that the accuracy of APD reconstruction is influenced by the antenna's configuration and radiation pattern. Antennas with radiation focused towards the external region of their internal structure, as desired for mobile phone antennas in future generations [138], exhibit higher accuracy in APD reconstruction.

Overall, the results suggest that the proposed approach is suitable for reconstructing APD at 5G millimeter-wave frequencies, particularly at higher frequencies.

4.5.3 Measurement requirements

For the reconstruction method to achieve acceptable accuracy, it is crucial to efficiently collect data by measuring E-field data that is both adequate and accurate. Additionally,

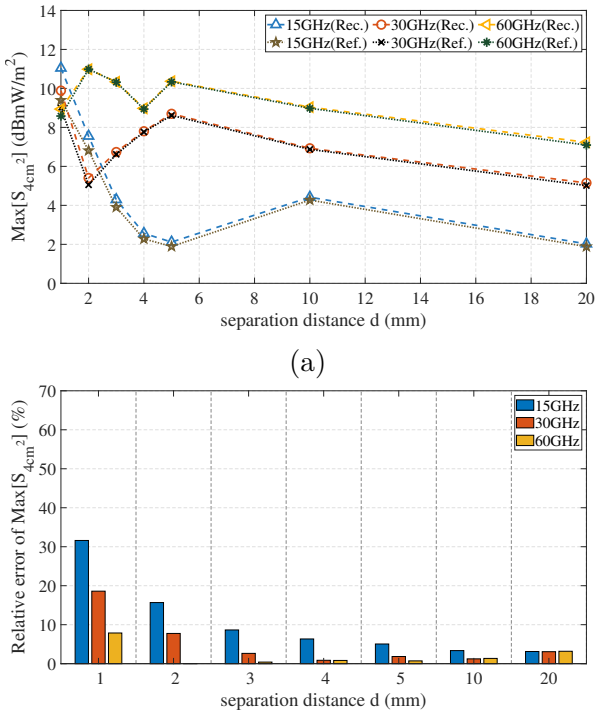

Figure 4.10: (a) Maximum S_{4cm^2} and its (b) relative error at 15, 30, and 60 GHz for the edge-type antenna.

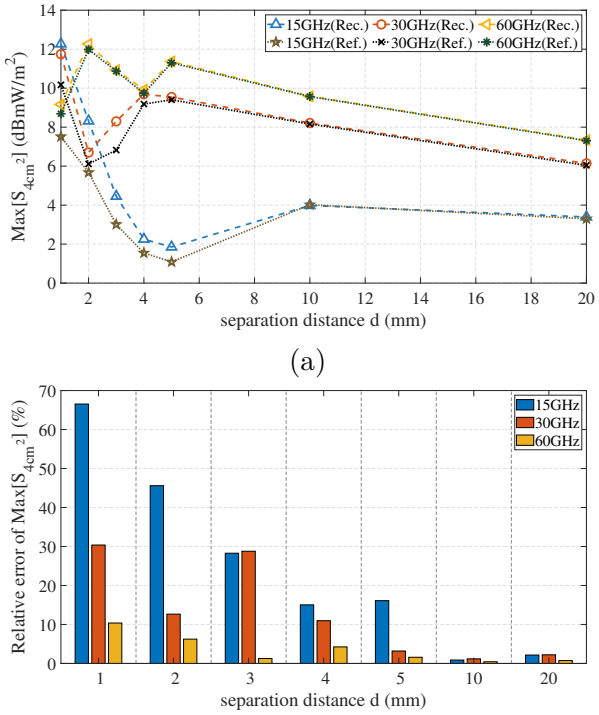

Figure 4.11: (a) Maximum S_{4cm^2} and its (b) relative error at 15, 30, and 60 GHz for the corner-type antenna.

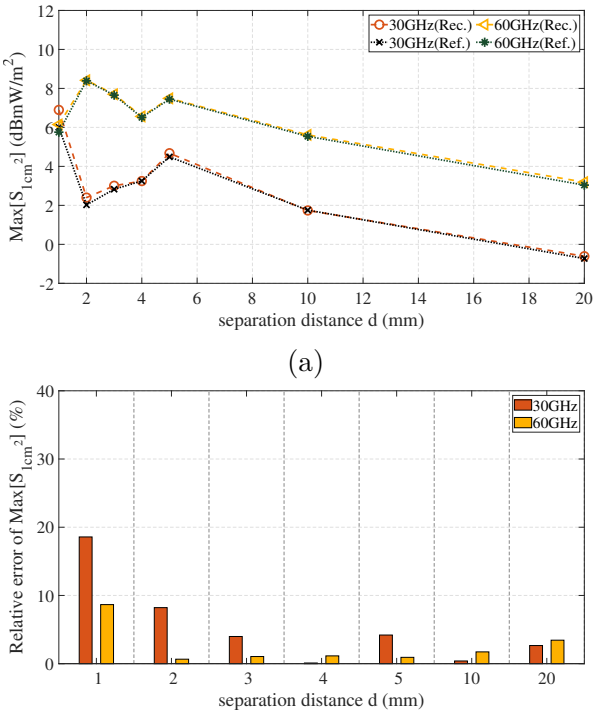

Figure 4.12: (a) Maximum S_{1cm^2} and its (b) relative error at 30 and 60 GHz for the edge-type antenna.

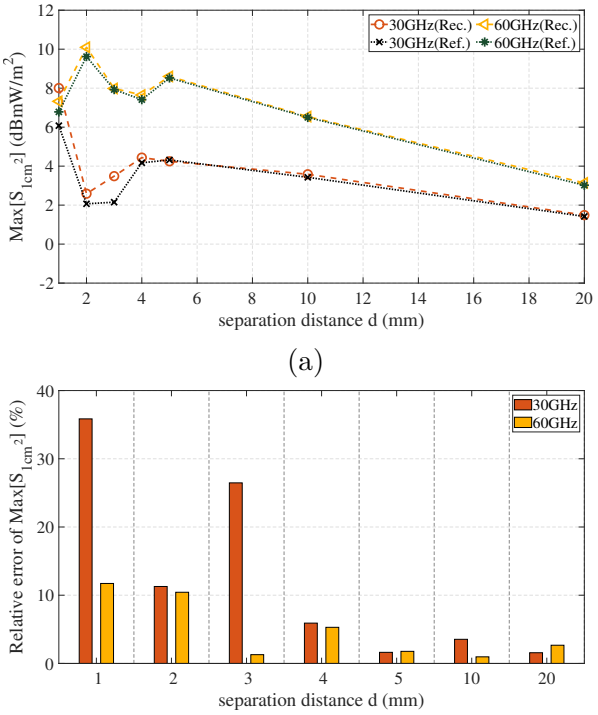

Figure 4.13: (a) Maximum S_{1cm^2} and its (b) relative error at 30 and 60 GHz for the corner-type antenna.

the size of the phantom employed in the measurement system can impact the E-fields on the surface of the hemisphere, potentially resulting in reduced accuracy. Consequently, the following aspects are investigated to assess their influence: the angular resolution of the sampled E-field, the uncertainty associated with the measured amplitude and phase of the E-field, and the sensitivity of the method to variations in phantom size.

4.5.3.1 Angular resolution

While dense sampling on the surface of the hemisphere can enhance reconstruction accuracy, it also leads to longer measurement times. Conversely, sparse sampling may result in poor accuracy. Therefore, to achieve an efficient system, the sampling interval should strike a balance between collecting sufficient information and minimizing measurement time. Consequently, the reconstruction error has been investigated for various angular intervals (Δ) of 2, 4, 6, and 8 degrees, considering both azimuth (ϕ) and elevation (θ) angles.

Figure 4.14 illustrates the relative error of maximum S_{4cm^2} and S_{1cm^2} for different angular intervals. It is worth noting that the errors for maximum S_{4cm^2} and S_{1cm^2} exhibit similar trends. Errors exceeding 100% indicate a lack of convergence in solving the inverse equation for reconstructing the equivalent current, suggesting the loss of critical information during sampling. As anticipated, the errors generally increase as the sampling interval, Δ, increases from 2° to 8°. The choice of acceptable sampling intervals depends on the radiation pattern of the Device Under Test (DUT). The results highlight that $\Delta \leq 2°$ provides more reliable information for both types of antennas.

4.5.3.2 Measurements uncertainty

Monte Carlo simulation is employed to assess the sensitivity of the reconstructed maximum S_A to the accuracy of the measured amplitude and phase. The impact of amplitude uncertainty is determined by introducing Gaussian noise (e^{error}) with standard deviations of -20 dB and -30 dB relative to the peak value on the surface of the hemisphere. Phase uncertainty is taken into account by introducing a phase error (φ^{error}) as a random variable with a normal distribution and a standard deviation of σ, which is added to the measured E-fields. The expression for incorporating the phase error is given by:

$$|E|^{MC}(x,y,z) = |E|^{sim}(x,y,z) + e^{error}(\sigma_a), \tag{4.47}$$

$$\measuredangle E^{MC}(x,y,z) = \measuredangle E^{sim}(x,y,z) + \varphi^{error}(\sigma_p), \tag{4.48}$$

where $\measuredangle E$ and $|E|$ are the amplitude and phase of the E-field, the superscript of MC and sim are corresponded to the uncertain and certain parameters on the hemisphere's surface, respectively. For each combination of amplitude and phase uncertainty, 500 simulations were conducted to analyze the effect of noises on the APD reconstruction accuracy.

The mean contribution error of the reconstructed maximum S_A, resulting from amplitude noise levels of -20 dB and -30 dB, is found to be no larger than 1.27% and 0.17%, respectively, for $A = 1$ cm^2 at 30 GHz, and 4.13% and 2.38% for $A = 4$ cm^2 at 15 GHz. These results indicate that the impact of amplitude uncertainty on the reconstructed maximum S_A is relatively small.

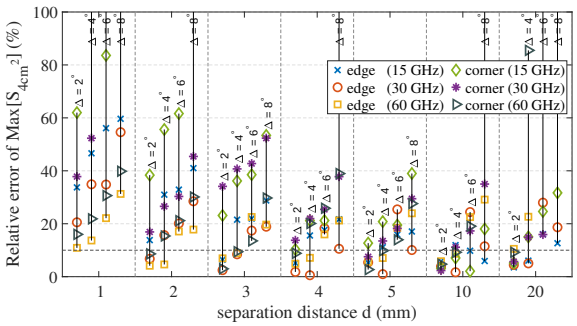

(a)

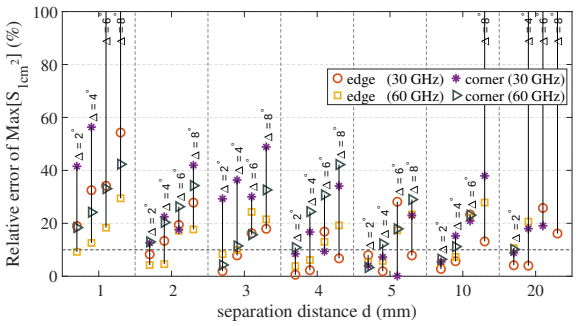

(b)

Figure 4.14: Relative error of maximum S_A with (a) $A = 4$ cm^2 at 15, 30, and 60 GHz and (b) $A = 1$ cm^2 at 30, and 60 GHz due to the angular intervals $\Delta = \Delta\phi = \Delta\theta$ of 2°, 4°, 6°, and 8°.

The contribution errors of the reconstructed maximum S_{1cm^2}, solely due to the amplitude noise level of -20 dB, are presented in Figure 4.15(a). The bars represent the mean contribution errors, while the lines represent the ranges of errors. It can be observed that the contribution errors remain within an acceptable range, indicating that the reconstructed maximum S_{1cm^2} is less affected by amplitude uncertainty.

Furthermore, the combined effect of amplitude noise (-20 dB) and phase noise is evaluated by assessing the contribution error of the reconstructed maximum S_A. The maximum mean contribution errors of 2.65%, 5.41%, and 6.35% are obtained for $A = 1$ cm^2 at 30 GHz, and 5.16%, 8.13%, and 9.91% for $A = 4$ cm^2 at 15 GHz, with phase standard deviations of $\sigma_p = 5°$, 10°, and 20°, respectively. These errors occur at the minimum separation distance between the antenna and the skin model, as depicted in Figure 4.15(b).

Overall, the results indicate that the reconstruction method is robust against amplitude noise, while the combination of amplitude and phase noise can introduce some level of error, particularly at smaller separation distances.

The results presented in Figure 4.15 illustrate the average contribution error for both edge-type and corner-type antennas. Based on these results, it is recommended to ensure that the phase measurement error does not exceed 10 degrees and the amplitude measurement error remains below -20 dB (relative to the peak value) in order to maintain the accuracy of the reconstruction method with a 90% confidence level.

By keeping the phase measurement error within 10 degrees, the impact of phase uncertainty on the reconstructed results can be effectively controlled. This ensures that the reconstructed maximum S_A remains reliable and accurate, as the contribution error

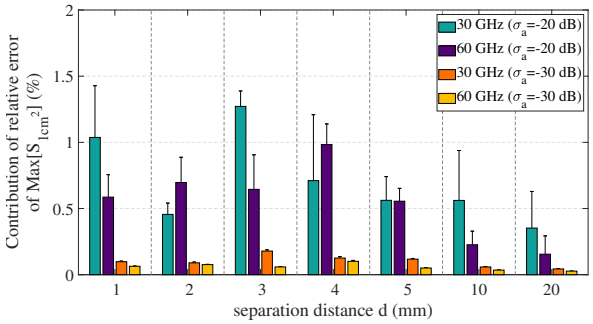

(a)

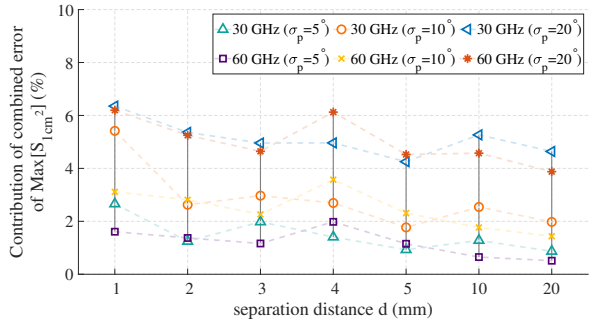

(b)

Figure 4.15: Contribution error of maximum S_{1cm^2} (a) due to the amplitude noise of -20 dB from the peak value and (b) combined with the phase error of 5°, 10°, and 20° at 30 and 60 GHz.

introduced by phase uncertainty is limited.

Similarly, limiting the amplitude measurement error to -20 dB (relative to the peak value) helps maintain the accuracy of the reconstructed results. By controlling the amplitude uncertainty within this range, the contribution error associated with amplitude measurement can be kept at an acceptable level, providing reliable reconstructed values for maximum S_A.

Adhering to these recommended thresholds for phase and amplitude measurements allows for the preservation of the reconstruction accuracy within a 90% confidence level. It is important to note that these thresholds may vary depending on specific requirements and applications, and additional considerations may be necessary to further improve the accuracy of the reconstruction method.

4.5.3.3 Semi-infinite layered approximation

The reconstruction errors of S_A^{Ref} were assessed based on the assumption of an infinite phantom surface and a phantom depth of 10λ. However, it is important to note that this semi-infinite layered phantom assumption is not applicable in practical laboratory environments. Therefore, clear instructions should be provided for specifying the dimensions of the substitute phantom. The size of the phantom depends on factors such as the radiation pattern of the antenna and the separation distance (d) between the antenna and the phantom.

Considering the phantom as a cube, the thickness of the phantom should be determined

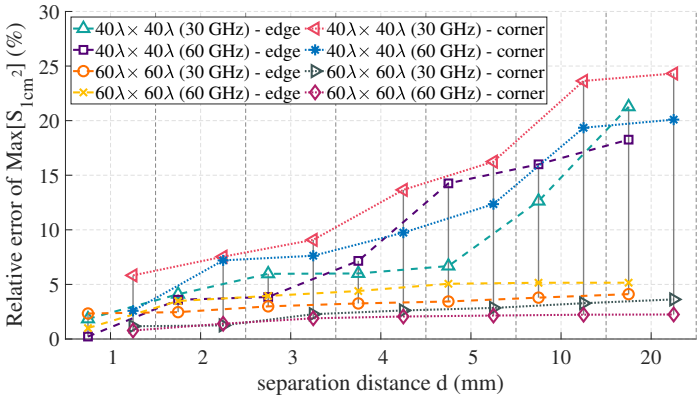

Figure 4.16: Relative error of maximum S_{1cm^2} due to the phantom surface size with λ thickness at 30 and 60 GHz.

based on the field's penetration depth. The penetration depth is defined as the distance at which the amplitude of a plane wave decreases to 63.2% of its initial value at the interface. The penetration depths at 15, 30, and 60 GHz, corresponding to the specific dielectric characteristics, are presented in Table 4.1. These values were calculated using the following formula, as described in [128]:

$$\delta(m) = \frac{1}{\alpha} = \frac{1}{\omega\sqrt{\mu\varepsilon}\left(\frac{1}{2}[\sqrt{1+(\sigma/\omega\varepsilon)^2}-1]\right)^{1/2}}, \tag{4.49}$$

where δ is penetration or skin depth, α is attenuation constant (Np/m), ω is angular frequency (rad/s), ϵ, σ, μ are permittivity (F/m), conductivity (S/m), and permeability (H/m) of the medium, respectively.

The thickness of the phantom should be considered in such a way that the field attenuates to zero after passing through the thickness of the phantom. To this end, the thickness of the phantom is considered at least five times bigger than the penetration depth to ensure the fields vanish in the lossy phantom. Also, the phantom surface should be large enough to avoid the effect of the diffraction from edges on the measured field at the hemisphere's surface. Accordingly, The analysis is performed to study the sensitivity of maximum S_A to the semi-infinite layered assumption of the phantom by considering the surface size of the phantom as $40\lambda \times 40\lambda$ and $60\lambda \times 60\lambda$ and the depth as $\lambda/2$ and λ. The errors related to the maximum S_{1cm^2} due to the phantom size are shown in Figure 4.16.

Reconstructed APD was compared to the APD computed with CST Microwave Studio, a commercial electromagnetic solver based on finite integration technique (FIT) [139]. The reconstruction error remains almost constant with respect to thickness changes from 0.5λ to λ. Therefore, in Figure 4.16, the relative error of reconstruction is shown with a phantom thickness of λ. On the other hand, changes in the size of the phantom surface are effective on the reconstruction error.

Considering $40\lambda \times 40\lambda$ as the phantom surface, when the separation distance is small, the reconstruction error is acceptable, but as the separation distance increases, the greater the effect of diffraction from the phantom edge on the sampling field. As a result, the reconstruction error is drastically increased at $d = 20$ mm. As the size of $60\lambda \times 60\lambda$ is selected, the diffraction effect can be negligible even at a larger separation distance. The

relative errors of maximum S_{1cm^2} were found within ± 10 % for $60\lambda \times 60\lambda$. As expected, the corner-type antenna is more sensitive to the phantom size compared to the edge-type one. Thus, considering the phantom dimensions larger than $60\lambda \times 60\lambda \times \lambda$ guarantees an acceptable result.

Chapter 5

Conclusion and future works

In the first chapter, a comprehensive overview of the international safety standards and guidelines for safeguarding human health against electromagnetic field propagation was provided. This review highlighted the potential risks to human well-being, explored the intricate interactions between electromagnetic fields and the human body, and delved into the various parameters employed to measure and assess near-field electromagnetic exposure. Additionally, the chapter emphasized the importance of the APD as an essential criterion for evaluating exposure levels, particularly for frequencies exceeding 6 GHz.

To accurately assess the APD, it is crucial to consider real-world scenarios where the DUT is in close proximity to the human body. Therefore, the evaluation of APD should be conducted under conditions that replicate the presence of the human body in the measurement laboratory. This entails placing a human body model in close proximity to the DUT and subsequently evaluating the APD. However, due to the near-field nature of the interaction between the antenna and the phantom, the spatial dependence of the E- and H-fields cannot be adequately described analytically.

The situation becomes further complicated when considering the coupling and multiple reflections that occur between the antenna and the human body. The radiation fields emitted by the antenna bounce back and forth between the antenna and the human body, leading to alterations in the antenna's current distribution. Consequently, these changes in the source's current result in modifications to the incident fields. Therefore, accurately characterizing the APD in such scenarios requires taking into account the complex interplay between the antenna, the human body, and the resulting field interactions.

To evaluate the APD on the human skin surface, two methods have been chosen: the Plane-Wave Spectrum (PWS) method and the Source Reconstruction Method (SRM) or Equivalent Current Reconstruction (EQC) method. These methods are selected due to their ability to consider the field and its impact in any medium.

The PWS method involves reconstructing the field by measuring it inside a human skin tissue model. This approach allows for the assessment of APD by analyzing the field distribution within the simulated skin tissue.

On the other hand, the EQC method involves reconstructing the field by measuring it outside of the phantom on a hemispherical surface surrounding the antenna. This method enables the evaluation of APD by examining the field characteristics in the vicinity of the antenna.

By employing these two different approaches, the APD can be assessed from different

perspectives, providing a comprehensive understanding of the field exposure on the human skin surface. Both methods offer valuable insights into the distribution and impact of the electromagnetic field, contributing to a more thorough evaluation of APD.

5.1 Invasive APD assessment

A novel approach has been introduced to evaluate the APD from measurements conducted inside a human tissue model when the antenna is placed in close proximity to the human body, specifically for frequencies above 6 GHz. Previous studies typically relied on the free space scenario, where the antenna operated without the presence of a human body model, to evaluate the APD using the plane wave transmission coefficient in the spectral domain or to assess the IPD.

In the proposed method, the electric field inside the human skin tissue model is sampled at a specific distance from the skin surface. By employing the backward propagating PWS method, the APD beneath the skin surface is determined. To assess the accuracy of this approach, a comparison is made between the proposed method, the PWS method in free space, and full wave simulations as a reference.

The results demonstrate that the APD reconstruction error for distances greater than 1 mm between the antenna and the human body model is approximately 9.4%, 7.35%, and 7.8% at frequencies of 10, 24, and 60 GHz, respectively. Moreover, it is observed that the effects of coupling and multiple reflections between the antenna and the human body model diminish when the distance between them exceeds one wavelength.

The sampling plane inside the human tissue model for the electric field measurements is considered to be 4.8 cm $\times$ 4.8 cm (9 $\times$ 9 points), 2 cm $\times$ 2 cm (9 $\times$ 9 points), and 1 cm $\times$ 1 cm (6 $\times$ 6 points) with spatial steps of 6, 2.5, and 2 mm at 10, 24, and 60 GHz, respectively. The misalignment error between the center of the antenna and the sampling plane, which indicates the spatial error of the sampling plane, is also investigated. Additionally, the amplitude of the electric field in the sampling plane inside the human tissue model is examined in terms of the detection capability of the measurement probe and the practical applicability of the proposed method. At 60 GHz, the maximum error of the minimum detection limit of 0.5, 0.8, 1, and 2 V/m for evaluating the APD is found to be 0.15%, 0.31%, 0.58%, and 1.69%, respectively. This error decreases with increasing distance between the antenna and the human body model, particularly at distances greater than one wavelength, as the antenna pattern expands, resulting in a higher minimum amplitude of the electric field in the sampling plane.

Phase uncertainty is taken into account by introducing a phase error to the sampled electric field. For the sampling plane located at a distance of 2 mm inside the tissue, the average combined error of the minimum detection limit of 1 V/m and phase errors with standard deviations of 5, 10, and 20 degrees at 60 GHz is determined to be 1.05%, 1.13%, and 4.63%, respectively.

The results validate the proposed method, involving measurements conducted inside the human tissue model and utilizing the backward-propagation PWS reconstruction method, as an efficient and accurate approach for evaluating the APD while considering the effects of coupling and multiple reflections. Compared to the PWS method in free space, the proposed method offers advantages in terms of time and computational efficiency due to the smaller size of the sampling plane. This research provides valuable

insights for evaluating the APD in next-generation wireless telecommunications and establishing EMF compliance testing methods for products operating in these frequency bands.

5.1.1 Future works

In future works, the following aspects can be considered to further enhance the APD evaluation method:

1. Investigating the frequency limitation: As mentioned, the method may face limitations at frequencies higher than 60 GHz due to the reduced depth of field penetration. Further research can focus on understanding and addressing these limitations to extend the applicability of the method to higher frequency ranges.

2. Incorporating skin surface roughness: To approach the actual amount of radiation exposure, considering the non-smooth surface of the human skin model can be valuable. This can be achieved by implementing a randomly rough surface on the air-phantom boundary, simulating the realistic surface characteristics of human skin. By accounting for surface roughness, the method can provide more accurate and realistic results.

3. Exploring different antennas: Using different antennas with varying beam patterns can provide a broader view of the radiation exposure. It would be beneficial to consider a range of antennas, including those commonly used in practical scenarios, to account for the variations in radiation patterns and characteristics. This approach would enhance the generalizability and practicality of the APD evaluation method.

4. Developing a detailed model of the mobile phone: To further improve the accuracy of the APD evaluation, future works can focus on creating a more comprehensive model of the mobile phone. This would involve considering not only the antenna but also the passive and active components on the main board, as well as other components such as the LCD and battery. By including these elements, the evaluation method can better reflect real-world scenarios and provide more accurate results.

By addressing these considerations in future research, the APD evaluation method can be enhanced, leading to improved understanding and assessment of radiation exposure in various frequency ranges and practical scenarios.

5.2 Non-invasive APD assessment

In this part of the thesis, a novel technique based on the DGF is proposed for reconstructing the equivalent source current when the antenna is positioned above the lossy half-space (phantom) for non-invasive APD evaluation, considering antenna-body coupling. The methodology involves dividing the entire space into two half-spaces: the upper half-space ($z > 0$) filled with air, where the antenna is located, and the lower half-space filled with an equivalent human skin liquid/solid. The required data for reconstructing

the equivalent source current is obtained by sampling the electric fields on the surface of a hemisphere surrounding the antenna within the upper half-space.

The proposed reconstruction method is solved using the MoM. Numerical simulations have been conducted to demonstrate the effectiveness and validity of the approach using two types of antennas positioned above a semi-infinite human skin model. The reconstructed APD obtained from the proposed method exhibits good correspondence with the reference values. The reconstruction errors were found to be less than 8.6% ($d \geq 3$ mm), 7.4% ($d \geq 2$ mm), and 8.75% ($d \geq 1$ mm) for the edge-type antenna, and 27.8% ($d \geq 3$ mm), 11.66% ($d \geq 2$ mm, except for $d = 3$ mm), and 11.1% ($d \geq 1$ mm) for the corner-type antenna at frequencies of 15, 30, and 60 GHz, respectively, considering the maximum value between S_{4cm^2} and S_{1cm^2}.

It is observed that at separation distances of less than 5 mm, the effects of coupling and successive reflections become significant. However, as the separation distance increases, these effects gradually diminish. Therefore, it can be concluded that increasing the distance between the antenna and the human body leads to a reduction in the impact of coupling and reflections.

The measurement requirements for assessing APD, including angular resolution, E-field phase, amplitude uncertainty, and phantom size, were thoroughly investigated. It was determined that an angular resolution of $\Delta \leq 2^\circ$ is acceptable to ensure sufficient information for accurate reconstruction. The uncertainties in E-field amplitude and phase were evaluated by adding Gaussian noise with levels of -20 and -30 dB from the sampled peak value, along with standard deviations of 5, 10, and 20 degrees, respectively. The combined mean error of maximum S_{1cm^2} was found to be within 11.3%, 5.6%, and 3.4% at frequencies of 15, 30, and 60 GHz, respectively.

Additionally, the size of the phantom needed to satisfy the semi-infinite layer approximation had to be determined. Surface dimensions of $40\lambda \times 40\lambda$ and $60\lambda \times 60\lambda$ were considered, with a thickness of $\lambda/2$ and λ, respectively, to determine the required phantom size. The results showed that a phantom size of $60\lambda \times 60\lambda \times \lambda$ adequately meets the practical measurement needs.

The proposed method proves to be a promising candidate for assessing APD, taking into account the coupling between the human body and the antenna, particularly for EMF exposure compliance testing from 5G mmWave mobile handsets. It is expected that this method will contribute to standardization efforts within IEC TC 106.

In conclusion, the proposed method introduces a new methodology for assessing APD in human exposure from mobile phone devices operating at frequencies above 6 GHz, while considering the antenna-human body coupling. This advancement has the potential to significantly impact the field and can pave the way for improved standards and compliance testing.

5.2.1 Future works

Certainly, the proposed method can be further enhanced and extended to address various aspects and scenarios. Some potential directions for future works include:

1. Improving the accuracy of the proposed method for frequencies below the mm-wave range, allowing for a wider frequency applicability and assessment of APD in lower frequency bands.

2. Extending the method to incorporate multi-layer models of the human body, enabling the evaluation of APD and even SAR assessment for frequencies below 6 GHz. This extension can build upon existing research efforts such as [88, 99, 140].

3. Considering the non-smooth surface of human skin in APD calculations, as the actual human skin surface is not perfectly smooth. This consideration can lead to more realistic and accurate assessments of APD in real-life scenarios.

4. Optimizing the positioning of E-field probes and reducing the number of required samples based on the radiation beam characteristics of the antenna. This optimization can help streamline the measurement process and reduce resource requirements while maintaining accurate APD assessment.

5. Exploring different types of antennas, such as patch antennas, and developing more detailed models of mobile phones that encompass passive and active components, LCDs, batteries, and other relevant components. This expansion can provide a comprehensive view of APD evaluation in practical mobile phone scenarios.

6. Applying the proposed method to other applications, such as antenna diagnosis or near-to-far-field transformation for antennas located close to or inside a dielectric object [141–143]. This utilization of the method in different contexts can broaden its scope and utility in the field of antenna engineering and characterization.

By addressing these aspects, further advancements can be made in APD evaluation methodologies, contributing to the development of accurate and efficient techniques for assessing human exposure to electromagnetic fields in various scenarios.

Bibliography

[1] M. Simkó and M. O. Mattsson, 5G Wireless Communication and Health EffectsA Pragmatic Review Based on Available Studies Regarding 6 to 100 GHz *Int J Environ Res Public Health*, vol. 16, p. 3406, sep 2019.

[2] W. H. O. Radiation, E. Health, and W. H. Organization, *Establishing a dialogue on risks from electromagnetic fields*. World Health Organization, 2002.

[3] W. Xiang, K. Zheng, and X. S. Shen, *5G mobile communications*. Springer, 2016.

[4] I. Nasim, Analysis of Human EMF Exposure in 5G Cellular Systems Master's thesis, Electronic Theses and Dissertations (1923), 2019.

[5] C. A. Balanis, *Advanced engineering electromagnetics, 2nd Edition*. John Wiley & Sons, 2012.

[6] ICNIRP. Guidelines for limiting exposure to electromagnetic fields (100 kHz to 300 GHz) *Health Phys*, vol. 118, pp. 483–524, May 2020.

[7] IEEE Standard for Safety Levels with Respect to Human Exposure to Electric, Magnetic, and Electromagnetic Fields, 0 Hz to 300 GHz *IEEE Std C95.1-2019 (Revision of IEEE Std C95.1-2005/ Incorporates IEEE Std C95.1-2019/Cor 1-2019)*, pp. 1–312, Feb. 2019.

[8] R. E. Fields, Evaluating compliance with FCC guidelines for human exposure to radiofrequency electromagnetic fields *OET bulletin*, vol. 65, no. 10, 1997.

[9] IEEE Standard for Safety Levels with Respect to Human Exposure to Radio Frequency Electromagnetic Fields, 3 kHz to 300 GHz *IEEE Std C95.1-2005 (Revision of IEEE Std C95.1-1991)*, Oct. 2005.

[10] IEEE Standard for Safety Levels With Respect to Human Exposure to Human Exposure to Electromagnetic Fields, 03 kHz *IEEE Standard C95.6-2002*, Sep. 2002.

[11] ICNIRP. Guidelines for limiting exposure to time-varying electric, magnetic, and electromagnetic fields (up to 300 GHz) *Health Phys*, vol. 74, p. 494522, Apr. 1998.

[12] ICNIRP. Guidelines for limiting exposure to time-varying electric and magnetic fields (1 Hz to 100 kHz) *Health Phys*, vol. 99, no. 6, p. 818836, 2010.

[13] J. Wiart, *Radio-frequency human exposure assessment: from deterministic to stochastic methods*. John Wiley & Sons, 2016.

[14] FCC, Code of Federal Regulation Title 47, Section 1.1310, Radio Frequency Radiation Exposure Limits *FCC, Washington, DC, USA*, 1996.

[15] "FCC. (Oct. 2018). RF exposure procedures." https://transition.fcc.gov/oet/ea/presentations/files/oct18/5.2-RF_Exposure_Procedures-JN.PDF.

[16] "FCC. (Nov. 2019). RF exposure procedures." https://docs.fcc.gov/public/attachments/FCC-19-126A1.pdf.

[17] Resolution of Notice of Inquiry, Second Report and Order, Notice of Proposed Rulemaking, and Memorandum Opinion and Order *document FCC*, pp. 19–126, Dec. 2019.

[18] W. He, B. Xu, Y. Yao, D. Colombi, Z. Ying, and S. He, Implications of Incident Power Density Limits on Power and EIRP Levels of 5G Millimeter-Wave User Equipment *IEEE Access*, vol. 8, pp. 148214–148225, 2020.

[19] C. A. Balanis, *Antenna Theory: Analysis and Design, 4th Edition*. Wiley, 2016.

[20] R. C. Johnson, H. A. Ecker, and J. S. Hollis, Determination of far-field antenna patterns from near-field measurements *Proceedings of the IEEE*, vol. 61, no. 12, pp. 1668–1694, 1973.

[21] A. Yaghjian, An overview of near-field antenna measurements *IEEE Transactions on Antennas and Propagation*, vol. 34, no. 1, pp. 30–45, 1986.

[22] Y. Rahmat-Samii, L. I. Williams, and R. G. Yaccarino, The UCLA bi-polar planar-near-field antenna-measurement and diagnostics range *IEEE Antennas and Propagation Magazine*, vol. 37, no. 6, pp. 16–35, 1995.

[23] L. I. Williams, Y. Rahmat-Samii, and R. G. Yaccarino, The bi-polar planar near-field measurement technique, Part I: implementation and measurement comparisons *IEEE transactions on antennas and propagation*, vol. 42, no. 2, pp. 184–195, 1994.

[24] R. Yaccarino, Y. Rahmat-Samii, and L. Williams, The bi-polar planar near-field measurement technique, part II: near-field to far-field transformation and holographic imaging methods *IEEE Transactions on Antennas and Propagation*, vol. 42, no. 2, pp. 196–204, 1994.

[25] J. Lord, G. Cook, and A. Anderson, Reconstruction of the excitation of an array antenna from the measured near-field intensity using phase retrieval in *IEE Proceedings H-Microwaves, Antennas and Propagation*, vol. 139, pp. 392–396, IET, 1992.

[26] J. Lee, E. M. Ferren, D. P. Woollen, and K. M. Lee, Near-field probe used as a diagnostic tool to locate defective elements in an array antenna *IEEE Transactions on Antennas and Propagation*, vol. 36, no. 6, pp. 884–889, 1988.

[27] Y. Rahmat-Samii and J. Lemanczyk, Application of spherical near-field measurements to microwave holographic diagnosis of antennas *IEEE Transactions on Antennas and Propagation*, vol. 36, no. 6, pp. 869–878, 1988.

[28] M. S. Gatti and Y. Rahmat-Samii, FFT applications to plane-polar near-field antenna measurements *IEEE Transactions on Antennas and propagation*, vol. 36, no. 6, pp. 781–791, 1988.

[29] Y. Rahmat-Samii, Surface diagnosis of large reflector antennas using microwave holographic metrology: An iterative approach *Radio Science*, vol. 19, no. 05, pp. 1205–1217, 1984.

[30] A. Taaghol and T. K. Sarkar, Near-field to near/far-field transformation for arbitrary near-field geometry, utilizing an equivalent magnetic current *IEEE Transactions on Electromagnetic Compatibility*, vol. 38, no. 3, pp. 536–542, 1996.

[31] T. K. Sarkar and A. Taaghol, Near-field to near/far-field transformation for arbitrary near-field geometry utilizing an equivalent electric current and MoM *IEEE Transactions on Antennas and Propagation*, vol. 47, no. 3, pp. 566–573, 1999.

[32] P. Petre and T. K. Sarkar, A planar near-field to far-field transformation using an equivalent magnetic current approach in *IEEE Antennas and Propagation Society International Symposium 1992 Digest*, pp. 1534–1537, IEEE, 1992.

[33] Y. Álvarez, F. Las-Heras, and M. R. Pino, Reconstruction of equivalent currents distribution over arbitrary three-dimensional surfaces based on integral equation algorithms *IEEE Transactions on Antennas and Propagation*, vol. 55, no. 12, pp. 3460–3468, 2007.

[34] J. L. A. Quijano, L. Scialacqua, J. Zackrisson, L. J. Foged, M. Sabbadini, and G. Vecchi, Suppression of undesired radiated fields based on equivalent currents reconstruction from measured data *IEEE Antennas and Wireless Propagation Letters*, vol. 10, pp. 314–317, 2011.

[35] K. Persson, M. Gustafsson, G. Kristensson, and B. Widenberg, Source reconstruction by far-field data for imaging of defects in frequency selective radomes *IEEE Antennas and Wireless Propagation Letters*, vol. 12, pp. 480–483, 2013.

[36] L. Foged, L. Scialacqua, F. Saccardi, J. A. Quijano, and G. Vecchi, Application of the dual-equation equivalent-current reconstruction to electrically large structures by fast multipole method enhancement [AMTA corner] *IEEE Antennas and Propagation Magazine*, vol. 56, no. 5, pp. 264–273, 2014.

[37] K. Persson, M. Gustafsson, G. Kristensson, and B. Widenberg, Radome diagnosticsSource reconstruction of phase objects with an equivalent currents approach *IEEE Transactions on Antennas and Propagation*, vol. 62, no. 4, pp. 2041–2051, 2014.

[38] P. Li and L. J. Jiang, Source reconstruction method-based radiated emission characterization for PCBs *IEEE Transactions on Electromagnetic Compatibility*, vol. 55, no. 5, pp. 933–940, 2013.

[39] S. Pfeifer, E. Carrasco, P. Crespo-Valero, E. Neufeld, S. Kühn, T. Samaras, A. Christ, M. H. Capstick, and N. Kuster, Total Field Reconstruction in the Near Field Using Pseudo-Vector *E*-Field Measurements *IEEE Transactions on Electromagnetic Compatibility*, vol. 61, no. 2, pp. 476–486, 2019.

[40] P. Noren, L. J. Foged, L. Scialacqua, and A. Scannavini, Measurement and Diagnostics of Millimeter Waves 5G Enabled Devices in *2018 IEEE Conference on Antenna Measurements Applications (CAMA)*, pp. 1–4, 2018.

[41] M. Nesterova and S. Nicol, Analytical study of 5G beamforming in the reactive near-field zone in *12th European Conference on Antennas and Propagation (EuCAP 2018)*, pp. 1–5, 2018.

[42] B. Derat, A. Cozza, and J. Bolomey, Influence of source - phantom multiple interactions on the field transmitted in a flat phantom in *2007 18th International Zurich Symposium on Electromagnetic Compatibility*, pp. 139–142, 2007.

[43] B. Derat and A. Cozza, Analysis of the Transmitted Field Amplitude and SAR Modification Due to Mobile Terminal - Flat Phantom Multiple Interactions in *The Second European Conference on Antennas and Propagation, EuCAP 2007*, pp. 1–6, 2007.

[44] T. Nakae, D. Funahashi, J. Higashiyama, T. Onishi, and A. Hirata, Skin Temperature Elevation for Incident Power Densities From Dipole Arrays at 28 Ghz *IEEE Access*, vol. 8, pp. 26863–26871, 2020.

[45] E. Carrasco, D. Colombi, K. R. Foster, M. Ziskin, and Q. Balzano, Exposure Assessment of Portable Wireless Devices above 6 GHz *Radiation Protection Dosimetry*, vol. 183, pp. 489–496, June 2019.

[46] A. Yaghjian, An overview of near-field antenna measurements *IEEE Transactions on Antennas and Propagation*, vol. 34, no. 1, pp. 30–45, 1986.

[47] P. C. Clemmow, *The Plane Wave Spectrum Representation of Electromagnetic Fields*. Wiley, 1996.

[48] IEEE Recommended Practice for Near-Field Antenna Measurements *IEEE Std 1720-2012*, pp. 1–102, 2012.

[49] K. Sasaki, K. Li, J. Chakarothai, T. Iyama, T. Onishi, and S. Watanabe, Error Analysis of a Near-Field Reconstruction Technique Based on Plane Wave Spectrum Expansion for Power Density Assessment Above 6 GHz *IEEE Access*, vol. 7, pp. 11591–11598, 2019.

[50] C. Scott, *The Spectral Domain Method in Electromagnetics*. Artech House, 1989.

[51] K. Sasaki, K. Li, K. Wake, S. Watanabe, J. Higashiyama, and T. Onishi, Accuracy of Incident Power Density Measured Using Reconstructing Algorithm for Compliance Assessment of Devices in Near-Field at Millimeterwave Frequencies in *International Symposium on Electromagnetic Compatibility, Sapporo and Asia-Pacific (EMC Sapporo/APEMC)*, pp. 43–46, 2019.

[52] J. E. Hansen, *Spherical Near-field Antenna Measurements*. IET, 1988.

[53] O. Breinbjerg, Spherical near-field antenna measurements The most accurate antenna measurement technique in *2016 IEEE International Symposium on Antennas and Propagation (APSURSI)*, pp. 1019–1020, 2016.

[54] Y. Diao and A. Hirata, Exposure Assessment of Array Antennas at 28 GHz Using Hybrid Spherical Near-Field Transformation and FDTD Method *IEEE Transactions on Electromagnetic Compatibility*, pp. 1–9, 2021.

[55] Y. Pinto and J. Wiart, Statistical analysis and surrogate modeling of indoor exposure induced from a WLAN source in *2017 11th European Conference on Antennas and Propagation (EUCAP)*, pp. 806–810, 2017.

[56] Y. Adane, A. Gati, M.-F. Wong, C. Dale, J. Wiart, and V. Hanna, Optimal modeling of real radio base station antennas for human exposure assessment using spherical-mode decomposition *IEEE Antennas and Wireless Propagation Letters*, vol. 1, pp. 215–218, 2002.

[57] A. K. Skrivervik, M. Bosiljevac, and Z. Sipus, Fundamental Limits for Implanted Antennas: Maximum Power Density Reaching Free Space *IEEE Transactions on Antennas and Propagation*, vol. 67, no. 8, pp. 4978–4988, 2019.

[58] K. Nikita, G. Stamatakos, N. Uzunoglu, and A. Karafotias, Analysis of the interaction between a layered spherical human head model and a finite-length dipole *IEEE Transactions on Microwave Theory and Techniques*, vol. 48, no. 11, pp. 2003–2013, 2000.

[59] L. Zhao and K.-L. Wu, A Hybrid Nfm/MoM Full-Wave Analysis of Layered Prolate Head Model Exposed to Handset Antenna *Progress In Electromagnetics Research*, vol. 123, pp. 205–225, 2012.

[60] P. Petre and T. K. Sarkar, Planar near-field to far-field transformation using an equivalent magnetic current approach *IEEE Transactions on Antennas and Propagation*, vol. 40, no. 11, pp. 1348–1356, 1992.

[61] J. L. Araque Quijano and G. Vecchi, Near- and Very Near-Field Accuracy in 3-D Source Reconstruction *IEEE Antennas and Wireless Propagation Letters*, vol. 9, pp. 634–637, 2010.

[62] W. C. Gibson, *The method of moments in electromagnetics*. Chapman and Hall/CRC, 2021.

[63] J.-M. Jin, *The finite element method in electromagnetics*. John Wiley & Sons, 2015.

[64] S. Dey, D. Chatterjee, E. J. Garboczi, and A. M. Hassan, Method of moment analysis of carbon nanotubes embedded in a lossy dielectric slab using a multilayer dyadic greens function *IEEE Transactions on Antennas and Propagation*, 2022.

[65] Y. A. López, F. L.-H. Andrés, M. R. Pino, and T. K. Sarkar, An improved super-resolution source reconstruction method *IEEE Transactions on Instrumentation and Measurement*, vol. 58, no. 11, pp. 3855–3866, 2009.

[66] S. Makarov, MoM antenna simulations, with Matlab: RWG basis functions *IEEE Antennas and Propagation Magazine*, vol. 43, no. 5, pp. 100–107, 2001.

[67] Q. Balzano, M. Y. Kanda, and C. C. Davis, Specific absorption rates in a flat phantom in the near-field of dipole antennas *IEEE Transactions on Electromagnetic Compatibility*, vol. 48, no. 3, pp. 563–568, 2006.

[68] A. R. Guraliuc, M. Zhadobov, R. Sauleau, L. Marnat, and L. Dussopt, Near-Field User Exposure in Forthcoming 5G Scenarios in the 60 GHz Band *IEEE Transactions on Antennas and Propagation*, vol. 65, no. 12, pp. 6606–6615, 2017.

[69] D. Colombi, B. Thors, C. TöRnevik, and Q. Balzano, RF Energy Absorption by Biological Tissues in Close Proximity to Millimeter-Wave 5G Wireless Equipment *IEEE Access*, vol. 6, pp. 4974–4981, 2018.

[70] M. Ziane, R. Sauleau, and M. Zhadobov, Antenna/Body Coupling in the Near-Field at 60 GHz: Impact on the Absorbed Power Density *Applied Sciences*, vol. 10, no. 21, 2020.

[71] L. Alon, S. Gabriel, G. Y. Cho, R. Brown, and C. M. Deniz, Prospects for millimeter-wave compliance measurement technologies [measurements corner] *IEEE Antennas and Propagation Magazine*, vol. 59, no. 2, pp. 115–125, 2017.

[72] EUmmWVx, "5G Power Density Probe." https://speag.swiss/products/dasy8/m-mmwave/new-eummwvx-vector-e-probe-3/, 2017.

[73] A. Turgut and B. K. Engiz, Analyzing the SAR in Human Head Tissues under Different Exposure Scenarios *Applied Sciences*, vol. 13, no. 12, p. 6971, 2023.

[74] Y. Okano and H. Shimoji, Comparison measurement for specific absorption rate with physically different procedure *IEEE Transactions on Instrumentation and Measurement*, vol. 61, no. 2, pp. 439–446, 2011.

[75] Z. Liu, D. Allal, M. Cox, and J. Wiart, Discrepancies of measured SAR between traditional and fast measuring systems *International journal of environmental research and public health*, vol. 17, no. 6, p. 2111, 2020.

[76] Electric field probes - electro-optic Probe (eoProbe), "KAPTEOS." https://en.kapteos.com/eoprobe-datasheet, 2017.

[77] H. Togo, N. Shimizu, and T. Nagatsuma, Near-field mapping system using fiber-based electro-optic probe for specific absorption rate measurement *IEICE transactions on electronics*, vol. 90, no. 2, pp. 436–442, 2007.

[78] Y. Okano, T. Sato, and Y. Sugama, A specific absorption rate measurement method using fiber optic thermal sensors *IEEE Transactions on Instrumentation and Measurement*, vol. 59, no. 6, pp. 1705–1714, 2010.

[79] T. Iyama, K. Kiminami, and T. Onishi, Applicability of three-axis electro-optic (EO) probe for specific absorption rate (SAR) measurement *IEICE transactions on communications*, vol. 92, no. 4, pp. 1414–1417, 2009.

[80] J. Blackwell, G. Oluniran, B. Tuohy, M. Destrade, M. J. Kraśny, and N. Colgan, Experimental assessment of clinical MRI-induced global SAR distributions in head phantoms *Physica Medica*, vol. 66, pp. 113–118, 2019.

[81] M. Tarasek, Y. Shu, D. Kang, S. Tao, E. Gray, J. Huston III, Y. Hua, D. Yeo, M. Bernstein, and T. Foo, Average SAR prediction, validation, and evaluation for a compact MR scanner head-sized RF coil *Magnetic resonance imaging*, vol. 85, pp. 168–176, 2022.

[82] M. Ziane, M. Zhadobov, and R. Sauleau, High-Resolution Technique for Near-Field Power Density Measurement Accounting for Antenna/Body Coupling at Millimeter Waves *IEEE Antennas and Wireless Propagation Letters*, vol. 20, no. 11, pp. 2151–2155, 2021.

[83] J. Lundgren, J. Helander, M. Gustafsson, D. Sjoberg, B. Xu, and D. Colombi, A near-field measurement and calibration technique: Radio-frequency electromagnetic field exposure assessment of millimeter-wave 5G devices *IEEE Antennas and Propagation Magazine*, vol. 63, no. 3, pp. 77–88, 2020.

[84] B. Hakim, B. Beard, and C. Davis, Precise dielectric property measurements and E-field probe calibration for specific absorption rate measurements using a rectangular waveguide *Measurement Science and Technology*, vol. 20, no. 4, p. 045702, 2009.

[85] G. F. Hamberger, C. Rowell, and B. Derat, Near-field techniques for millimeter-wave antenna array calibration in *2019 Antenna Measurement Techniques Association Symposium (AMTA)*, pp. 1–5, IEEE, 2019.

[86] A. Christ, T. Samaras, E. Neufeld, and N. Kuster, Transmission Coefficient of Power Density Into Skin Tissue Between 6 And 300 GHz *Radiation Protection Dosimetry*, vol. 192, pp. 113–118, 12 2020.

[87] Q. Balzano, O. Garay, and K. Siwiak, The near field of dipole antennas, part II: Experimental results *IEEE Transactions on Vehicular Technology*, vol. 30, no. 4, pp. 175–181, 1981.

[88] T. Samaras, A. Christ, and N. Kuster, Compliance Assessment of the Epithelial or Absorbed Power Density Below 10 GHz Using SAR Measurement Systems *Bioelectromagnetics*, vol. 42, no. 6, pp. 484–490, 2021.

[89] S. F. Jafari, R. Sarraf Shirazi, G. Moradi, A. Sibille, and J. Wiart, Absorbed/Epithelial Power Density Assessment Using Plane-Wave Spectrum Method From Inside the Skin Tissue Above 6 GHz *IEEE Transactions on Instrumentation and Measurement*, vol. 71, pp. 1–8, 2022.

[90] F. Karimi, S. Kühn, J. Xi, S. Reboux, A. Christ, A. Fallahi, R. Meyer, and N. Kuster, Method and Implementations to Measure the Absorbed Power Density in *2022 IEEE MTT-S International Microwave Biomedical Conference (IMBioC)*, pp. 129–131, IEEE, 2022.

[91] E. C. Jordan, K. G. Balmain, *et al.*, Electromagnetic waves and radiating systems 1969.

[92] A. Hirata, D. Funahashi, and S. Kodera, Setting exposure guidelines and product safety standards for radio-frequency exposure at frequencies above 6 GHz: brief review *Annals of Telecommunications*, vol. 74, no. 1, pp. 17–24, 2019.

[93] S. Omi, T. Uno, T. Arima, and J. Wiart, Reconstruction of internal field of dielectric objects for noninvasive SAR measurement using boundary integral equation *IEEE Transactions on Electromagnetic Compatibility*, vol. 61, no. 1, pp. 48–56, 2018.

[94] W. He, L. Scialacqua, A. Scannavini, Z. Ying, K. Zhao, B. Xu, C. Di Paola, S. Zhang, and S. He, Incident power density assessment study for 5G millimeter-wave handset based on equivalent currents method in *2020 14th European Conference on Antennas and Propagation (EuCAP)*, pp. 1–4, IEEE, 2020.

[95] S. Pfeifer, A. Fallahi, J. Xi, E. Neufeld, and N. Kuster, Forward Transformation from Reactive Near-Field to Near and Far-Field at Millimeter-Wave Frequencies *Applied Sciences*, vol. 10, no. 14, 2020.

[96] D. Poljak and M. Cvetković, Assessment of absorbed power density (S ab) at the surface of flat lossy medium in GHz frequency range: A case of Hertz dipole in *2020 5th International Conference on Smart and Sustainable Technologies (SpliTech)*, pp. 1–4, IEEE, 2020.

[97] W. He, B. Xu, L. Scialacqua, Z. Ying, A. Scannavini, L. J. Foged, K. Zhao, C. Di Paola, S. Zhang, and S. He, Fast power density assessment of 5G mobile handset using equivalent currents method *IEEE Transactions on Antennas and Propagation*, vol. 69, no. 10, pp. 6857–6869, 2021.

[98] R. H. M. Baharin, S. Omi, T. Uno, and T. Arima, Internal Electric Field Reconstruction and SAR Estimation of In-Body Antenna Using Inverse Equivalent Current Method *IEEE Transactions on Electromagnetic Compatibility*, vol. 63, no. 5, pp. 1658–1666, 2021.

[99] N. Miura, S. Kodera, Y. Diao, J. Higashiyama, Y. Suzuki, and A. Hirata, Power Absorption and Skin Temperature Rise From Simultaneous Near-Field Exposure at 2 and 28 GHz *IEEE Access*, vol. 9, pp. 152140–152149, 2021.

[100] A. Hirata, S. Kodera, K. Sasaki, J. Gomez-Tames, I. Laakso, A. Wood, S. Watanabe, and K. R. Foster, Human exposure to radiofrequency energy above 6 GHz: Review of computational dosimetry studies *Physics in medicine & biology*, vol. 66, no. 8, p. 08TR01, 2021.

[101] Y. Diao and A. Hirata, Assessment of mmWave exposure from antenna based on transformation of spherical wave expansion to plane wave expansion *IEEE Access*, vol. 9, pp. 111608–111615, 2021.

[102] S. Omi, K. Sasaki, and K. Wake, Performance analysis of incident power density evaluation by inverse source method for compliance assessment at quasi-millimeter and millimeter wave bands *IEEE Transactions on Electromagnetic Compatibility*, vol. 63, no. 5, pp. 1649–1657, 2021.

[103] K. Li, Y. Diao, K. Sasaki, A. Prokop, D. Poljak, V. Doric, J. Xi, S. Kodera, A. Hirata, and W. El Hajj, Intercomparison of Calculated Incident Power Density and Temperature Rise for Exposure From Different Antennas at 10–90 GHz *IEEE Access*, vol. 9, pp. 151654–151666, 2021.

[104] Q. Gontier, L. Petrillo, F. Rottenberg, F. Horlin, J. Wiart, C. Oestges, and P. De Doncker, A stochastic geometry approach to EMF exposure modeling *IEEE access*, vol. 9, pp. 91777–91787, 2021.

[105] M. Ziane, M. Zhadobov, and R. Sauleau, Increase of exposure levels due to antenna/body coupling in the 60-GHz band in *2021 XXXIVth General Assembly and Scientific Symposium of the International Union of Radio Science (URSI GASS)*, pp. 1–4, IEEE.

[106] A. Hirata, Y. Diao, T. Onishi, K. Sasaki, S. Ahn, D. Colombi, V. De Santis, I. Laakso, L. Giaccone, W. Joseph, *et al.*, Assessment of human exposure to electromagnetic fields: Review and future directions *IEEE Transactions on Electromagnetic Compatibility*, 2021.

[107] G. Sacco, D. Nikolayev, R. Sauleau, and M. Zhadobov, Antenna/Human Body Coupling in 5G Millimeter-Wave Bands: Do Age and Clothing Matter? *IEEE Journal of Microwaves*, vol. 1, no. 2, pp. 593–600, 2021.

[108] K. S. Cujia, A. Fallahi, S. Reboux, and N. Kuster, Experimental Exposure Evaluation from the Very Close Near-to the Far-Field using a Multiple-Multipole Source Reconstruction Algorithm *IEEE Transactions on Antennas and Propagation*, 2022.

[109] K. Li, S. Kodera, D. Poljak, Y. Diao, K. Sasaki, A. Susnjara, A. Prokop, K. Taguchi, J. Xi, S. Zhang, *et al.*, Calculated Epithelial/Absorbed Power Density for Exposure from Antennas at 10–90 GHz: Intercomparison Study Using a Planar Skin Model *IEEE Access*, 2023.

[110] G. Ancans, V. Bobrovs, A. Ancans, and D. Kalibatiene, Spectrum Considerations for 5G Mobile Communication Systems *Procedia Computer Science*, vol. 104, pp. 509–516, 2017.

[111] P. Joshi, F. Ghasemifard, D. Colombi, and C. Törnevik, Actual Output Power Levels of User Equipment in 5G Commercial Networks and Implications on Realistic RF EMF Exposure Assessment *IEEE Access*, vol. 8, pp. 204068–204075, 2020.

[112] S. Gabriel, R. W. Lau, and C. Gabriel, The dielectric properties of biological tissues: III. Parametric models for the dielectric spectrum of tissues *Physics in Medicine and Biology*, vol. 41, pp. 2271–2293, nov 1996.

[113] Altair Engineering Inc., "FEKO (2020)."

[114] IEC/IEEE International Standard - Measurement procedure for the assessment of specific absorption rate of human exposure to radio frequency fields from hand-held and body-mounted wireless communication devices Part 1528: Human models, instrumentation, and procedures (Frequency range of 4 MHz to 10 GHz) *IEC/IEEE 62209-1528:2020*, pp. 1–284, 2020.

[115] "E-Field Probe EP-EF (NBM)." https://www.narda-sts.it/eng/products/probes/or-03-programmable-optical-repeater-10-hz-40-ghz/.

[116] "WPF Field Probe." https://www.wavecontrol.com/rfsafety/en/products/probes.

[117] L. Petrillo, T. Mavridis, J. Sarrazin, D. Lautru, A. Benlarbi-Delai, and P. De Doncker, Analytical creeping wave model and measurements for 60 GHz body area networks *IEEE transactions on antennas and propagation*, vol. 62, no. 8, pp. 4352–4356, 2014.

[118] Y. Diao, E. A. Rashed, and A. Hirata, Assessment of absorbed power density and temperature rise for nonplanar body model under electromagnetic exposure above 6 GHz *Physics in medicine & biology*, vol. 65, no. 22, p. 224001, 2020.

[119] G. Sacco, Z. Haider, and M. Zhadobov, Exposure levels induced in curved body parts at mmWaves *IEEE Journal of Electromagnetics, RF and Microwaves in Medicine and Biology*, vol. 6, no. 3, pp. 413–419, 2022.

[120] M. M. M. Mustafa, "Isotropic planar layered media." https://drive.google.com/file/d/119WYX1Y1loffDDkUtncHvfFD82p0JNpe/view, 2022.

[121] A. Sommerfeld, Über die Ausbreitung der Wellen inder drahtlosen Telegraphie 1909.

[122] R. E. Collin, Hertzian dipole radiating over a lossy earth or sea: Some early and late 20th-century controversies *IEEE Antennas and Propagation Magazine*, vol. 46, no. 2, pp. 64–79, 2004.

[123] W. C. Chew, *Waves and fields in inhomogeneous media*, vol. 16. Inst of Electrical &, 1995.

[124] L. B. Felsen and N. Marcuvitz, *Radiation and scattering of waves*, vol. 31. John Wiley & Sons, 1994.

[125] J. R. Wait, *Electromagnetic waves in stratified media: Revised edition including supplemented material*, vol. 3. Elsevier, 2013.

[126] M. M. M. Mustafa, *On the Electromagnetic Fields in Planar Layered Media Comprising Anisotropic Conductive Sheets at the Interfaces*. PhD thesis, Texas A&M University, 2019.

[127] D. H. Cheng, On the formulation of the dyadic Green's function in a layered medium *Electromagnetics*, vol. 6, no. 2, pp. 171–182, 1986.

[128] C. A. Balanis, *Advanced engineering electromagnetics*. John Wiley & Sons, 2012.

[129] J. Colinas, Y. Goussard, and J.-J. Laurin, Application of the Tikhonov regularization technique to the equivalent magnetic currents near-field technique *IEEE Transactions on Antennas and Propagation*, vol. 52, no. 11, pp. 3122–3132, 2004.

[130] Mazin Mustafa, "Half-Space Sommerfeld Integrator Electric Fields." https://www.mathworks.com/matlabcentral/fileexchange/69680-half-space-sommerfeld-integrator-electric-fields, 2023.

[131] Mazin Mustafa, "Electric/Magnetic Dipole Radiation in Planar Layered Media." https://www.mathworks.com/matlabcentral/fileexchange/82104-electric-magnetic-dipole-radiation-in-planar-layered-media, 2023.

[132] Dielectric Properties, *The Foundation for Research on Information Technologies in Society (ITIS)*. Zurich, Switzerland.

[133] K. Sasaki, E. Porter, E. A. Rashed, L. Farrugia, and G. Schmid, Measurement and image-based estimation of dielectric properties of biological tissues-past, present, and future- *Physics in Medicine & Biology*, vol. 67, no. 14, p. 14TR01, 2022.

[134] B. Xu, K. Zhao, B. Thors, D. Colombi, O. Lundberg, Z. Ying, and S. He, Power Density Measurements at 15 GHz for RF EMF Compliance Assessments of 5G User Equipment *IEEE Transactions on Antennas and Propagation*, vol. 65, no. 12, pp. 6584–6595, 2017.

[135] C. Di Paola, S. Zhang, K. Zhao, Z. Ying, T. Bolin, and G. F. Pedersen, Wideband Beam-Switchable 28 GHz Quasi-Yagi Array for Mobile Devices *IEEE Transactions on Antennas and Propagation*, vol. 67, no. 11, pp. 6870–6882, 2019.

[136] C. A. Balanis, *Antenna theory: analysis and design*. John wiley & sons, 2015.

[137] E. Carrasco, D. Colombi, K. R. Foster, M. Ziskin, and Q. Balzano, Exposure assessment of portable wireless devices above 6 GHz *Radiation Protection Dosimetry*, vol. 183, no. 4, pp. 489–496, 2019.

[138] H.-T. Chou and Z.-H. Lin, Polarization Agile Beam Steering by Subarray Antenna Module Design to Compensate Wide-Angle Polarization Discrepancy of User Equipment Antenna Radiations at mmW Frequencies *IEEE Transactions on Antennas and Propagation*, vol. 70, no. 9, pp. 8137–8147, 2022.

[139] Dassault Systèmes Simulia Corp., "CST (2021)." https://www.3ds.com/products-services/simulia/products/cst-studio-suite/.

[140] K. Li, S. Kodera, D. Poljak, Y. Diao, K. Sasaki, A. Susnjara, A. Prokop, K. Taguchi, J. Xi, S. Zhang, *et al.*, Calculated Epithelial/Absorbed Power Density for Exposure from Antennas at 10–90 GHz: Intercomparison Study Using a Planar Skin Model *IEEE Access*, 2023.

[141] S. Razafimahatratra, J. Sarrazin, G. Valerio, F. Sarrazin, M. Casaletti, P. De Doncker, and A. Benlarbi-Delai, Input impedance of an aperture over a lossy half-space: application to on-body antenna performance at 60 GHz *Progress In Electromagnetics Research C*, vol. 83, pp. 161–178, 2018.

[142] K. A. Michalski and J. R. Mosig, On the Complete Radiation Pattern of a Vertical Hertzian Dipole Above a Low-Loss Ground *IEEE Journal of Microwaves*, vol. 1, no. 3, pp. 747–762, 2021.

[143] C. Xiao, Z. Liang, and J. Yang, Radiation Characteristic Analysis of Antenna Deeply Implanted in Human Body and Localization Sensor Array *IEEE Transactions on Instrumentation and Measurement*, vol. 71, p. 4009912, 2022.

Publications

Journal

- **Absorbed/Epithelial Power Density Assessment Using Plane-Wave Spectrum Method From Inside the Skin Tissue Above 6 GHz**
  S. F. Jafari, R. Sarraf Shirazi, G. Moradi, A. Sibille and J. Wiart
  IEEE Transaction on Instruments and Measurements, vol. 71, pp. 1-8, 2022

  Abstract: In this paper, the idea of measurement inside the human skin liquid-filled phantom for 5G technologies is examined. Measurement inside the skin tissue phantom is almost off the table due to the shallow penetration depth of fields at millimeter and quasi-millimeter waves. Antenna-body interactions should be considered for absorbed power density (APD) assessment when the device is close to the human body. These effects can be considered to a large extent by measuring within the liquid phantom. The reconstruction technique is used to determine APD at the human skin surface using the backward plane-wave spectrum method through sampling the E-field at the specific distance within the phantom. The reconstruction errors were obtained using a planar array antenna at 10 to 60 GHz frequencies. These errors were no larger than 9.4%, 7.35%, 7.8% at 10, 24, and 60 GHz for assessing the maximum spatially-averaged power density for a separation distance between the device and tissue phantom larger than 1 mm. At last, the measuring requirement for the electric field was also investigated. The results suggest that the coupling/multiple-reflection effects are negligible when the separation distance between antenna and body is larger than λ.

- **Non-Invasive Absorbed Power Density Assessment From 5G Millimeter-Wave Mobile Phones Using Method of Moments**
  S. F. Jafari, R. Sarraf Shirazi, G. Moradi, A. Sibille and J. Wiart
  IEEE Transaction on Antenna and Propagation, vol. 71, pp. 5729-5738, 2023

  Abstract: Absorbed power density (APD) is challenging to assess due to antenna-human body interactions since the antenna is close to the human body. This paper presents a novel technique for non-invasive APD assessment by considering antenna-human body coupling. The electric field integral equation based on spatial dyadic Green's functions (DGFs) is solved inversely by the method of moments to reconstruct the equivalent currents using the electric field sampled on the surface of the hemisphere surrounding the antenna. Then, the APD is assessed by the equivalent

currents beneath the air-phantom interface. The reconstruction errors are obtained using two types of placement of the antenna array, at the edge and corner of the handheld device, at frequencies of 15, 30, and 60 GHz. It was found that at 60 GHz, the errors did not exceed 8.75% and 11.1% for the edge- and corner-type antennas, respectively, for the maximum spatially averaged power density. The measurement requirements were investigated for an actual testing scenario, including angular resolution, E-field measurement uncertainty, and required phantom size. It is shown that the proposed technique paves the way for a new methodology to assess APD, including the antenna-human body coupling, for exposure to handheld devices operating above 6 GHz.

ECOLE DOCTORALE

Titre : Analyse de l'exposition radioélectrique aux ondes millimétriques en champ proche

Mots clés : 5G, densité de puissance absorbée, santé et sécurité, exposition humaine, appareils mobiles, méthode de reconstruction

Résumé : Cette thèse vise à déterminer la densité de puissance absorbée (APD) en tenant compte du couplage et des réflexions multiples entre l'antenne et le corps humain, ce qui pose des défis dans l'évaluation de l'APD en raison de leur proximité étroite.
La première partie de la thèse explore le concept de mesure de l'APD à l'intérieur d'un fantôme de tissu cutané, en se concentrant spécifiquement sur son application dans les technologies 5G. Cependant, la mesure de l'APD à l'intérieur du fantôme de tissu cutané est limitée en raison de la faible profondeur de pénétration des champs aux ondes millimétriques et quasi-millimétriques. Pour surmonter cette limitation, une technique de reconstruction est utilisée, en utilisant la méthode du spectre de plane inverse. Le champ électrique est échantillonné à une distance spécifique à l'intérieur du fantôme, permettant de déterminer la densité de puissance absorbée à la surface de la peau humaine.
Dans la deuxième partie, une approche non invasive basée sur la fonction de Green dyadique (DGF) est proposée pour l'évaluation de l'APD. Cette méthode tient compte du couplage entre le modèle de peau humaine et le dispositif en cours de test (DUT). L'espace entier est divisé en deux demi-espaces : la demi-espace supérieur est rempli d'air, où l'antenne est positionnée, et le demi-espace inférieur est rempli d'un équivalent de peau humaine. L'équation intégrale de champ électrique (EFIE), basée sur les DGF spatiaux, est résolue à l'aide de la méthode des moments (MoM) pour reconstruire les courants équivalents. L'APD est évaluée en fonction des courants équivalents reconstruits sous l'interface air-fantôme.
En plus des techniques proposées, la thèse examine les exigences de mesure pour les deux approches, y compris l'incertitude de mesure du champ électrique, la résolution angulaire d'échantillonnage et la taille requise du fantôme.
Les résultats démontrent que les techniques proposées présentent une nouvelle méthodologie pour évaluer l'APD, en tenant compte du couplage entre le corps humain et l'antenne, notamment dans le contexte de l'exposition aux appareils portables fonctionnant au-dessus de 6 GHz.

Title : Near-field millimeter-wave radio-frequency exposure analysis

Keywords : Absorbed power density (APD), fifth-generation (5G), human exposure, millimeter-wave (mmWave), mobile phone

Abstract : This thesis aims to determine the absorbed power density (APD) considering the coupling and multiple reflections between the antenna and the human body, which poses challenges in assessing APD due to their close proximity.
The first part of the thesis explores the concept of measuring APD inside a skin tissue phantom, specifically focusing on its application in 5G technologies. However, measuring APD inside the skin tissue phantom is limited due to the shallow penetration depth of fields at millimeter and quasi-millimeter waves. To overcome this limitation, a reconstruction technique is employed, utilizing the backward plane-wave spectrum (PWS) method. The electric field is sampled at a specific distance within the phantom, enabling the determination of APD at the human skin surface.
In the second part, a non-invasive approach based on the dyadic Green's function (DGF) is proposed for APD assessment. This method takes into account the coupling between the human skin model and the device under test (DUT). The entire space is divided into two half-spaces : the upper half-space ($z > 0$) is filled with air, where the antenna is positioned, and the lower half-space is filled with an equivalent human skin liquid or solid. The electric field integral equation (EFIE), based on spatial DGFs, is solved using the method of moments (MoM) to reconstruct the equivalent currents. The electric field is sampled on the surface of a hemisphere surrounding the antenna, and the APD is evaluated based on the reconstructed equivalent currents beneath the air-phantom interface.
In addition to the proposed techniques, the thesis investigates the measurement requirements for both approaches, including E-field measurement uncertainty, sampling angular resolution, and the required size of the phantom.
The findings demonstrate that the proposed techniques present a novel methodology for assessing APD, taking into consideration the coupling between the human body and the antenna, particularly in the context of exposure to handheld devices operating above 6 GHz.

Institut Polytechnique de Paris
91120 Palaiseau, France